

Diss. ETH No. 16125

Search for doubly charged Higgs decaying into τ Leptons at HERA

A dissertation submitted to the
Swiss Federal Institute of Technology Zurich
for the degree of
Doctor of Natural Sciences

presented by
Simon Baumgartner

Dipl. Phys. ETH
born on October 30, 1975
citizen of Malters (LU)

accepted on the recommendation of
Prof. Dr. Ralph Eichler, examiner and
Prof. Dr. Urs Langenegger, co-examiner

June 2005

Seite Leer /
Blank leaf

Abstract

A search for doubly charged Higgs bosons H^{++} , decaying into $\tau\tau$ and $e\tau$ lepton pairs is presented. The Yukawa couplings tested hereby are $h_{\tau\tau}$ and $h_{e\tau}$. The search is performed with data taken at the H1 experiment at HERA, corresponding to an integrated luminosity of $\mathcal{L} = 88.1 \text{ pb}^{-1}$.

The analysis is based on tracks with high transverse momentum in the central detector region. The dominant background of high Q^2 neutral current events is reduced by simple cuts on the event kinematics and on the isolation of the tracks. Di-lepton production background is reduced by requiring tracks with like-sign charge. Despite the missing energy due to neutrinos from τ decays, the invariant mass of the $\tau\tau$ and $e\tau$ system can be fully reconstructed by applying momentum balance constraints on the event.

No evidence for a doubly charged Higgs signal in the above decay channels is observed. Therefore, upper limits on the production cross section are calculated. In the mass range $80 \leq M_{H^{++}} \leq 150 \text{ GeV}$ these limits are found to be $\sigma(ep \rightarrow H^{++}) \times BR(H^{++} \rightarrow \tau\tau) \leq 0.2 \text{ pb}$ and $\sigma(ep \rightarrow H^{++}) \times BR(H^{++} \rightarrow e\tau) \leq 0.2 \text{ pb}$ at 95% confidence level. Upper limits on the diagonal couplings h_{ll} under the assumption of a democratic scenario $h_{ee} = h_{\mu\mu} = h_{\tau\tau}$, and on the coupling $h_{e\tau}$ under the assumption $BR(H^{++} \rightarrow e\tau) = 100\%$ are derived.

Zusammenfassung

Diese Arbeit beschreibt die Suche nach dem doppelt geladenen Higgs Boson H^{++} und seinen möglichen Zerfällen nach $\tau\tau$ und $e\tau$ Lepton Paaren. Die hierfür verantwortlichen Yukawa-Kopplungen sind $h_{\tau\tau}$ und $h_{e\tau}$. Die Suche basiert auf Daten, die am H1 Experiment bei HERA genommen wurden und die einer integrierten Luminosität von $\mathcal{L} = 88.1 \text{ pb}^{-1}$ entsprechen.

Die Grundlage der Analyse bilden Spuren von hohem Transversalimpuls im zentralen Bereich des Detektors. Der Hauptuntergrund, Ereignisse des neutralen Stroms bei hohem Q^2 , wird durch Schnitte auf die Ereigniskinematik und auf die Isolation der Spuren unterdrückt. Untergrund aus Bi-Lepton Produktion wird durch eine Bedingung auf gleiche Ladung der Spuren reduziert. Trotz der aus den τ Zerfällen resultierenden, nicht messbaren Neutrinoenergien kann die volle invariante Masse der $\tau\tau$ und $e\tau$ Endzustände rekonstruiert werden, indem für alle Ereignisse Impulserhaltung gefordert wird.

Es konnte kein Hinweis auf die Existenz des doppelt geladenen Higgs Bosons in den obigen Zerfallskanälen gefunden werden. Deshalb wurden obere Ausschlussgrenzen auf den Produktionswirkungsquerschnitt ausgerechnet. Im Massenbereich $80 \leq M_{H^{++}} \leq 150 \text{ GeV}$ sind diese Grenzen $\sigma(ep \rightarrow H^{++}) \times BR(H^{++} \rightarrow \tau\tau) \leq 0.2 \text{ pb}$ und $\sigma(ep \rightarrow H^{++}) \times BR(H^{++} \rightarrow e\tau) \leq 0.2 \text{ pb}$ für ein 95% Vertrauensniveau. Ferner wurde eine Obergrenze auf die diagonalen Kopplungen h_{ll} , unter Annahme des demokratischen Szenarios $h_{ee} = h_{\mu\mu} = h_{\tau\tau}$, und eine Obergrenze auf die Kopplung $h_{e\tau}$, unter der Annahme $BR(H^{++} \rightarrow e\tau) = 100\%$, berechnet.

Seite Leer /
Blank leaf

Contents

| | |
|--|-----------|
| Introduction | 1 |
| 1 Theory | 3 |
| 1.1 Outline of the Standard Model | 3 |
| 1.1.1 Particle Spectrum | 3 |
| 1.1.2 $SU(2)_L$ and $U(1)_Y$ Gauge Transformations | 4 |
| 1.1.3 Particle Masses | 6 |
| 1.2 The Higgs Mechanism in the SM | 7 |
| 1.3 An extended Higgs Sector in general | 9 |
| 1.3.1 The ρ parameter | 9 |
| 1.3.2 Flavour Changing Neutral Currents (FCNC) | 10 |
| 1.4 A Model with one Higgs Triplet | 10 |
| 1.5 Left-Right Symmetric Models | 11 |
| 1.6 Doubly charged Higgs at HERA | 13 |
| 1.6.1 Production and Decay of the doubly charged Higgs | 13 |
| 1.6.2 Doubly charged Higgs at other colliders | 15 |
| 1.6.2.1 LEP | 15 |
| 1.6.2.2 Tevatron and LHC | 15 |
| 1.7 The HTM MC Generator | 17 |
| 2 The H1 Experiment at HERA | 21 |
| 2.1 The HERA accelerator | 21 |
| 2.2 The H1 experiment | 22 |
| 2.2.1 Central Jet Chamber | 24 |
| 2.2.2 Calorimeter | 25 |
| 2.2.2.1 Spaghetti Calorimeter (SPACAL) | 26 |
| 2.2.3 Instrumented Iron | 26 |
| 2.2.4 Trigger and Data Acquisition | 26 |
| 2.2.4.1 L1 Trigger Elements of this analysis | 27 |
| 2.2.5 Luminosity System | 28 |
| 2.3 Simulation of the H1 Experiment | 29 |

| | | |
|----------|---|-----------|
| 3 | Preselection | 31 |
| 3.1 | Data Sets | 31 |
| 3.2 | Selection of the candidates | 32 |
| 3.3 | Back to back Topology | 37 |
| 3.4 | Non ep Background Suppression | 38 |
| 3.5 | Event Classification | 40 |
| 3.5.1 | Electron Identification | 41 |
| 3.5.2 | Muon Identification | 41 |
| 3.6 | Trigger | 42 |
| 3.6.1 | Trigger Efficiencies | 42 |
| 3.7 | Data - MC comparison | 46 |
| 3.7.1 | The Background MC | 46 |
| 3.7.2 | Data - MC discrepancies | 48 |
| 3.7.2.1 | $e\mu$ Event Class | 48 |
| 3.7.2.2 | Forward Region | 49 |
| 3.7.3 | τ -Jet refinement | 52 |
| 3.7.4 | Control Distributions | 52 |
| 4 | Final Selection | 55 |
| 4.1 | Rejection of NC Events | 55 |
| 4.1.1 | $\tau\tau$ Topology | 55 |
| 4.1.2 | $e\tau$ Topology | 57 |
| 4.1.3 | Electron scattering angle | 60 |
| 4.2 | Isolation Criteria | 62 |
| 4.2.1 | Lepton Isolation | 63 |
| 4.2.2 | Hadron Isolation | 63 |
| 4.3 | Inelastic Background | 66 |
| 4.4 | Invariant Mass Reconstruction | 67 |
| 4.4.1 | $\tau\tau$ Topology | 67 |
| 4.4.2 | $e\tau$ Topology | 69 |
| 4.4.3 | Mass Requirement | 72 |
| 4.5 | Charge Requirement | 73 |
| 4.6 | Final Cutflows | 77 |
| 5 | Results | 81 |
| 5.1 | Systematic Errors | 81 |
| 5.1.1 | Signal | 81 |
| 5.1.2 | Background | 84 |
| 5.2 | Efficiencies | 85 |
| 5.3 | Limit Calculation | 90 |
| 5.3.1 | Multiple Search Channels | 91 |
| 5.3.2 | Treatment of Systematic Uncertainties | 93 |
| 5.3.3 | Limits for individual Event Classes | 94 |
| 5.3.4 | Combined Limits | 94 |

| | |
|-------------------------|------------|
| 6 Conclusion | 101 |
| List of Figures | 103 |
| List of Tables | 107 |
| Bibliography | 109 |
| A Data Events | 115 |
| Danksagung | 127 |
| Curriculum Vitae | 129 |

Introduction

Because of its importance, the Higgs Boson is maybe the most sought-after particle in particle physics today. Although predicted by the so called *Standard Model (SM)* of particle physics, no evidence for its existence has so far been found. Many searches have already been performed at different experiments. The most prominent search at LEP [1] e.g. sets a lower limit on the Higgs mass of $M = 114.4 \text{ GeV}/c^2$ in the simplest theoretical case of just one Higgs doublet.

At the electron-proton collider HERA the Higgs search sensitivities and therefore also the Higgs discovery potentials are lower than at LEP for most of the theoretical Higgs scenarios. For instance for the one Higgs doublet case cited above the production cross section at HERA is smaller by several orders of magnitude while there is at the same time more background from QCD processes. However, there are scenarios where HERA is competitive. One such possibility are models which give rise to doubly charged Higgs bosons. If existing, these particles would decay dominantly into di-lepton final states, as charge conservation forbids decays into two quarks.

The original motivation to look for doubly charged Higgs bosons at the H1 experiment was the observation of an excess of high mass final states with 2 and 3 electrons [2]. The original H1 searches [3] for doubly charged Higgs bosons have therefore focused on the Higgs decay into electrons and muons. Although the high mass multi-electron events were found not to be compatible with the doubly charged Higgs hypothesis, the analysis was extended to the lepton flavour violating decay channel $H^{\pm\pm} \rightarrow e\mu$. This thesis represents the further extension towards decay channels containing τ -leptons. Notably the decay into a pair of τ leptons and the lepton flavour violating decay into an electron- τ pair are studied. Only the data from the 1996/1997 and 1999/2000 (HERA I run) are used.

Seite Leer /
Blank leaf

Chapter 1

Theory

1.1 Outline of the Standard Model

The *Standard Model (SM)* [4, 5] is today the best theory for describing elementary particles and their interactions. It arose from the Glashow-Salam-Weinberg model (GSW) [6, 7, 8] of the electroweak interaction. The basic concept of the SM is the invariance under a set of local gauge transformations. The gauge bosons responsible for the interactions between fermions emerge then from this requirement.

1.1.1 Particle Spectrum

In the SM two categories of particles are present: Fermions with spin 1/2 and gauge bosons with spin 1. Within the fermions different types exist: leptons and quarks (see Table 1.1). The quarks participate in strong and electroweak interactions, while leptons only participate in the electroweak interaction. The quantum numbers shown are the charge Q the hypercharge Y and the third component of the weak isospin T_3 . These quantities are connected through the relation¹:

$$Q = \frac{Y}{2} + T_3. \quad (1.1)$$

Table 1.1 distinguishes between the left-handed² fermions, which take part in the charged weak interaction and which form doublets of weak isospin \vec{T} and the right-handed isospin singlets. There are no right-handed neutrinos in the SM.

For the down-type quarks, the eigenstates of weak interaction d' , s' and b' are not identical to their respective mass eigenstates d , s , and b . These different eigenstates are related through the *Cabibbo-Kobayashi-Maskawa (CKM)* mixing matrix V_{CKM} [10]:

¹There are also other conventions in use for the definition of the hypercharge. Another frequent convention e.g. defines the hypercharge as half of the quantity used here.

²For a massless left-handed fermion the spin and the momentum are antiparallel to each other. If they are parallel, the fermion is right-handed.

| | Generation | | | T_3 | Y | Q |
|---------|--|--|--|-------|------|------|
| | 1st | 2nd | 3rd | | | |
| Leptons | $\begin{pmatrix} \nu_e \\ e \end{pmatrix}_L$ | $\begin{pmatrix} \nu_\mu \\ \mu \end{pmatrix}_L$ | $\begin{pmatrix} \nu_\tau \\ \tau \end{pmatrix}_L$ | 1/2 | -1 | 0 |
| | e_R | μ_R | τ_R | -1/2 | -1 | -1 |
| | | | | 0 | -2 | -1 |
| Quarks | $\begin{pmatrix} u \\ d' \end{pmatrix}_L$ | $\begin{pmatrix} c \\ s' \end{pmatrix}_L$ | $\begin{pmatrix} t \\ b' \end{pmatrix}_L$ | 1/2 | 1/3 | 2/3 |
| | u_R | c_R | t_R | -1/2 | 1/3 | -1/3 |
| | d'_R | s'_R | b'_R | 0 | 4/3 | 2/3 |
| | | | | 0 | -2/3 | -1/3 |

Table 1.1: *Properties of the fermions in the Standard Model [9].*

$$\begin{pmatrix} d' \\ s' \\ b' \end{pmatrix} = V_{CKM} \begin{pmatrix} d \\ s \\ b \end{pmatrix} = \begin{pmatrix} V_{ud} & V_{us} & V_{ub} \\ V_{cd} & V_{cs} & V_{cb} \\ V_{td} & V_{ts} & V_{tb} \end{pmatrix} \begin{pmatrix} d \\ s \\ b \end{pmatrix}. \quad (1.2)$$

The gauge bosons (see Table 1.2) mediate the interactions between the fermions. Each of the 4 fundamental interactions has its own set of gauge bosons³.

| Interaction | Gauge boson(s) | Relative strength | Range [m] | Participating fermions |
|-----------------|---------------------|-------------------|-----------------|------------------------|
| strong | 8 gluons (g) | 1 | $\leq 10^{-15}$ | quarks |
| electromagnetic | photon (γ) | 10^{-2} | ∞ | all charged |
| weak | W^\pm, Z^0 | 10^{-6} | 10^{-18} | all |
| gravitational | [graviton (G)] | 10^{-39} | ∞ | all |

Table 1.2: *Interactions in the standard model and the corresponding gauge bosons. The relative strengths of the forces are roughly given for short distance scales of a few fm.*

1.1.2 $SU(2)_L$ and $U(1)_Y$ Gauge Transformations

Leaving out the quarks and the strong interactions, the Lagrangian density⁴ describing massless non-interacting leptons and neutrinos can be written as:

$$\mathcal{L}_F = i(\bar{\Psi}_L^l \not{\partial} \Psi_L^l + \bar{\psi}_R^l \not{\partial} \psi_R^l), \quad (1.3)$$

where the usual notation is used: $\not{\partial} = \gamma^\mu \partial_\mu$ and $\bar{\psi} = \psi^\dagger \gamma^0$. ψ_R^l is the right-handed charged lepton singlet of weak isospin $SU(2)_L$ and

$$\Psi_L^l = \begin{pmatrix} \psi_L^\nu \\ \psi_L^l \end{pmatrix} \quad (1.4)$$

³Gravitation is actually not part of the SM and also the graviton is so far just a hypothetical particle.

⁴In the rest of the text, for simplicity reasons, the Lagrangian density will be called Lagrangian.

is the left-handed $SU(2)_L$ doublet. As it is done in QED it is required that the Lagrangian of equation (1.3) should be invariant under local gauge transformations, namely transformations of the following kind:

$$\begin{aligned} SU(2)_L : \quad \Psi_L^l(x) &\rightarrow \Psi_L^{\prime l}(x) = e^{i\frac{g}{2}\vec{\tau}\vec{\omega}(x)}\Psi_L^l(x) \\ U(1)_Y : \quad \psi_R^l(x) &\rightarrow \psi_R^{\prime l}(x) = e^{i\frac{g'}{2}Y_R\chi(x)}\psi_R^l(x). \end{aligned} \quad (1.5)$$

Here $\omega_i(x)$ ($i = 1, 2, 3$) and $\chi(x)$ are arbitrary functions depending on the space-time point x . The meaning of the constants g and g' is explained below. The τ_i ($i = 1, 2, 3$) are the Pauli matrices, which are linearly independent generators of the $SU(2)$ group:

$$\tau_1 = \begin{pmatrix} 0 & 1 \\ 1 & 0 \end{pmatrix} \quad \tau_2 = \begin{pmatrix} 0 & -i \\ i & 0 \end{pmatrix} \quad \tau_3 = \begin{pmatrix} 1 & 0 \\ 0 & -1 \end{pmatrix}. \quad (1.6)$$

It can be easily seen that the Lagrangian of equation (1.3) is not invariant under the transformation (1.5) since the derivative acts on the functions $\omega(x)$, $\chi(x)$ leaving terms of the form:

$$\tau_i \bar{\Psi}_L^l \gamma^\mu \Psi_L^l \partial_\mu \omega_i(x) \quad \text{and} \quad Y \bar{\psi}_R^l \gamma^\mu \psi_R^l \partial_\mu \chi(x). \quad (1.7)$$

Again as in QED local gauge invariance can be achieved though by adding to the derivative ∂^μ additional gauge fields, which transform exactly in a way to cancel the terms (1.7):

$$\partial^\mu \rightarrow D_L^\mu = \partial^\mu + i\frac{g}{2}\vec{\tau} \cdot \vec{W}^\mu + i\frac{g'}{2}YB^\mu \quad \text{for left-handed leptons,} \quad (1.8)$$

$$\partial^\mu \rightarrow D_R^\mu = \partial^\mu + i\frac{g'}{2}YB^\mu \quad \text{for right-handed leptons.} \quad (1.9)$$

The new gauge fields $W_{1,2,3}^\mu$ and B^μ couple with coupling constants g and g' to the fermions. In order to cancel the terms (1.7) they have to transform under $SU(2)_L$, $U(1)_Y$ respectively as:

$$W_i^\mu \xrightarrow{SU(2)_L} W_i^\mu - \partial^\mu \omega_i - g\vec{\omega} \times \vec{W}^\mu \quad (1.10)$$

$$B^\mu \xrightarrow{U(1)_Y} B^\mu - \partial^\mu \chi. \quad (1.11)$$

The physically observed gauge bosons are linear combinations of the above fields. The charged gauge bosons W^\pm , which couple neutrinos to charged leptons are:

$$W^{(\pm)\mu} = \frac{1}{\sqrt{2}}(W_1^\mu \pm iW_2^\mu). \quad (1.12)$$

The product $\vec{\tau} \cdot \vec{W}^\mu$ in (1.8), which produces the coupling of leptons and bosons, can now be more conveniently written in terms of the W^\pm when using the isospin operators τ^+ and τ^- :

$$\tau^+ = \frac{1}{2}(\tau_1 + i\tau_2) = \begin{pmatrix} 0 & 1 \\ 0 & 0 \end{pmatrix} \quad \tau^- = \frac{1}{2}(\tau_1 - i\tau_2) = \begin{pmatrix} 0 & 0 \\ 1 & 0 \end{pmatrix}. \quad (1.13)$$

By defining the vectors:

$$\vec{\tau} = (\sqrt{2}\tau^+, \tau_3, \sqrt{2}\tau^-) \quad (1.14)$$

$$\vec{W}^\mu = (W^{(-)\mu}, W_3^\mu, W^{(+)\mu}), \quad (1.15)$$

it follows:

$$\vec{\tau} \cdot \vec{W}^\mu = \sqrt{2}(\tau^+ W^{(-)\mu} + \tau^- W^{(+)\mu}) + \tau_3 W_3^\mu = \sum_{i=1}^3 \tau_i W_i^\mu. \quad (1.16)$$

The Z^μ and A^μ fields for the Z-boson and photon are:

$$Z^\mu = -B^\mu \sin \theta_W + W_3^\mu \cos \theta_W \quad (1.17)$$

$$A^\mu = B^\mu \cos \theta_W + W_3^\mu \sin \theta_W, \quad (1.18)$$

where θ_W is the Weinberg mixing angle. Inserting these fields back into (1.8) and requiring that the coupling of the photon field A^μ must be the electric charge e as in QED yields a relation between the couplings g , g' and the charge e :

$$g' \cos \theta_W = g \sin \theta_W = e. \quad (1.19)$$

According to the Noether theorem every continuous symmetry in the Lagrangian gives rise to a conserved quantity. From the local $SU(2)_L \times U(1)_Y$ gauge symmetry under the transformations (1.5), the conserved quantities turn out to be the weak isospin \vec{T} (generator of $SU(2)_L$ transformations) and the hypercharge Y (generator of $U(1)_Y$ transformations). Consequently the electric charge, which is related to Y and T_3 via (1.1) is also conserved.

The inclusion of the strong interaction into the SM follows the same pattern as the electroweak part. There again a local gauge invariance of the quark colour fields is required under $SU(3)_C$ gauge transformations. The 8 different gauge bosons (the gluons) come out in the same way. Finally, the SM is a gauge theory based on the $SU(3)_C \times SU(2)_L \times U(1)_Y$ gauge group.

1.1.3 Particle Masses

So far all particles in the theory have to be massless. A massive particle would produce a term in the Lagrangian proportional to the square of the corresponding field. For instance:

$$m_W^2 W_\mu^{(+)} W^{(-)\mu} \quad W \text{ mass term} \quad (1.20)$$

$$-m_e \bar{\psi}_e \psi_e \quad \text{Electron mass term} \quad (1.21)$$

Both types of mass terms for gauge bosons and fermions would destroy the local $SU(2)_L \times U(1)_Y$ gauge symmetry. For the W mass term this can be seen by using the

transformation (1.10). For the fermions the Dirac mass term can be decomposed into left-handed and right-handed states:

$$-m_e \bar{\psi}_e \psi_e = -m_e (\bar{\psi}_e^L \psi_e^R + \bar{\psi}_e^R \psi_e^L). \quad (1.22)$$

The mixed products of left-handed and right-handed states in (1.22) can not be gauge invariant since the left-handed states ψ^L transform only under $SU(2)_L$ gauge transformations and the right-handed states ψ^R transform under $U(1)_Y$. Producing massive fermions and gauge bosons while still preserving local gauge symmetry is exactly what the Higgs mechanism does.

1.2 The Higgs Mechanism in the SM

The Higgs mechanism in its simplest form in the SM requires the addition of a doublet of complex Higgs fields Φ with weak isospin $T = 1/2$ and hypercharge $Y = 1$.

$$\Phi = \begin{pmatrix} \phi^+ \\ \phi^0 \end{pmatrix} = \frac{1}{\sqrt{2}} \begin{pmatrix} \phi_1^+ + i\phi_2^+ \\ \phi_1^0 + i\phi_2^0 \end{pmatrix} \quad (1.23)$$

The Lagrangian of the scalar Higgs field is of the form:

$$\mathcal{L} = (\partial_\mu \Phi)^\dagger (\partial^\mu \Phi) - V \quad (1.24)$$

with a potential V of the form:

$$V(\Phi) = \mu^2 \Phi^\dagger \Phi + \lambda (\Phi^\dagger \Phi)^2. \quad (1.25)$$

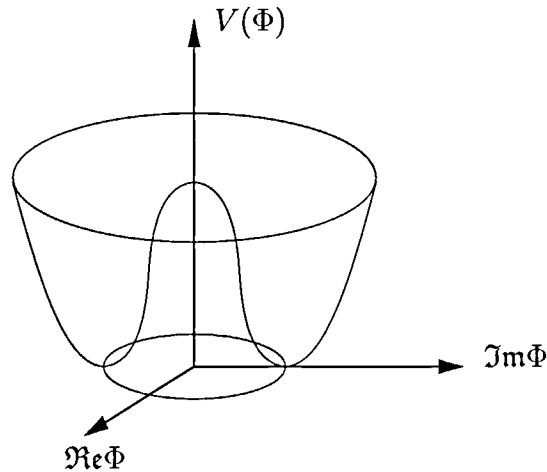


Figure 1.1: *Higgs Potential for a single complex scalar field*

The potential must be bounded below in order to be physically meaningful, which translates to $\lambda > 0$. For $\mu^2 < 0$ the potential takes the form of a Mexican hat (see Figure

1.1). This means that the minimum potential is not at $\Phi = 0$ but on a circle with radius $|\Phi| = \sqrt{-\mu^2/2\lambda}$ from the centre. These vacuum states can be written as:

$$\Phi(x) = \frac{1}{\sqrt{2}} e^{\frac{1}{2}i\vec{\tau}\vec{\theta}} \begin{pmatrix} 0 \\ v \end{pmatrix} \quad \text{with} \quad v = \sqrt{\frac{-\mu^2}{\lambda}}. \quad (1.26)$$

v is called the *Vacuum Expectation Value (VEV)*. The general form (1.23) of the Higgs doublet can now be written as an expansion around the vacuum state (1.26) with an $SU(2)_L$ local gauge transformation:

$$\Phi = \frac{1}{\sqrt{2}} e^{\frac{1}{2}i\vec{\tau}\vec{\eta}(x)} \begin{pmatrix} 0 \\ v + h(x) \end{pmatrix} \approx \frac{1}{\sqrt{2}} \begin{pmatrix} \eta_1 + i\eta_2 \\ v + h + i\eta_3 \end{pmatrix}. \quad (1.27)$$

The right-hand side of this equation is obtained for small values of $\vec{\eta}(x)$ and is equivalent to (1.23). Since the aim is to construct a Lagrangian, which should be gauge invariant, we are allowed to choose a special gauge such that $\vec{\eta} = 0$. This is equivalent to choosing a specific vacuum state and expanding the Higgs field around this vacuum state.

$$\Phi = \frac{1}{\sqrt{2}} \begin{pmatrix} 0 \\ v + h(x) \end{pmatrix} \quad \text{with the vacuum} \quad \langle \Phi_0 \rangle = \frac{1}{\sqrt{2}} \begin{pmatrix} 0 \\ v \end{pmatrix}. \quad (1.28)$$

This is also referred to as *spontaneous symmetry breaking*, because by expanding around a specific vacuum state the initial symmetry in the Higgs potential is lost. The Lagrangian (1.24) is made $SU(2)_L$ gauge invariant by replacing the derivatives by (1.8):

$$\mathcal{L} = (D_\mu \Phi)^\dagger (D^\mu \Phi) - \mu^2 \Phi^\dagger \Phi - \lambda (\Phi^\dagger \Phi)^2. \quad (1.29)$$

Inserting the Higgs field of (1.28) and the physical boson fields of (1.12), (1.17) and (1.18) into this Lagrangian yields among others all mass terms:

$$\begin{aligned} \mathcal{L}_{W-mass} &= \frac{1}{4} v^2 g^2 W_\mu^{(+)} W^{(-)\mu} && \rightarrow m_W = \frac{1}{2} v g \\ \mathcal{L}_{Z-mass} &= \frac{1}{8} v^2 (g^2 + g'^2) Z_\mu Z^\mu && \rightarrow m_Z = m_W / \cos \theta_W \\ \mathcal{L}_{H-mass} &= \frac{1}{2} (2v^2 \lambda) h^2 && \rightarrow m_h = \sqrt{2v^2 \lambda}, \end{aligned} \quad (1.30)$$

and interactions terms:

$$\mathcal{L}_{int} = \frac{1}{2} v g^2 W_\mu^{(+)} W^{(-)\mu} h + \frac{1}{4} g^2 W_\mu^{(+)} W^{(-)\mu} h^2 + \frac{v g^2}{4 \cos^2 \theta_W} Z_\mu Z^\mu h + \frac{g^2}{8 \cos^2 \theta_W} Z_\mu Z^\mu h^2. \quad (1.31)$$

Fermion masses can be obtained by Yukawa couplings to the Higgs field with coupling constants g_l :

$$\mathcal{L}_{FH} = -g_l (\bar{\Psi}_L^l \psi_R^l \Phi + \Phi^\dagger \bar{\psi}_R^l \Psi_L^l). \quad (1.32)$$

Inserting (1.28) yields again mass and interaction terms:

$$\mathcal{L}_{mass} = -\frac{1}{\sqrt{2}} v g_l \bar{\psi}_l \psi_l \quad \rightarrow m_l = v g_l / \sqrt{2} \quad (1.33)$$

$$\mathcal{L}_{int} = -\frac{g_l}{\sqrt{2}} \bar{\psi}_l \psi_l h. \quad (1.34)$$

1.3 An extended Higgs Sector in general

Although the SM Higgs mechanism has the advantage of being simple, it also leaves certain questions open. For instance it is not clear, where the huge differences between fermion masses comes from. Even more disturbing are the recent discoveries of neutrino oscillations in solar, atmospheric and reactor neutrinos [11]. In the SM the neutrinos are strictly massless, but for such oscillations to occur, the neutrinos are required to have masses. There are several possible scenarios how neutrinos could acquire a mass. A Dirac mass term like in (1.21) would require the existence of a right-handed neutrino state ψ_R^ν , which is absent in the SM but could be incorporated. In this case the neutrinos acquire their mass in the same way as the charged leptons and quarks, namely by interaction with a Higgs doublet field of weak isospin 1/2 (see equation (1.34)). Another possibility is that neutrinos are their own antiparticles. Such particles are also called *Majorana* particles. One immediate consequence of Majorana neutrinos would be the non-conservation of lepton number. Transitions between left-handed and right-handed neutrinos would be possible e.g. by interaction with the Higgs fields. Such transitions would not only violate lepton number conservation by $\Delta L = \pm 2$ but also require a change in weak isospin of $\Delta T_3 = \pm 1$, which can only be mediated by Higgs triplet fields. Therefore, in order to have massive Majorana neutrinos an extension in the Higgs sector becomes unavoidable.

Before having a closer look into two extensions of the Higgs sector containing Higgs triplets, it should be noted that there is not complete freedom in the design of a Higgs sector. Experiments impose a few constraints, which any possible Higgs scenario must fulfil.

1.3.1 The ρ parameter

One major constraint for any Higgs scenario comes from the so-called ρ parameter, which is defined at tree level as:

$$\rho \equiv \frac{m_W^2}{(m_Z^2 \cos^2 \theta_W)}. \quad (1.35)$$

This parameter relates the masses of the W and Z bosons and the Weinberg mixing angle θ_W . It is known from experiment to be close to 1, i.e. $\rho \approx 1$. The ρ parameter is also closely related to the Higgs sector of the theory [12]:

$$\rho = \frac{\sum_{T,Y} [4T(T+1) - Y^2] |V_{T,Y}|^2 c_{T,Y}}{\sum_{T,Y} 2Y^2 |V_{T,Y}|^2}. \quad (1.36)$$

In equation (1.36) $V_{T,Y}$ denotes the vacuum expectation value of each neutral Higgs field and T, Y denote the total $SU(2)_L$ isospin and hypercharge of the multiplet to which it belongs. The factor $c_{T,Y}$ distinguishes between real and complex fields for the multiplet with (T, Y) :

$$c_{T,Y} = \begin{cases} 1, & (T, Y) \leftrightarrow \text{complex multiplet} \\ 1/2, & (T, Y = 0) \leftrightarrow \text{real multiplet} \end{cases} \quad (1.37)$$

From (1.36) it follows that multiplets, which fulfil the condition

$$4T(T+1) - Y^2 = 2Y^2 \quad \text{or} \quad (2T+1)^2 - 3Y^2 = 1, \quad (1.38)$$

will always satisfy $\rho = 1$. Singlets ($T = 0, Y = 0$) and doublets with ($T = 1/2, Y = \pm 1$) do satisfy this condition. More complicated solutions exist as e.g. a septet with ($T = 3, Y = 4$), but because of their complicated structure they are usually discarded [12].

Instead, there are other means to enforce $\rho \approx 1$ than equation (1.38). For instance a theory containing $SU(2)_L$ triplets together with the usual doublets (satisfying (1.38)) can be constructed such that

- The vacuum expectation values of the neutral fields of the triplets are small compared to the neutral doublet fields. This means that the triplet contributions to (1.36) are small.
- There are several Higgs triplets with $Y, V_{T,Y}$ values arranged such that their overall contribution to (1.36) is zero.
- The triplets do not contain neutral members, e.g. a $Y = -4$ triplet.

Thus $\rho = 1$ can be satisfied also in more complicated Higgs scenarios.

1.3.2 Flavour Changing Neutral Currents (FCNC)

Another requirement for any Higgs model is the experimentally observed absence of flavour changing neutral currents (FCNC). In the minimal Higgs scenario FCNC are absent. This is because the Higgs-fermion Yukawa couplings are diagonal in terms of fermion flavour. For more complicated Higgs scenarios it becomes more difficult to show that FCNC are absent. If the fermions couple to more than one neutral Higgs it is no longer clear that the fermion mass matrix and the Higgs couplings are diagonal, which would be required for the absence of FCNC.

The simplest way around is to assume that the neutral Higgs bosons mediating FCNC have masses above the energies, which are currently accessible at colliders. Another possibility is to assume that the fermions couple to Higgs bosons from one multiplet only [13].

1.4 A Model with one Higgs Triplet

In this section a triplet of complex Higgs fields is added to the SM doublet of (1.23). The triplet is required to have hypercharge $Y = 2$ and thus the Higgs sector takes the form:

$$\vec{\Delta} = \begin{pmatrix} \Delta^{++} \\ \Delta^+ \\ \Delta^0 \end{pmatrix} \quad \vec{\Phi} = \begin{pmatrix} \phi^+ \\ \phi^0 \end{pmatrix}. \quad (1.39)$$

This model was first proposed by Gelmini and Roncadelli [14] with the intention to produce Majorana masses for neutrinos. If we denote the vacuum expectation values of the neutral members by $\langle\phi^0\rangle = v$ and $\langle\Delta^0\rangle = w$, then the ρ parameter of equation (1.36) becomes:

$$\rho = \frac{1 + \frac{2w^2}{v^2}}{1 + \frac{4w^2}{v^2}}. \quad (1.40)$$

This means that ρ is less than unity and from current experimental constraints the ratio w/v can be constrained to [15]:

$$\frac{w}{v} \leq 0.066 \quad \text{at 99\% CL.} \quad (1.41)$$

In order to conveniently write down the Yukawa interactions of leptons and the Higgs triplet, an $SU(2)_L$ representation of the Higgs triplet should be constructed with the product $\vec{\tau} \cdot \vec{\Delta}$ where $\vec{\tau}$ is the vector of Pauli matrices of equation (1.14):

$$\Delta \equiv \vec{\tau} \cdot \vec{\Delta} = \begin{pmatrix} \Delta^+ & \sqrt{2}\Delta^{++} \\ \sqrt{2}\Delta^0 & -\Delta^+ \end{pmatrix}. \quad (1.42)$$

The Lagrangian for Yukawa interactions of the left-handed lepton doublets and the Higgs triplet can now be written [16]:

$$\mathcal{L}_{int} = ih_{ij}(\Psi_{iL}^T C \tau_2 \Delta \Psi_{jL}) + h.c. \quad (1.43)$$

τ_2 is the second Pauli matrix and C is the charge conjugation matrix and *h.c.* means hermitian conjugate. The Lagrangian from equation (1.43) mediates transitions between fermions and antifermions and especially it produces a Majorana mass term for neutrinos:

$$\mathcal{L}_{mass} = m_{\nu_i} \overline{(\psi_L^{\nu_i})^c} \psi_L^{\nu_i} \quad \text{with} \quad m_{\nu_i} = \sqrt{2}h_{ii}w. \quad (1.44)$$

The physical particle content of the Higgs sector after symmetry breaking is made up of doubly charged $H^{\pm\pm}$, singly charged H^\pm and three neutral Higgs bosons, denoted H^0 , h^0 and A^0 . The singly charged H^\pm and the neutrals turn out to be mixtures of doublet and triplet fields, the doubly charged Higgs bosons on the other hand correspond directly to the triplet fields $\Delta^{\pm\pm}$.

1.5 Left-Right Symmetric Models

The basic motivation for proposing a Left-Right symmetric theory is the assumption that the observed parity violation in weak interactions is only a low-energy phenomenon. In such theories there are two W bosons W_1 and W_2 . The W_1 corresponds to the well-known W boson, which couples to left-handed currents and the W_2 , which must be heavier since it has not been discovered yet, couples to right-handed currents. Similarly, such theories predict two Z bosons, Z_1 and Z_2 , where the Z_1 corresponds to the familiar Z^0 with a mass

of 91 GeV. In the fermion sector, the theory contains the usual quarks and charged leptons and three light neutrino mass eigenstates ν_i ($i = 1, 2, 3$), which couple primarily to W_1 . Additionally, there are three heavy neutrino mass eigenstates N_i ($i = 1, 2, 3$), which couple to W_2 predominantly.

This particle spectrum is now grouped into doublets of left-handed and right-handed isospin:

$$\Psi_L^e = \begin{pmatrix} \nu_e \\ e^- \end{pmatrix}_L \leftrightarrow \left(\frac{1}{2}, 0, -1 \right) \quad \Psi_R^e = \begin{pmatrix} N_e \\ e^- \end{pmatrix}_R \leftrightarrow \left(0, \frac{1}{2}, -1 \right) \quad (1.45)$$

$$\Psi_L^q = \begin{pmatrix} u \\ d \end{pmatrix}_L \leftrightarrow \left(\frac{1}{2}, 0, \frac{1}{3} \right) \quad \Psi_R^q = \begin{pmatrix} u \\ d \end{pmatrix}_R \leftrightarrow \left(0, \frac{1}{2}, \frac{1}{3} \right). \quad (1.46)$$

The quantum numbers shown are $(T_L, T_R, B-L)$ where T_L is the left- and T_R the right-handed weak isospin, and $B-L$ is the difference of Baryon minus Lepton number. The last quantum number turns out to be the generator of the U(1) gauge group in Left-Right symmetric theories because the charge formula (1.1) now becomes:

$$Q = T_{L3} + T_{R3} + \frac{B-L}{2}. \quad (1.47)$$

The quantum number $B-L$ has an immediate physical interpretation, expressing the symmetry between quarks and leptons for the weak interaction. The hypercharge Y in the case of the SM has no such physical meaning. Some theorists consider this to be another ‘‘advantage’’ of Left-Right symmetric theories over the SM [17].

So the basic idea is to start from a gauge theory of $SU(2)_L \times SU(2)_R \times U(1)_{B-L}$, which breaks down to the familiar $SU(2)_L \times U(1)_Y$ for low energies because of the absence of the massive right-handed particles. The simplest Higgs sector required to establish this breakdown of gauge symmetry contains a bidoublet of Higgs fields Φ and two Higgs triplets $\Delta_{L,R}$:

$$\Phi \equiv \begin{pmatrix} \phi_1^0 & \phi_1^+ \\ \phi_2^- & \phi_2^0 \end{pmatrix} \leftrightarrow \left(\frac{1}{2}, \frac{1}{2}, 0 \right) \quad (1.48)$$

$$\Delta_L \equiv \begin{pmatrix} \Delta_L^+ & \sqrt{2}\Delta_L^{++} \\ \sqrt{2}\Delta_L^0 & -\Delta_L^+ \end{pmatrix} \leftrightarrow (1, 0, 2) \quad (1.49)$$

$$\Delta_R \equiv \begin{pmatrix} \Delta_R^+ & \sqrt{2}\Delta_R^{++} \\ \sqrt{2}\Delta_R^0 & -\Delta_R^+ \end{pmatrix} \leftrightarrow (0, 1, 2). \quad (1.50)$$

The notation for the triplet fields is again $\Delta = \vec{\tau}\vec{\Delta}$. The Higgs potential can be constructed such that the vacuum expectation values of these multiplets is:

$$\langle \Phi_0 \rangle = \frac{1}{\sqrt{2}} \begin{pmatrix} \kappa_1 & 0 \\ 0 & \kappa_2 \end{pmatrix} \quad (1.51)$$

$$\langle \Delta_{L,R} \rangle = \frac{1}{\sqrt{2}} \begin{pmatrix} 0 & 0 \\ w_{L,R} & 0 \end{pmatrix} \quad (1.52)$$

Very similarly to (1.40) the ρ parameter condition becomes:

$$\rho = \frac{m_{W_1}^2}{m_{Z_1}^2 \cos^2 \theta_W} = \frac{1 + \frac{2w_L^2}{v^2}}{1 + \frac{4w_L^2}{v^2}} \quad v^2 = \kappa_1^2 + \kappa_2^2. \quad (1.53)$$

This limits the size of $w_L \ll v$. Additionally, based on the most general form of the Higgs potential, it was shown in [18], that κ_2 must be small or even zero in order to avoid FCNCs. The Higgs triplets couple to the fermions in the same way as in equation (1.43):

$$\mathcal{L}_{int} = ih_{L,ij}(\Psi_{iL}^T C \tau_2 \Delta_L \Psi_{jL}) + ih_{R,ij}(\Psi_{iR}^T C \tau_2 \Delta_R \Psi_{jR}) + h.c. \quad (1.54)$$

Again these couplings generate Majorana mass terms for neutrinos of type (1.44). But in contrast to the model of section 1.4, the Left-Right symmetric model also contains the right-handed neutrino states N_R and the Dirac mass terms, which mediate transitions between left-handed and right-handed neutrinos. Therefore, this model leads to a so-called see-saw mechanism [19, 20, 21] for neutrino masses.

The physical particle content of the Higgs sector of this model after symmetry breaking contains 4 doubly charged Higgs $H_L^{\pm\pm}$ and $H_R^{\pm\pm}$, which correspond directly (no mixing between multiplets) to the $\Delta_L^{\pm\pm}$ and $\Delta_R^{\pm\pm}$ fields. Then there are also 4 singly charged and 6 neutral Higgs bosons, which are mostly mixtures between doublet and triplet fields.

1.6 Doubly charged Higgs at HERA

1.6.1 Production and Decay of the doubly charged Higgs

Because of charge conservation, the $H^{\pm\pm}$ cannot couple to a pair of quarks or a quark-antiquark pair directly. Therefore, they cannot be produced in the s-channel at an electron-proton collider⁵. However, they can couple to leptons and therefore they can be produced at the electron vertex of an ep-event via Yukawa couplings to electrons (see Figure 1.2). The incoming electron is scattered from a photon γ or Z^0 from the proton and radiates the doubly charged Higgs. The incoming lepton undergoes a charge inversion and eventually even a change in lepton flavour, e.g. $e^- \gamma \rightarrow H^{--} l^+$ and $e^+ \gamma \rightarrow H^{++} l^-$.

Unlike for the SM Higgs Boson, where the couplings to fermions are proportional to the mass of the fermions (see equations (1.33) and (1.34)), the doubly charged Higgs couples to leptons by a priori independent, unknown couplings $h_{ll'}$, where $l, l' = e, \mu, \tau$. Only the neutral Higgs bosons of the different multiplets are involved in the mass generation for the fermions. For $l \neq l'$ lepton flavour is violated. The decay width for the decay into a pair of identical leptons depends quadratically on the coupling. For a $T = 1$ and $Y = 2$ triplet the decay width is [22]:

$$\Gamma(H^{++} \rightarrow l^+ l^+) = \frac{|h_{ll}|^2}{8\pi} m_{H^{++}}. \quad (1.55)$$

⁵For a brief description of HERA see section 2.1.

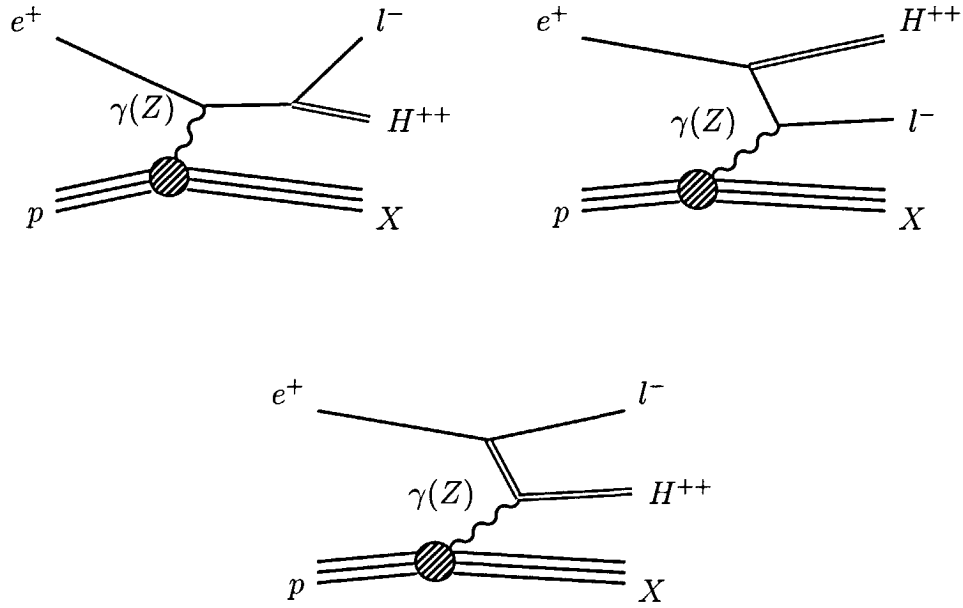


Figure 1.2: Feynman diagrams for tree level H^{++} production at HERA via the Yukawa process.

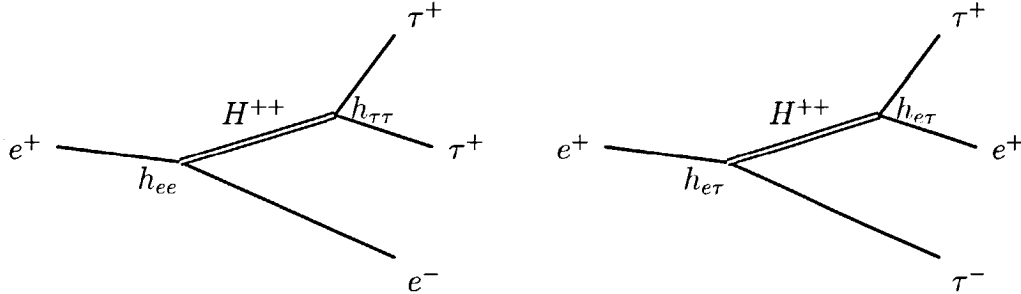


Figure 1.3: Feynman diagrams for H^{++} production and decay. The couplings involved in the processes $e\gamma \rightarrow eH^{\pm\pm} \rightarrow e\tau\tau$ and $e\gamma \rightarrow \tau H^{\pm\pm} \rightarrow \tau e\tau$, as well as the charge and flavour of the scattered lepton are indicated.

Other decay modes of doubly charged Higgs are possible [23]. Decays into W -pairs, pairs of singly charged Higgs or even mixed decays into one singly charged Higgs and a W boson can be considered. However, in this analysis it is assumed that the doubly charged Higgs is the lightest Higgs boson and therefore decays into H^\pm can be discarded. Additionally, the mass range considered for the doubly charged Higgs is $80 \leq M_{H^{\pm\pm}} \leq 150$ GeV. Therefore, the decay into W -pairs is also discarded.

In this thesis the decays of doubly charged Higgs into τ -pairs and the lepton flavour violating decay $H^{\pm\pm} \rightarrow e\tau$ are studied. For abbreviation these two decay topologies will be called $\tau\tau$, and $e\tau$ respectively throughout this analysis. The couplings involved in these processes are (see Figure 1.3) $h_{e\tau}$ and $h_{\tau\tau}$. The $\tau\tau$ final state requires additionally

a coupling $h_{el} \neq 0$ at the production vertex, e.g. in this analysis $h_{ee} \neq 0$ is assumed. However, the flavour of the scattered lepton is only of small importance since in section 3.2 it is shown that it is mostly undetected in the final state. The decays into other lepton pairs are studied in separate H1 analyses [3].

1.6.2 Doubly charged Higgs at other colliders

1.6.2.1 LEP

In addition to the Yukawa process (see Figure 1.2) there are two other processes at tree level at LEP (see Figure 1.4).

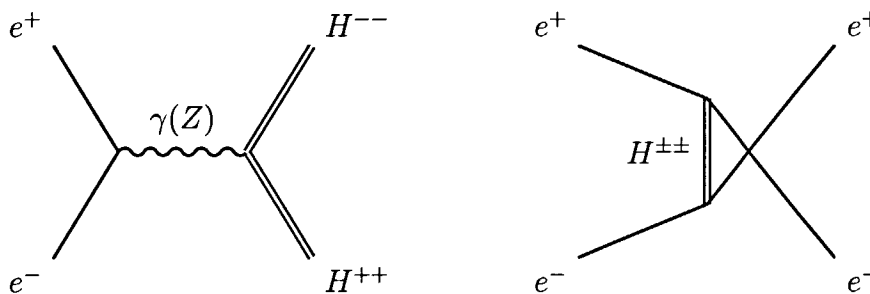


Figure 1.4: Feynman diagrams for $H^{\pm\pm}$ pair production and Bhabha scattering via doubly charged Higgs exchange at LEP

The s-channel pair production process (left) has a significantly larger cross section than the single production via Yukawa couplings but has the disadvantage that the accessible mass range for this process is limited to half of the available centre of mass energy ($\sqrt{s}/2$). Limits have been set for this channel by the OPAL [24], L3 [25] and DELPHI [26] experiments. The conclusion from these publications is basically that doubly charged Higgs bosons are excluded for masses below ~ 98 GeV.

The contribution from Bhabha scattering (see Figure 1.4, right) is sensitive to the coupling h_{ee} . Its contribution to the total Bhabha scattering cross section is estimated in [18] and limits on h_{ee} are derived from OPAL [27] and L3 [25].

The only LEP experiment, which provides limits for the single production of doubly charged Higgs via Yukawa couplings, is OPAL [27].

1.6.2.2 Tevatron and LHC

At hadron colliders the Drell-Yan pair production process is also possible (see Figure 1.5) via quark-antiquark annihilation. But this channel contributes significantly only at $p\bar{p}$ colliders (Tevatron) because for pp colliders such as LHC the antiquark content in the proton is suppressed. The antiquark would have to be a seaquark in that case. Instead for LHC the single production of $H^{\pm\pm}$ via W -fusion is the dominant production mechanism. Even a fusion of singly charged Higgs H^\pm instead of the W s can be considered, since e.g. in all

Higgs triplet models there have to be also singly charged Higgs bosons and these do couple to quarks and antiquarks directly.

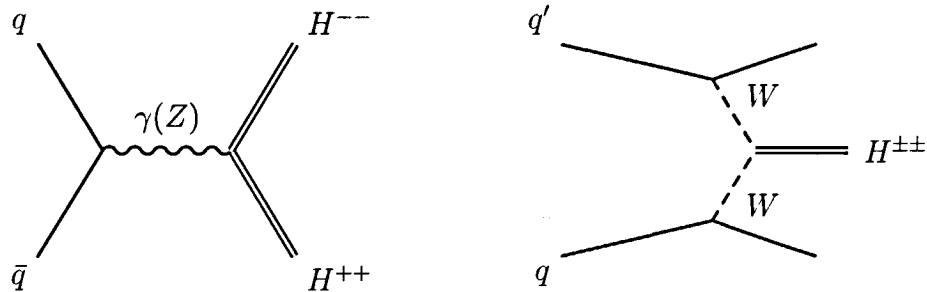


Figure 1.5: Feynman diagrams for $H^{\pm\pm}$ pair production and single production via W -fusion at Tevatron and LHC

Limits for the Drell-Yan pair production process have been set at Tevatron from the D0 [28] and CDF [29] experiments. These limits distinguish between left-handed and right-handed doubly charged Higgs because the couplings to the Z^0 boson are different (see also section 1.5)

The Yukawa process is of course not possible at hadron colliders because of the absence of leptons at tree level.

1.7 The HTM MC Generator

A dedicated MC⁶ generator (named HTM) for producing simulated events with doubly charged Higgs particles via all possible couplings $h_{ll'}$ has been written for HERA [30]. The generator calculates the matrix element for doubly charged Higgs production and produces events in each point of the phase space according to its differential cross section. Depending on the magnitude of the momentum squared Q^2 of the exchanged photon (see Figure 1.2) a different approach for the treatment of the proton vertex is used. The following Q^2 ranges are distinguished:

- **Elastic ($Q^2 = 0 \text{ GeV}^2$)**

The proton stays intact.

- **Quasielastic ($0 < Q^2 < 4 \text{ GeV}^2$)**

The proton-photon vertex is calculated using the SOPHIA package [31].

- **Inelastic ($Q^2 > 4 \text{ GeV}^2$)**

Electron quark scattering is modelled by the use of parton density functions (pdf) (see e.g. [4]) for different quarks in the initial state of the proton. Only u, \bar{u}, d, \bar{d} are considered. For this analysis the leading order pdf with the label CTEQ 4L [32] is used. The Lund fragmentation model as implemented in JETSET [33] determines the hadronic final state.

The total production cross sections are shown as a function of the Higgs mass in Figure 1.6 (coupling h_{ee}) and 1.7 (coupling $h_{e\tau}$). All cross sections drop exponentially with increasing Higgs mass as is shown by the fit. While the normalisations of the different cross sections are arbitrary (because of the arbitrary choice of $h_{ee}, h_{e\tau}$ respectively), the relative contributions of the different Q^2 régimes are independent of the coupling. For a Higgs mass of 100 GeV and a proton momentum of 920 GeV these relative contributions are summarised in Table 1.3.

| Kinematic Régime | Coupling | |
|-------------------------------|----------|-------------|
| | h_{ee} | $h_{e\tau}$ |
| $\sigma_{ela}/\sigma_{tot}$ | 53% | 38% |
| $\sigma_{quasi}/\sigma_{tot}$ | 27% | 37% |
| $\sigma_{inela}/\sigma_{tot}$ | 20% | 25% |

Table 1.3: *Relative contributions to the total Higgs production cross section of the different kinematic régimes for the couplings h_{ee} and $h_{e\tau}$.*

For the h_{ee} coupling, the elastic Higgs production is by far the most important. This is no longer true in the case of $h_{e\tau}$. The reason for this is the contribution of the top right graph in Figure 1.2. In this graph a photon emitted by the proton splits up into a lepton pair, which then combines with the incoming electron to the doubly charged Higgs. If the

⁶The abbreviation MC is used for “Monte Carlo” throughout this analysis.

Higgs was produced via the $h_{e\tau}$ coupling, then the lepton pair has to be a τ -pair, which is suppressed for very small Q^2 because of the non negligible τ mass.

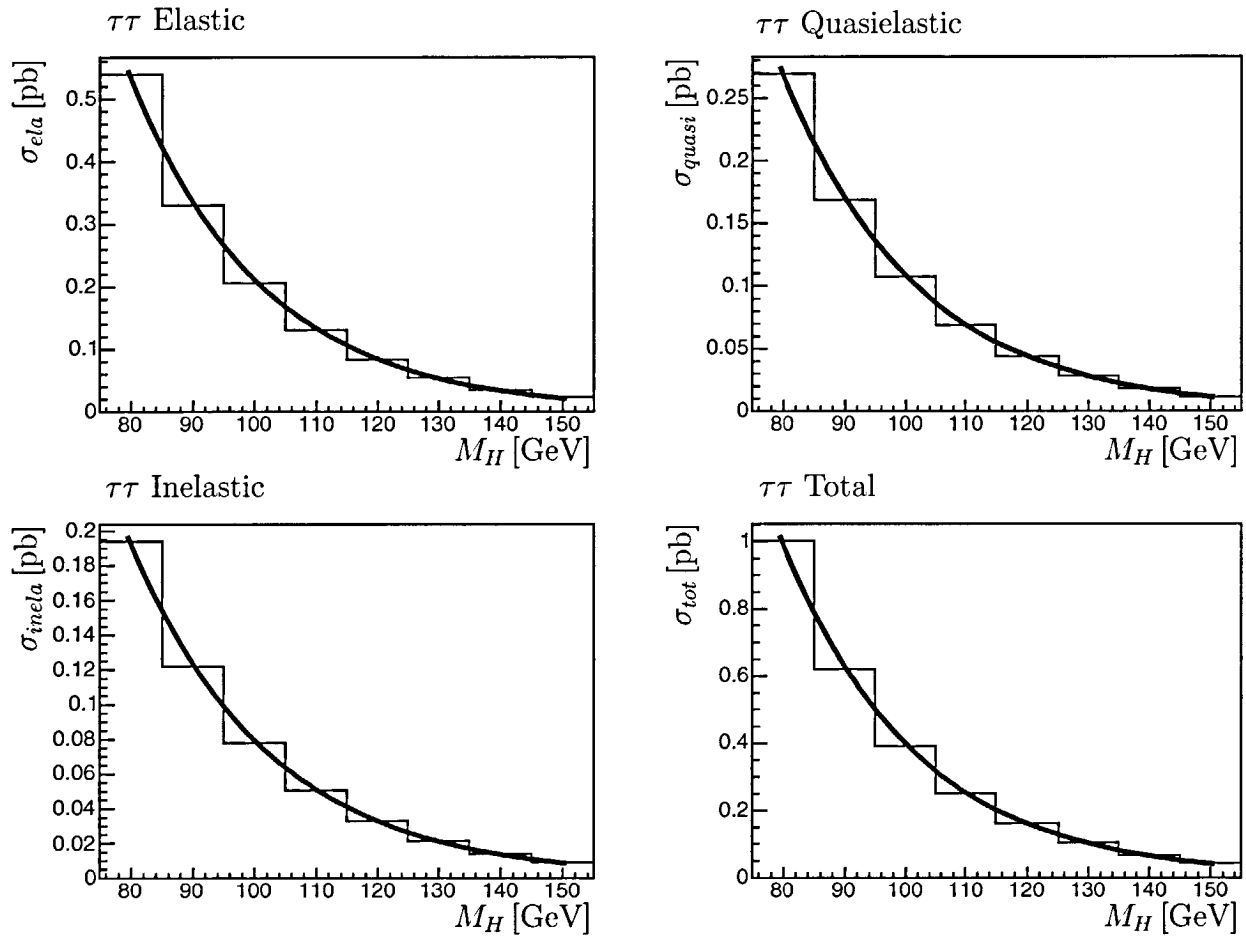


Figure 1.6: Higgs production cross sections for a coupling constant $h_{ee} = h_{\tau\tau} = 0.3$ for the different Q^2 ranges as a function of the Higgs mass in steps of 10 GeV. All other couplings are assumed zero. Note that the coupling $h_{\tau\tau}$ governs the decay, but is irrelevant for the Higgs production cross section. The line represents an exponential fit.

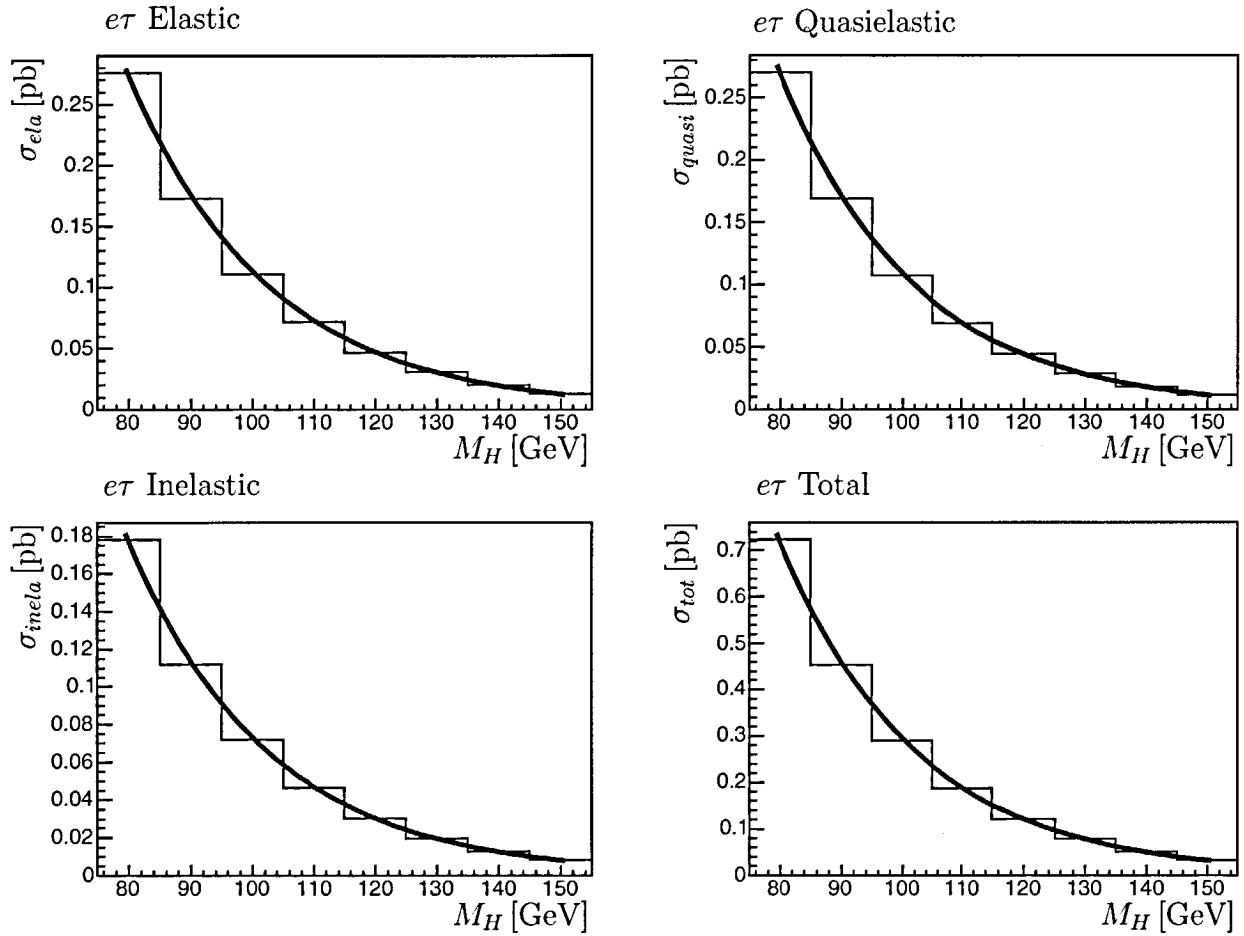


Figure 1.7: Same distributions as shown in Figure 1.6 but with the coupling constant $h_{e\tau} = 0.3$. All other couplings are assumed zero.

Seite Leer /
Blank leaf

Chapter 2

The H1 Experiment at HERA

2.1 The HERA accelerator

The “Hadron Electron Ring Accelerator” (HERA) is an electron proton collider located at the “Deutsches Elektron Synchrotron” (DESY) facility in Hamburg. The accelerator has a circumference of 6.3 km and consists of two separate rings, one for protons and the other for electrons or positrons. These rings are merged in the two interaction regions (see Figure 2.1) where the H1 and ZEUS experiments are located.

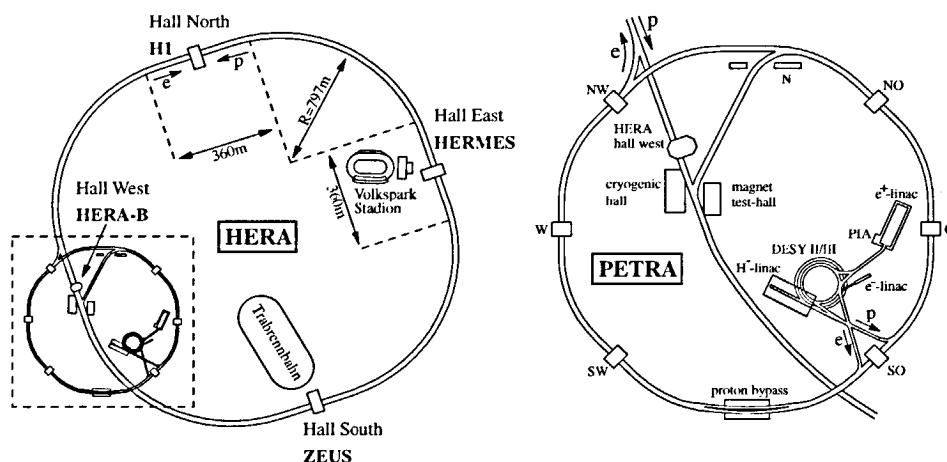


Figure 2.1: The HERA (left) and PETRA (right, enlarged section from the left) accelerator rings at DESY. PETRA serves as preaccelerator for electrons and protons. The colliding beam experiments H1 and ZEUS are located in the Hall North and Hall South respectively.

The proton beam is accelerated up to a final energy of 920 GeV^1 and the electron beam up to 27.5 GeV , which corresponds to a centre of mass energy of 320 GeV . The lateral dimensions² of the two beams are typically $190 \mu\text{m} \times 50 \mu\text{m}$ and the overlap region, which is referred to as *beam spot*, is measured to be $137 \mu\text{m} \times 37 \mu\text{m}$. The beams are not continuous

¹Until the year 1998 proton energy was 820 GeV and the corresponding centre of mass energy 300 GeV .

²All values are 1-sigma extensions in x and y from the beam centre and may vary over different runs.

but consist of particle bunches 96 ns apart. The bunch crossing (BC) rate is therefore 10.4 MHz. The maximal number of bunches, which can be stored in each beam is 210.

2.2 The H1 experiment

In this section, the most relevant subdetectors for this analysis are briefly described. A more detailed description of the H1 detector can be found in [34]. Figure 2.2 shows a schematic view of the open H1 detector. In the top right corner the *H1 coordinate system* is defined:

- The positive z -axis points in the direction of the proton beam.
- The x - and y -axis are perpendicular to the beams. The x -axis points towards the centre of the HERA accelerator.
- The polar angle θ is the angle between the z -axis and a given direction (e.g. particle).
- The azimuthal angle is called ϕ .

Because of the asymmetric beam energies, the proton (electron) beam direction is also often referred to as *forward (backward)* direction.

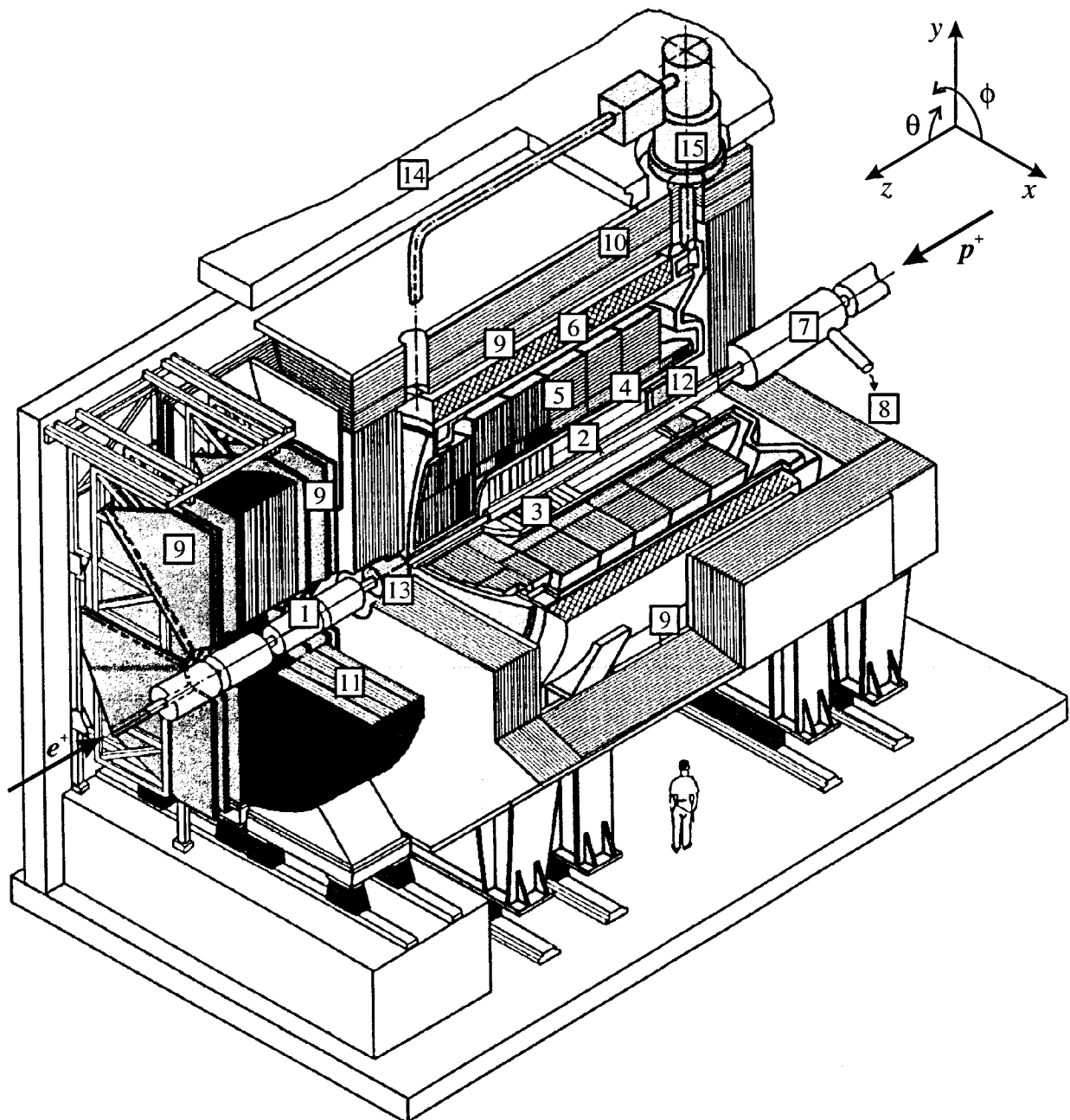


Figure 2.2: View of the H1 detector and the definition of the coordinate system. Legend: [1] Beam pipe and beam magnets, [2] Central tracking chambers, [3] Forward tracking and Transition radiators, [4] Electromagnetic Calorimeter, [5] Hadronic Calorimeter, [6] Superconducting coil, [7] Compensating magnet, [8] Helium cryogenics, [9] Muon chambers, [10] Instrumented Iron, [11] Muon toroid magnet, [12] Backward calorimeter, [13] Plug calorimeter, [14] Concrete shielding, [15] Liquid Argon cryostat

2.2.1 Central Jet Chamber

The most important device for track reconstruction is the *Central Jet Chamber (CJC)*. A side view of the H1 tracking system is shown in Figure 2.3.

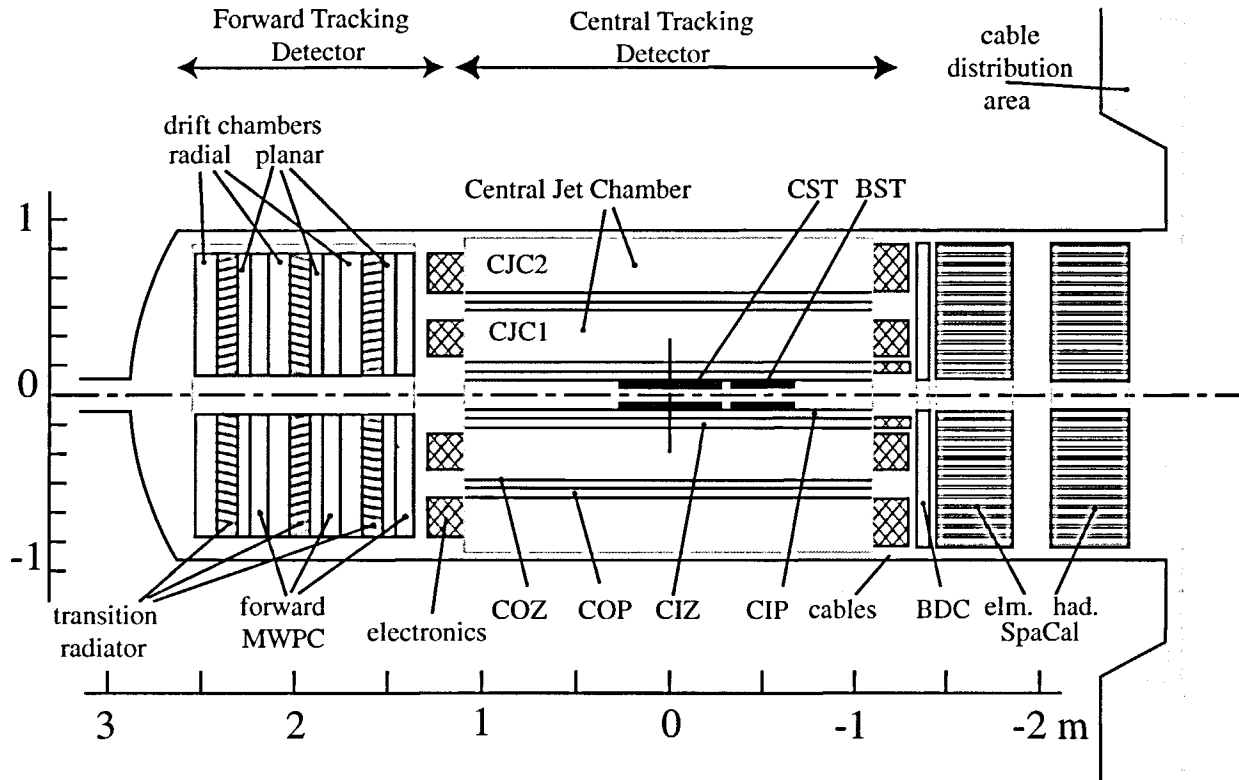


Figure 2.3: Side view of the H1 tracking system.

The CJC is a drift chamber consisting of two cylindrical volumes (CJC1 and CJC2) mounted concentrically around the beam pipe. In the azimuthal direction the CJC1 (CJC2) is divided into 30 (60) identical drift cells by cathode wire planes. Inside each drift cell 24 (32) anode sense wires are strung parallel to the beam (z -axis).

Charged particles passing through the CJC are bent in the magnetic field of 1.15 T created by the superconducting solenoid (see Figure 2.2). Along their trajectories gas molecules from the chamber are ionised and the free ionisation charge (electrons) drift towards the sense wires where they produce an electric signal. By measuring the drift times of the charge deposits in the different sense wires, the particle's track can be reconstructed in the $r\phi$ -plane. An $r\phi$ hit resolution of $\sigma_{r\phi} \approx 140 \mu\text{m}$ is achieved. This translates to a resolution in transverse momentum of $\sigma(p_t)/p_t^2 = 0.5\% \text{ GeV}^{-1}$ [35]. The z position can be measured at each sense wire by charge division of the signals obtained at the two wire ends. Two additional drift chambers, the so-called CIZ and COZ (see Figure 2.3), are mounted inside (CIZ) and outside (COZ) the CJC1. With their sense wires perpendicular to the beam they greatly enhance the z measurement and the θ resolution.

The geometrical boundaries and polar angle (θ) acceptance for CJC1 and CJC2 are

summarised in Table 2.1.

| | Radius [mm] | | z [mm] | | θ [°] | |
|------|-------------|-------|--------|------|--------------|-----|
| | inner | outer | min | max | min | max |
| CJC1 | 203 | 451 | -1125 | 1075 | 11 | 170 |
| CJC2 | 530 | 844 | -1125 | 1075 | 26 | 154 |

Table 2.1: *CJC geometry*

2.2.2 Calorimeter

In order to measure particle energies, H1 has a *liquid argon (LAR)* calorimeter surrounding the central tracker [36]. The inner, electromagnetic (EMC) part of the calorimeter is dedicated to identify electrons and photons, and the outer, hadronic (HAC) part is dedicated to measure charged and neutral hadrons (see Figure 2.4).

The calorimeter consists of stacks of absorber plates (lead in EMC, stainless steel in HAC) with gaps in between, which are filled with liquid argon. A high energetic particle passing through the calorimeter produces a particle shower in the absorber plates, which can then be measured by the charge deposition in the liquid argon.

The calorimeter is segmented in z into 8 different “wheels” and each “wheel” is furthermore segmented into 8 octants in ϕ . This leads to small insensitive areas called *cracks* between the segments. The total polar angle acceptance of the calorimeter is $4^\circ \lesssim \theta \lesssim 154^\circ$.

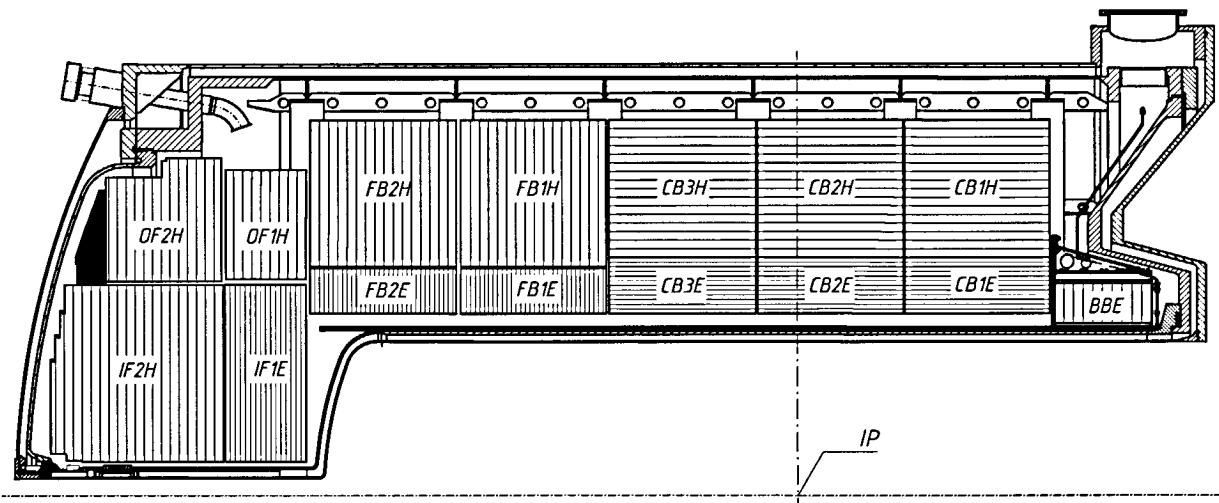


Figure 2.4: Side view of the upper half of the liquid argon calorimeter. The label “IP” denotes the nominal interaction point. Darker shaded regions belong to the electromagnetic part, lighter shaded regions belong to the hadronic part of the calorimeter.

2.2.2.1 Spaghetti Calorimeter (SPACAL)

In the backward (electron beam) direction a lead/scintillating fibre calorimeter, the so-called “*Spaghetti Calorimeter (SPACAL)*” covers the polar angle region of $153^\circ \lesssim \theta \lesssim 177.5^\circ$. Its main purpose is the energy and position measurement of the scattered electron in deep inelastic scattering events. The position resolution of the SPACAL is 4 mm.

2.2.3 Instrumented Iron

The instrumented iron yoke (see Figure 2.2) surrounds all previously described detector components of H1. It serves as return yoke for the magnetic flux and is used for the detection of minimum ionising particles. It is divided into forward ($4^\circ \lesssim \theta \lesssim 34^\circ$) and backward ($127^\circ \lesssim \theta \lesssim 175^\circ$) endcaps and a barrel region ($34^\circ \lesssim \theta \lesssim 127^\circ$). The instrumentation consists of streamer tubes [37], which are inserted between 10 iron sheet layers of 75 mm thickness [38]. The gas filled tubes have a cross section of $10 \times 10 \text{ mm}^2$ and they have a single sense wire strung in the centre. The top sides of the layers are equipped with strip or pad cathodes. The strip cathodes are glued perpendicular to the sense wires such as to obtain a 2-dimensional spatial resolution of 3 to 4 mm in those layers.

2.2.4 Trigger and Data Acquisition

The purpose of the H1 Trigger system [39] is to trigger the readout of the frontend electronics of the detector for ep interactions. The trigger consists of 4 trigger levels L1 to L5³ with increasing decision times (see Figure 2.5). With a BC frequency of 10.4 MHz the input rate for the L1 trigger level is typically around 100 kHz. The L1 decision time is set to $2.3 \mu\text{s}$. Within this time span all trigger signals (*trigger elements (TE)*) from all subdetectors relevant for the trigger have to be transmitted to the *central trigger* logic, where they are logically combined to a set of 128 *subtriggers*. These subtriggers produce the central trigger decision, which has to be transmitted back to all detector subsystems, still within the L1 decision time. In case of a positive L1 trigger decision the pipeline in the frontend electronics is stopped and no more input data is accepted. The output rate of L1 is up to 1 kHz. Some L1 subtriggers are *prescaled* in order to keep the rate small. A prescaled subtrigger with prescale factor n is considered only for every n^{th} positive trigger decision.

On level L2, the L1 trigger decision is validated and additional topological and neural network based criteria are applied. The L2 decision is made after $20 \mu\text{s}$ and it reduces the rate to about 50 Hz. After a positive L2 decision the event is read out, which takes typically 1 to 2 ms per event. After readout (or rejection on L2) the frontend pipeline is restarted.

On level L4, a multi processor farm performs a fast reconstruction of each event, whereby the rate is reduced to typically 10 Hz, which is then written to tape. This raw data is then run through the full reconstruction on a dedicated computer farm, the so-called

³The third trigger level (L3) has not been implemented for the data taking period considered in this analysis.

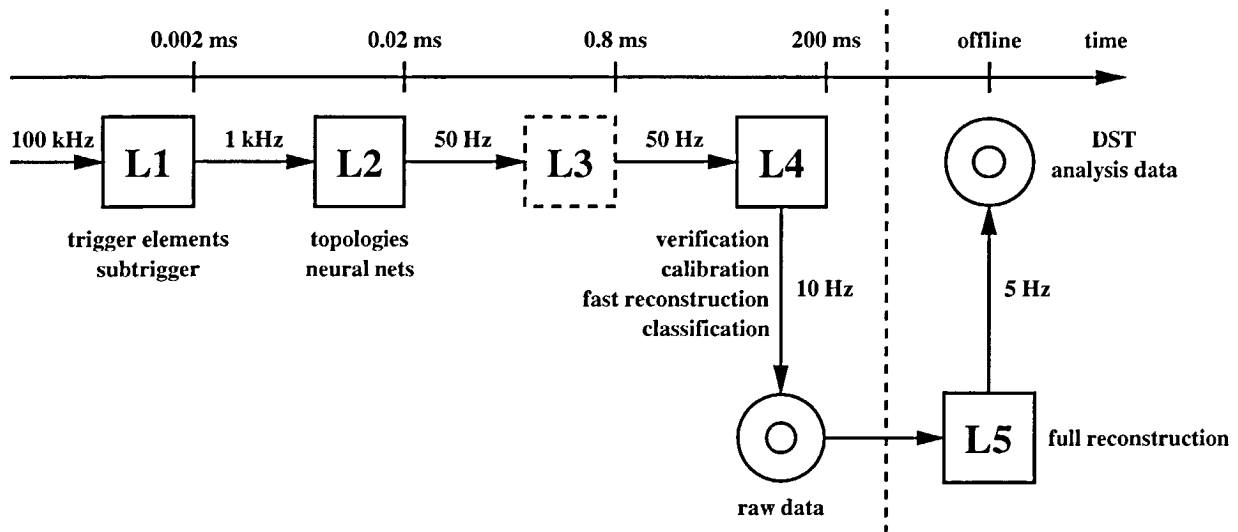


Figure 2.5: Schematic of the different trigger levels, their decision times and the data acquisition of the H1 experiment.

level L5. This process runs asynchronously to the readout.

2.2.4.1 L1 Trigger Elements of this analysis

- DCRPh_THig
The $DCr\phi$ trigger compares digitised CJC hits from 10 wire layers with predefined (track) masks. It allows to trigger on coarse track parameters and multiplicities. DCRPh_THig requires at least one track with transverse momentum $P_T > 800$ MeV.
- DCRPh-Ta, DCRPh-Tc
At least one (a), or three (c) tracks respectively with transverse momentum $P_T > 420$ MeV.
- LAr_electron>1
For triggering purposes several adjacent LAr cells are grouped into larger areas pointing approximately to the nominal vertex. These groups of cells are called *trigger towers* [40]. For LAr_electron>1 the energy in the electromagnetic part of one trigger tower must exceed a threshold of 5 GeV.
- LAr_Etmiss>1,2
The vectorial sum of the transverse energy ($\sqrt{E_x^2 + E_y^2}$) over all trigger towers exceeds the nominal threshold of 4.4 GeV (1) or 5.2 GeV (2).
- LAr_BR
A trigger tower exceeds an energy threshold of 1 GeV and has a matching track from the proportional chambers (CIP/COP) (see Figure 2.3).

- LAr_IF
The energy sum over all trigger towers in the IF region of the calorimeter (see Figure 2.4) exceeds the threshold of 2 GeV.
- Mu_ECQ
Muon in the outer endcap of the instrumented iron.
- Mu_Bar
Muon in the barrel region of the instrumented iron.
- SPCLe_IET>1
Inclusive electron trigger in the SPACAL above the threshold of 2 GeV.

2.2.5 Luminosity System

The luminosity is determined by the rate of Bethe-Heitler processes, which is $ep \rightarrow ep\gamma$. The cross section for this process can be calculated in QED to an accuracy of 0.3%. The angular distributions of the scattered electron and photon are strongly peaked at low scattering angles. This means that they have to be measured with specially installed devices downstream the electron beam line and close to the beam. The electron tagger (ET) is located at $z = -33$ m and the photon tagger (PD) is at $z = -103$ m (see Figure 2.6).

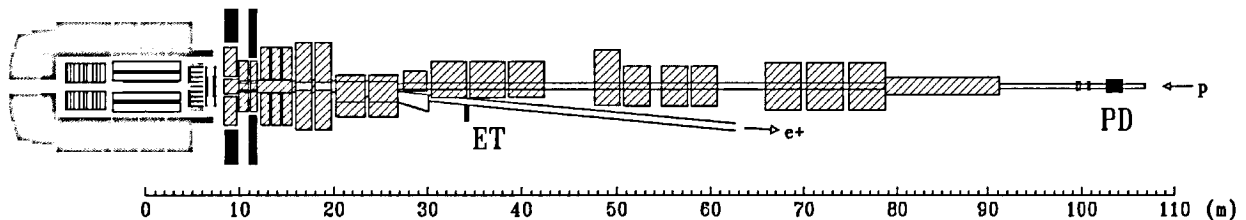


Figure 2.6: *The H1 Luminosity System*

The main background from Bremsstrahlung $eA \rightarrow eA\gamma$, where A denotes an atom from the residual beam-gas, can be taken into account from the rate measurement for non-colliding bunches, the so-called *satellite bunch correction*.

$$\mathcal{L} = \frac{R_{tot} - (I_{tot}/I_0)R_0}{\sigma_{vis}} \quad (2.1)$$

In equation (2.1) R_{tot} is the total measured coincidence rate of electron and photon tagger, R_0 is the rate for the pilot bunches and I_{tot} , I_0 are the corresponding electron beam currents. σ_{vis} is the total visible Bethe-Heitler cross section.

2.3 Simulation of the H1 Experiment

The detector response for generated MC events is simulated in detail with the GEANT (version 3.15) software [41], which is used by the H1 simulation package H1SIM. GEANT incorporates many physical processes, like e.g. energy loss, multiple scattering and secondary particle production. Long lived generated particles are propagated through a virtual detector and their full interaction with the detector material (including dead material) is simulated. The energy deposits in active detector volumes is translated into detector signals according to measured performance figures. These simulated events are then fed into the H1 reconstruction software H1REC, which produces events that have exactly the same format as real data.

In this analysis, signal efficiencies and background rates are determined purely from MC simulation. It is therefore important to achieve an agreement between data and MC in order to justify the results of this analysis.

Seite Leer /
Blank leaf

Chapter 3

Preselection

The goal in this chapter is to identify the candidates for the decay particles originating from the doubly charged Higgs decay and to remove most of the background from the available data sets. The basic guidance for this purpose is the signal topology obtained from the MC generator discussed in section 1.7 and the constraints from the experiment discussed in chapter 2. The topology of a massive doubly charged Higgs decaying into lepton pairs consists essentially of two isolated, back to back particles with high transverse momentum and only little or no additional activity in the detector. Therefore, in a first step the candidates for the Higgs decay particles are selected from tracks with high transverse momentum in the central region of the detector. Furthermore, the candidate tracks are required to be back to back. Events are then classified according to whether the candidate tracks belong to an identified electron, muon or nothing of both. Trigger conditions and non ep background suppression criteria are imposed. No distinction is made between the $\tau\tau$ and $e\tau$ topology on the preselection level, which means that the final selection cuts (see chapter 4) are applied to exactly the same preselected subsample.

3.1 Data Sets

The data sets used in this analysis comprise the data from the HERA I running period of the years 1996, 1997, 1999 and 2000. Table 3.1 shows the lepton beam charge, the centre of mass energy (\sqrt{s}) and the collected luminosity (all subtriggers) by H1 for the different years. The higher centre of mass energy in the years ≥ 1998 became possible by an increased proton momentum of 920 GeV (before: 820 GeV).

The luminosity is given after the following corrections:

- Run¹ quality: All runs are assigned a quality, which can be poor, medium or good. A poor run is a run where at least one major detector component such as CJC or LAr calorimeter is off. This analysis considers only medium or good quality runs.
- Trigger phase: From the beginning until the end of a luminosity fill² different running

¹A run is a data taking period, for which the detector conditions and trigger settings are constant.

²A luminosity fill is one filling of the HERA accelerator with electron and proton bunches.

| Year | Lepton Beam Charge | \sqrt{s} [GeV] | Luminosity [pb^{-1}] |
|--------------|--------------------|------------------|---------------------------------|
| 1996 | + | 300 | 7.47 |
| 1997 | + | 300 | 18.85 |
| 1999 | + | 318 | 14.20 |
| 2000 | + | 318 | 47.60 |
| Total | | | 88.12 |

Table 3.1: *Properties of the different data sets used.*

conditions with different rates of non- ep physics are passed through. The central trigger has different prescale schemes called trigger phases to adapt to these different background situations. For stable ep -running conditions the trigger phase must be between 2 and 4.

- High voltage requirement: High voltage “on” is required for the following systems used in the analysis: CJC, Luminosity System, LAr calorimeter, SPACAL, instrumented iron.
- Satellite bunch correction as described in section 2.2.5.
- Dead-time correction: When an event passes the L1 trigger, the pipeline is stopped and H1 does not read in new events until the triggered event is read out or rejected by a higher trigger level. This so-called dead-time is typically of the order of a few percent. It is calculated run-wise.

Not all HERA I data sets are used in this analysis. Most importantly the e^- data collected in the years 1998 and 1999 and corresponding to a luminosity of about 11 pb^{-1} is discarded due to bad background conditions and an unacceptably low tracking efficiency [42]. Especially for the isolation criteria discussed in section 4.2 a good tracking efficiency is required. Other run periods were discarded also, namely runs with a shifted z-vertex position and runs with a so-called minimum bias trigger setup were discarded.

Because of uniformly continuous running conditions, the years of 1996, 1997 and the years 1999, 2000 are combined together. Therefore, the analysis distinguishes only two data sets, which are hereafter called the 96/97 and 99/00 data set, respectively. All MC used to compare with the 96/97 data set was simulated and reconstructed for 1997 running conditions and the MC used to compare with the 99/00 data set was simulated and reconstructed for 1999 and 2000 running conditions.

3.2 Selection of the candidates

The selection of particle candidates originating from a heavy doubly charged Higgs starts from tracks. Only tracks, which fulfil a standard set of quality criteria, the so-called Lee West track criteria [43], are considered throughout this analysis. Additionally, tracks pointing to calorimeter cracks (see section 2.2.2) are discarded, because the electron identification efficiency for electrons going into cracks is much reduced.

First the transverse momentum P_T and the pseudorapidity η of the tracks are studied. These two quantities are defined as:

$$P_T = \sqrt{p_x^2 + p_y^2} \quad \text{and} \quad \eta = -\log \left(\tan \frac{\theta}{2} \right). \quad (3.1)$$

See section 2.2 for the definition of the x and y directions as well as the polar angle θ . The pseudorapidity is approximately equal to the rapidity³, if the mass of the particle is small compared to its energy. The advantage of this quantity over the polar angle is that rapidity differences are invariant under Lorentz boosts. The pseudorapidity is monotonically decreasing with increasing polar angle and is zero for a polar angle of 90 degrees.

Figure 3.1 shows the P_T and η distributions of the Higgs decay particles on generator level for a signal MC of elastically produced H^{++} of a mass of $M = 100$ GeV. Each plot contains two entries per event, one for each daughter particle of the Higgs. The plots on the left (right) side were done for a Higgs decay into $\tau\tau$ ($e\tau$).

³The rapidity is well-known from special relativity theory

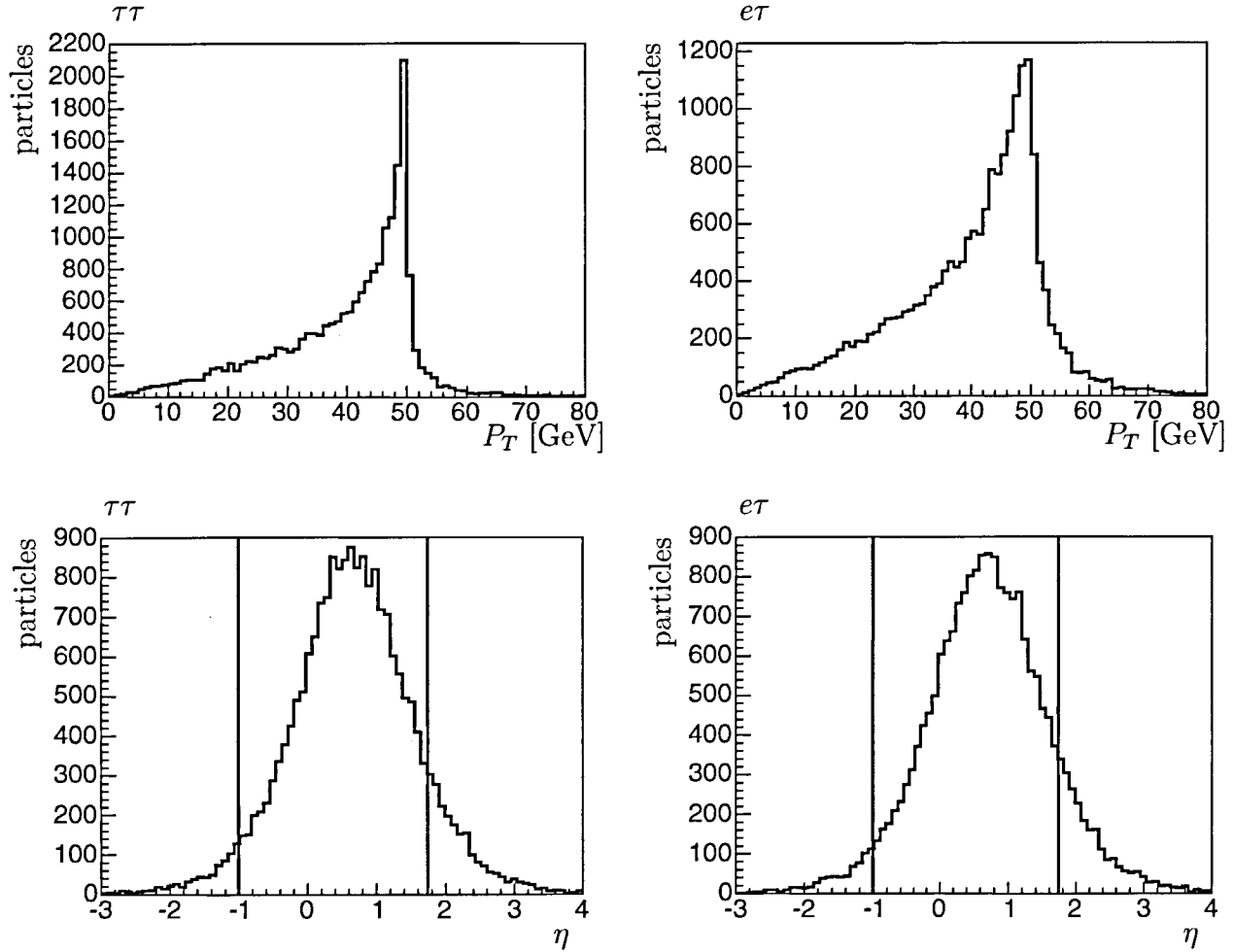


Figure 3.1: Generator level P_T (upper) and η (lower) spectra of the Higgs decay particles for $\tau\tau$ (left) and $e\tau$ (right). The vertical bars in the η distributions denote the central region, in which the candidates are required to be.

The candidates have a tendency to go in the forward direction. This effect gets even stronger as the Higgs mass increases, because a heavier Higgs means that a larger fraction of the proton's energy is required for its production. Thus, the Higgs gets boosted in the proton direction. Nevertheless, the CJC acceptance (see section 2.2.1) requires tracks in the central region. The cut chosen here is:

$$\text{Candidate tracks within } 20^\circ \leq \theta \leq 140^\circ$$

The cut is indicated by the vertical bars in the η distributions of Figure 3.1. In the case of a 100 GeV Higgs about 80% of the candidates end up in the acceptance region. Additionally, a veto against ep events with small electron scattering angles is used:

No identified electron⁴ in the SPACAL ($153^\circ \lesssim \theta_e \lesssim 177.5^\circ$)

The total cross section for deep inelastic scattering in ep -collisions is proportional to $1/Q^4$, where Q^2 is the square of the transferred momentum of the exchanged photon. By using the lepton inelasticity y , Q^2 can be related to the transverse momentum of the final state particles by [44]:

$$Q^2(1-y) = P_{T,hfs}^2 = P_{T,e}^2. \quad (3.2)$$

$P_{T,hfs}$ and $P_{T,e}$ are the transverse momenta of the hadronic final state and the scattered electron respectively. The last equality in (3.2) holds because in neutral current reactions the scattered electron balances the momentum of the hadronic final state. A steeply falling cross section in Q^2 is therefore also steeply falling in P_T and consequently it is a good idea to cut on the transverse momentum of the candidates in order to reduce the neutral current background⁵. All tracks in an event in the accepted θ region are P_T -ordered. The two tracks with largest transverse momentum are considered as candidates. They must meet the following requirements:

$$\begin{array}{ll} \text{Faster candidate track} & P_T > 10 \text{ GeV} \\ \text{Slower candidate track} & P_T > 5 \text{ GeV} \end{array}$$

In Figure 3.2 the P_T spectra of the faster versus the slower candidate for $\tau\tau$ (left) and $e\tau$ (right) are displayed. Again, the MC samples used contain elastically produced Higgs of a mass of 100 GeV. Because a large fraction of the original τ momentum is carried away undetected by one or more neutrinos, these P_T spectra are already much softer than the spectra from Figure 3.1. For the $e\tau$ channel (right) it has to be noted that the electron candidate has a much harder P_T spectrum than the τ candidate and therefore it almost always fulfils the P_T requirement on the faster candidate. Therefore, the τ candidate for $e\tau$ only has to fulfil the requirement on the slower candidate (vertical line). It should also be noted, that the transverse momentum of all candidates increases with increasing Higgs mass.

⁴Electron identification is described in section 3.5.1

⁵The different backgrounds are discussed in section 3.7.1

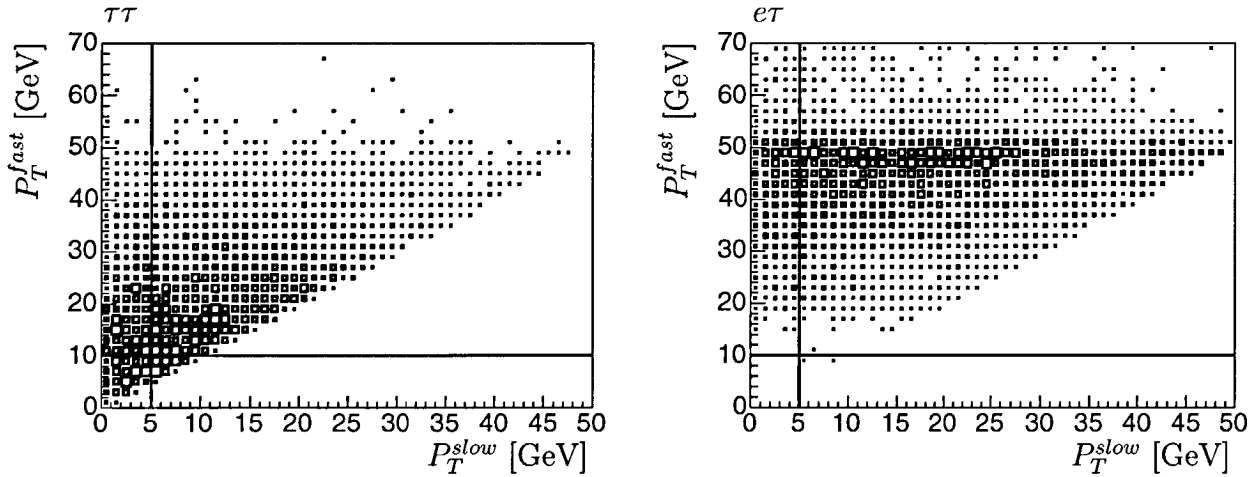


Figure 3.2: P_T of the faster versus P_T of the slower candidate track for a Higgs signal of 100 GeV. The candidates correspond to the charged daughter particles of the τ leptons or to the direct electron in the case of $e\tau$. For $e\tau$ the faster candidate almost always coincides with the direct electron and fulfils $P_T > 10$ GeV easily. The two lines denote the P_T conditions for the candidates. The upper right quadrant is allowed.

The P_T and η distributions of the pseudoscattered⁶ leptons on generator level are shown in Figure 3.3, again for elastically produced Higgs of a mass of 100 GeV. The P_T distributions of the pseudoscattered e^- (left) and τ^- (right) are softer than those for the candidates (see Figure 3.2). The difference between the P_T spectra of the e^- and τ^- are due to their different masses. Setting $m_\tau = m_e$ on generator level results in almost identical spectra. The pseudoscattered leptons tend to go even more in the forward (proton) direction than the Higgs decay products, because unlike the former, the latter can acquire a considerable transverse boost from the Higgs decay. The vertical bar in the η distributions corresponds to the $\theta = 20^\circ$ acceptance cut. Thus, by considering the tracks with highest P_T in the accepted region in θ as candidates, the impurity obtained from pseudoscattered leptons ending up as candidates is expected to be small.

⁶The notion pseudoscattered should indicate that the scattered lepton has undergone a charge inversion and has even changed lepton flavour in case of $e\tau$.

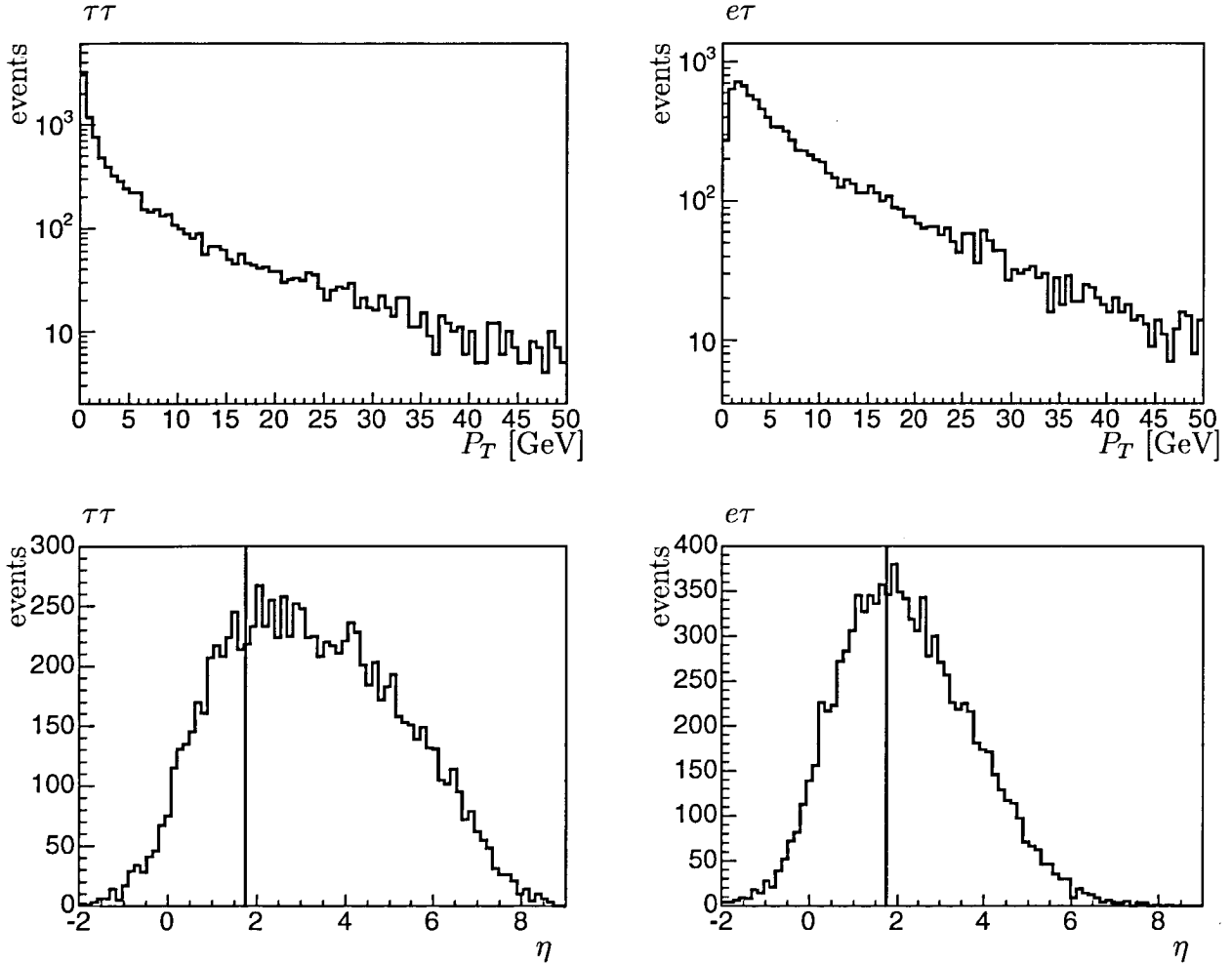


Figure 3.3: Generator level P_T (upper) and η (lower) spectra of the pseudoscalars for $\tau\tau$ (left) and $e\tau$ (right). The vertical bar in the η distributions denotes the forward boundary of the central region, in which the candidates are required to be.

3.3 Back to back Topology

The $\eta\phi$ -distance between two tracks is defined as:

$$R_{\eta\phi} = \sqrt{\Delta\eta^2 + \Delta\phi^2}. \quad (3.3)$$

For particles, which are back to back in ϕ ($\Delta\phi = \pi$) this distance will be $\gtrsim \pi$. Unless the H^{++} itself has a non negligible transverse momentum compared to its mass, the decay particles will have to be back to back in ϕ for reasons of momentum conservation. The $R_{\eta\phi}$ distribution of the candidates in Figure 3.4 shows a clear peak at $R_{\eta\phi} \approx \pi$. It is thus possible to cut on $R_{\eta\phi}$:

Candidate tracks separated: $R_{\eta\phi} > 2.5$

This cut removes background from high energetic jets, which have more than one track of high transverse momentum in a small region of the $\eta\phi$ -space.

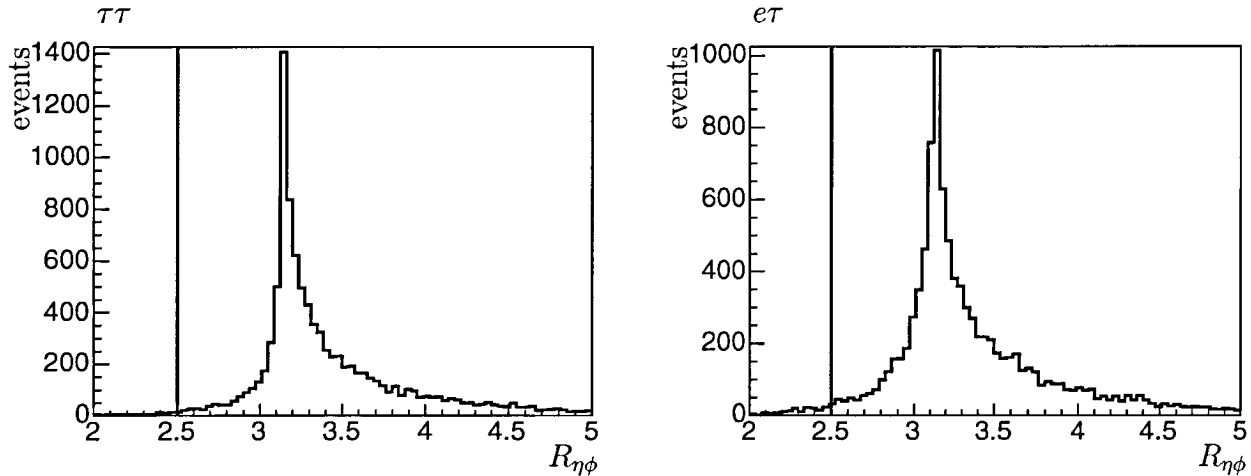


Figure 3.4: Distance in $\eta\phi$ between the two candidates for $\tau\tau$ (left) and $e\tau$ (right). The vertical bar denotes the minimum required $\eta\phi$ -distance.

3.4 Non ep Background Suppression

In order to reduce the non ep physics background a set of offline background finders has been written [45]. These finders aim at detecting events originating from cosmics or from interactions of the proton beam halo⁷ with surrounding material like collimators or the beam pipe, so-called beam-wall interactions. Both of these backgrounds are made up of muons, which are able to penetrate through the external concrete shielding of the experiment because of their minimum ionisation property. The halo muon background is parallel to the proton beam direction.

Figure 3.5 shows the number of signal events, which are rejected for Higgs decays into $\tau\tau$ and $e\tau$ after selection of the candidates. The only background finder, which cuts away more than 1% of the generated signal events is the COSLAR finder in the case of a Higgs decay into $\tau\tau$. It is a cosmic finder based on liquid argon information only. All finders except COSLAR are used.

In order to reject cosmic background an additional requirement on the timing of the CJC can be used. The CJC track reconstruction software provides an event T_0 based on the drift time information for the different tracks with a resolution of about 1 ns. This time stamp is required to be within ± 4.8 ns around a BC as given by the HERA clock. More than 99.9% of the ep events are within this time window. Cosmic background on the other hand is asynchronous to the HERA clock. This cut only applies to data because non- ep physics is not modelled in MC.

⁷The proton beam halo designates protons, which are on stable orbits but outside the beam core.

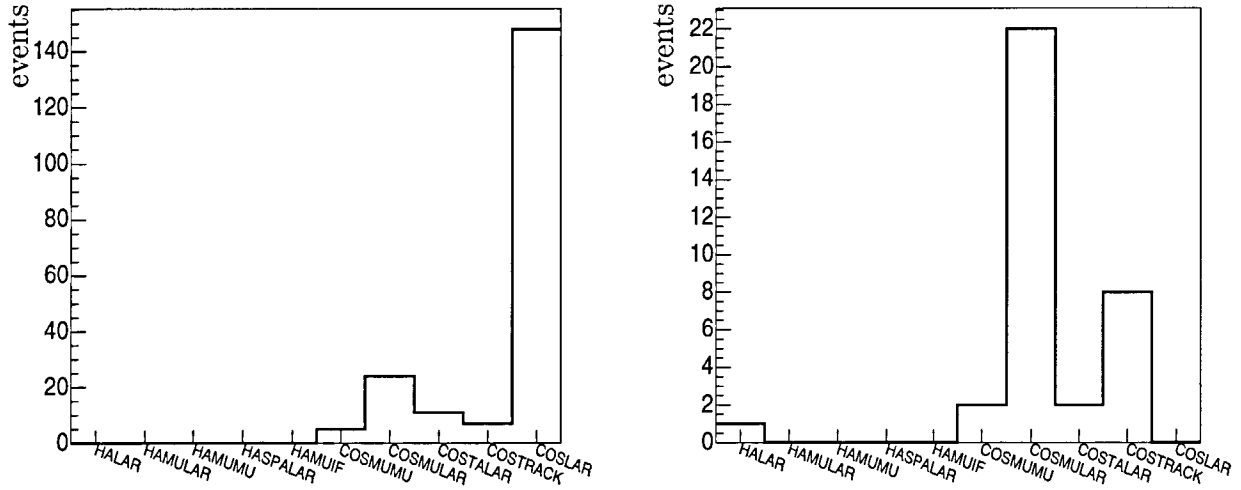


Figure 3.5: Number of signal events rejected by the different background finders in an elastic signal MC sample of 10000 events with Higgs mass 100 GeV for $\tau\tau$ (left) and $e\tau$ (right).

If one of the candidates is a muon (see section 3.5.2) an additional requirement for cosmics suppression is used. The sum of the polar angles (as taken from the candidate's non vertex constrained track) of the candidates is required to differ from 180° by at least 10° :

$$|\sum \theta - 180^\circ| > 10^\circ$$

Basically no signal is lost due to this cut as can be seen from Figure 3.6, where $\sum \theta$ is shown for events for the $\tau\tau$ decay topology and a Higgs mass of 100 GeV. Instead, the signal is boosted into the forward direction.

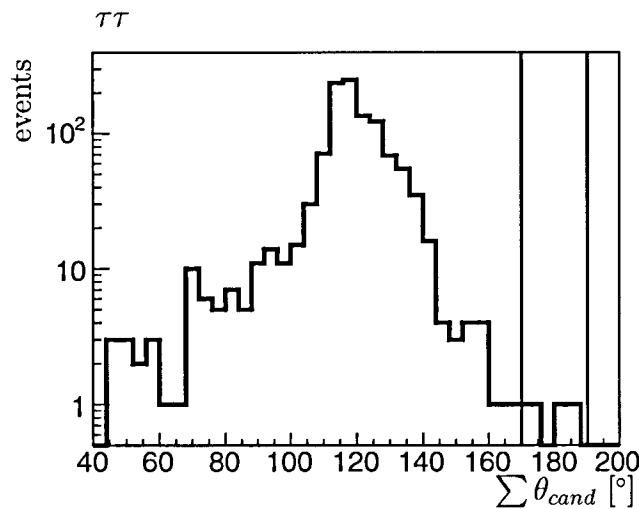


Figure 3.6: $\sum \theta$ of the candidates for a $\tau\tau$ signal MC of a 100 GeV Higgs. The region enclosed by the vertical bars is cut away.

Beam-gas and beam-wall interactions are suppressed by requiring that the z-Vertex of the event should lie within ± 35 cm around the nominal vertex.

| Criteria | Suppressed Background |
|--|---------------------------|
| Background Finders | Cosmics, Beam halo events |
| $ T_0^{CJC} - T_{BC} < 4.8$ ns | Cosmics |
| $ \sum \theta - 180^\circ < 10^\circ$ | Cosmics |
| $ z_{vtx} < 35$ cm | Beam-gas, Beam-wall |

Table 3.2: Summary: non-ep physics suppression

3.5 Event Classification

Different *event classes* are defined according to the decay modes of the τ particles(s) involved in the event. Each event is then classified into exactly one event class. The definition of the different decay classes is imposed from τ decay modes, which can be reliably distinguished. Only electronic, muonic and hadronic decay modes are distinguished. Their relative branching ratios are summarised in Table 3.3.

| τ Decay Mode | BR |
|----------------------|-------|
| $e\nu_e\nu_\tau$ | 17.8% |
| $\mu\nu_\mu\nu_\tau$ | 17.4% |
| $h\nu_\tau\dots$ | 64.8% |

Table 3.3: τ decay modes and branching ratios (BR) from [9]. h stands for a charged hadron.

This leads to the event classes ee , $\mu\mu$, $e\mu$, ej , μj and jj for $\tau\tau$ and the classes ee , $e\mu$ and ej for $e\tau$. j denotes hadronic τ decay i.e. a τ -jet. The branching ratios for these event classes can be easily derived from Table 3.3 and are given in Table 3.4. This event classification will allow to adapt the subsequent selection cuts to the background situation in the individual event classes.

| Event Class | BR $\tau\tau$ | BR $e\tau$ |
|-------------|---------------|------------|
| ee | 3.2% | 17.8% |
| $e\mu$ | 6.2% | 17.4% |
| ej | 23.1% | 64.8% |
| $\mu\mu$ | 3.0% | — |
| μj | 22.6% | — |
| jj | 42.0% | — |

Table 3.4: Branching ratios of the different event classes for $\tau\tau$ and $e\tau$. The $e\tau$ branching ratios are equal to those of a single τ decay (see Table 3.3).

The classification procedure checks for each candidate track if it is linked to an identified electron or an identified muon. The identification procedures for electrons and muons are shortly described below. Each candidate track, which is not explicitly linked to an electron or a muon is at this step regarded as τ -jet. It is explicitly stated here that **no jet finder algorithm is used to identify τ -jets**. For the $\tau\tau$ decay topology the ee and $\mu\mu$ event classes are discarded, because of their small branching ratio and because there is a risk of double counting when combining the results from the $\tau\tau$ analysis with the other dedicated searches for $H^{\pm\pm} \rightarrow ee$ and $H^{\pm\pm} \rightarrow \mu\mu$.

3.5.1 Electron Identification

The H1 electron identification in the LAr calorimeter is based on the criteria formulated in [46]. First calorimeter clusters, which have at least 2 GeV and more than 50% of their energy in the electromagnetic part of the calorimeter are preselected. Then the clusters are merged into an envelope, which is defined by a cone of 7.5 degrees opening angle, starting at a distance of 1 m from the barycentre of the seed cluster. The envelope is truncated after the first hadronic layer of the calorimeter. After this procedure all merged clusters are considered as electron candidates if they fulfil:

- The electromagnetic energy is larger than 5 GeV
- The fraction of electromagnetic energy $E_{em}/E_{tot} > 0.94 + 0.05 \cdot \cos\theta$
- A track is found matching to the cluster within a cone of $R_{\eta\phi} < 0.1$ [47]. For the ee event class the starting radius (first hit in the CJC) of the electron track is required to be smaller than 30 cm. This cut reduces late photoconversion from Compton background in ee .
- The energy in a cone of $R_{\eta\phi} < 0.5$ around the electron candidate (not counting the electron energy) is less than 5% of the electron energy [47]. This means that the electron has to be isolated in the calorimeter.

3.5.2 Muon Identification

Several muon identification procedures are in use at H1 [48, 49]. Most procedures make use of the instrumented iron (s. section 2.2.3), which most high P_T muons reach because of their minimum ionisation property. The combination of hits in different layers of the instrumented iron (s. section 2.2.3) yields so-called *iron tracks* [50], defined by the impact point in the iron and a direction. Each iron track must meet a set of quality criteria, which can be found in [51].

In this analysis no explicit link between an iron track and a track of the central tracker is required but each iron track is required to match a central track within a distance of $R_{\eta\phi} < 0.5$.

Muon identification efficiencies and misidentification probabilities for hadrons are given in [51]. For muons with $P_T > 5$ GeV, the identification efficiency is $\geq 90\%$ and the probability to wrongly identify hadrons (pions, kaons) as muons is below 2%.

Another muon identification procedure relies on the LAr calorimeter and the central tracker alone. This procedure is also described in detail in [49]. A central track for a muon candidate is extrapolated into the calorimeter where the deposited energy inside and outside of cylinders of radius 15 cm and 30 cm around the track are determined. These quantities are used to define a muon quality criteria, which is a number between 0 and 3. Candidates, which have a quality of 3 (“good muons”), are also regarded as muons in this analysis. The efficiency for the LAr based muon identification is about 70% for muons with momentum ≥ 3 GeV and the misidentification probability (pion identified as muon) for quality 3 muons is below 2%.

3.6 Trigger

In order to determine the efficiency, by which doubly charged Higgs signal events in the acceptance region are triggered by the H1 detector, a subset of L1 subtriggers has to be chosen and their combined efficiency determined. For data it will be required that at least one of the subtriggers has fired⁸ and for MC the trigger efficiencies will be applied.

The subtriggers used in this analysis are given in Table 3.5. The main trigger elements, as explained in section 2.2.4, for each subtrigger are given as well as the mean (lumiweighted) L1 prescale factors and the L2 condition for subtrigger ST71. For each subtrigger a set of non ep physics veto conditions, the so-called *global options* are applied. Examples and definitions for such global options can be found elsewhere [52].

| ST Nr. | Main trigger elements | Mean L1 prescale | L2 condition |
|--------|----------------------------------|------------------|---------------|
| ST18 | Mu_ECQ && DCRPh_Ta && DCRPh_THig | 1.33 | — |
| ST34 | Mu_Bar && DCRPh_Ta && DCRPh_THig | 1.18 | — |
| ST66 | LAr_IF>1 && LAr_Etmiss>2 | 1.00 | — |
| ST67 | LAr_electron>1 | 1.00 | — |
| ST71 | LAr_BR && DCRPh_Tc | 1.04 | LAr-BigT-miss |
| ST77 | LAr_Etmiss>1 | 1.00 | — |

Table 3.5: *Subtriggers used in the analysis and their mean (lumiweighted) L1 prescale factors. The notation “&&” denotes logical AND operation of two trigger elements.*

3.6.1 Trigger Efficiencies

For all event classes containing electrons the most important subtrigger is ST67, which is exactly supposed to trigger electrons in the LAr calorimeter and which is also unprecaled (see Table 3.5). Its efficiency was determined to be close to 100% in [52] for electrons with energies $\gtrsim 10$ GeV. The electron energy for events in $e\mu$ and ej classes for the $\tau\tau$ decay channel is shown in figure 3.7 for a 100 GeV elastically produced Higgs signal.

⁸I.e. all selected subtriggers are combined in a logical OR.

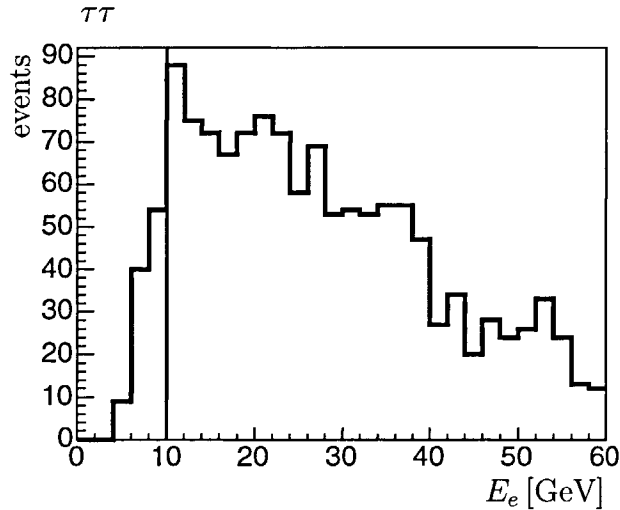


Figure 3.7: Electron energy for event classes $e\mu$ and ej for the $\tau\tau$ decay channel. The Higgs mass is at 100 GeV. To the right of the vertical line at 10 GeV the trigger efficiency is approximately 100%.

For electron energies below 10 GeV the trigger efficiency was shown in [52] to drop steeply with decreasing energy. Therefore, the following requirement is imposed:

$$\text{Electron energy} \geq 10 \text{ GeV.}$$

At this level of the preselection 7% of the remaining signal in $e\mu$ and ej are lost due to this requirement for a Higgs mass of 100 GeV. For the $e\tau$ decay channel the losses are much smaller, because in this case the electron energy is much harder. No efficiency correction is applied to surviving events in electron classes, but a systematic uncertainty of 0.5% is assigned to these events [52].

For the $\tau\tau$ decay channel there are two non-electron event classes, namely μj and jj , which are treated separately.

μj trigger efficiency

Because there is only a small amount of μj events in data, the trigger efficiency can not be determined from data directly. Instead it is argued here, that the signature of this event topology in the LAr calorimeter is a signature of missing transverse energy. The muon, because of its minimum ionisation property, deposits only a small amount of energy (typically a few GeV) in the calorimeter, while the jet in the opposite hemisphere will usually be completely absorbed. The LAr signature is thus roughly the same as that for charged current events. The LAr triggers used here,

$$\text{ST66} \ || \ \text{ST67} \ || \ \text{ST71} \ || \ \text{ST77}^9,$$

⁹“||” denotes logical OR.

are H1 standard triggers for charged current analyses [40, 52]. The most important sub-trigger is ST77, which triggers missing transverse energy. The combined trigger efficiency is determined by *pseudo-charged current* events [53]. These are neutral current events, where the scattered electron was removed in order to obtain a high statistics data sample, which closely resembles the charged current topology. With this data sample the trigger efficiency of the above triggers was determined e.g. in [51] as a function of the scattering angle γ^{hfs} and the transverse momentum P_T^{hfs} of the hadronic final state¹⁰. These quantities are shown for the μj class for a 100 GeV Higgs in figure 3.8. Unlike NC or CC jets, high energetic τ -jets are usually contained in a single trigger tower. Therefore, the pseudocharged current trigger efficiency as determined above is a conservative estimate of the true trigger efficiency.

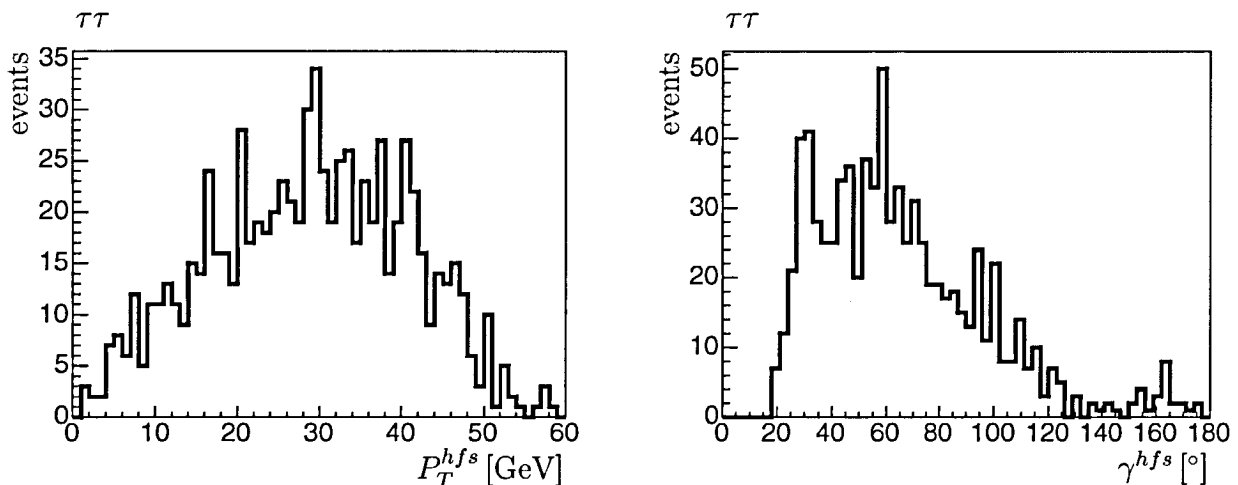


Figure 3.8: P_T^{hfs} (left) and γ^{hfs} (right) for the μj class for a 100 GeV Higgs.

The LAr triggers are complemented with the muon triggers ST18 and ST34. These triggers were studied in [54], where it was shown that their efficiencies are correctly described in the trigger simulation for MC. Muon trigger efficiencies are therefore taken directly from the MC. L1 Trigger prescales as well as the L2 condition for ST71 are taken into account as described in [55]. Each event is then assigned a combined trigger efficiency ε_{comb} :

$$\varepsilon_{comb} = 1 - (1 - \varepsilon_{PsCC}) \cdot (1 - \varepsilon_{\mu}). \quad (3.4)$$

Here ε_{PsCC} is the efficiency for the LAr triggers (see above) determined from pseudo-charged current data and ε_{μ} is the prescale corrected efficiency of the muon triggers (ST18, ST34). ε_{comb} can then be regarded as probability to trigger the considered event. The efficiency distribution for the signal MC sample for a Higgs of 100 GeV (see Figure 3.9) yields a mean efficiency of 0.95.

***jj* trigger efficiency**

For the jj channel the trigger efficiency is determined from a neutral current data sample

¹⁰The hadronic final state is the momentum 4-vector containing all hadrons and jets of an event.

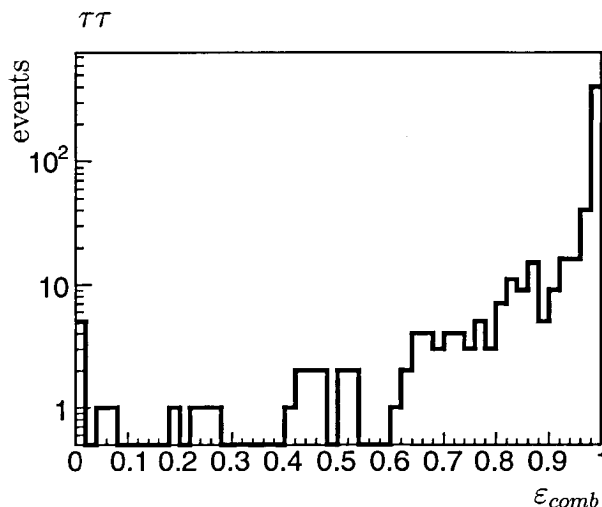


Figure 3.9: The signal efficiency of single events distribution for the μj event class for a Higgs signal of 100 GeV.

where the scattered electron is detected in the SPACAL calorimeter. The subtrigger ST9 serves as monitor trigger.

| ST Nr. | Main trigger elements | Mean L1 prescale | L2 condition |
|--------|-----------------------|------------------|--------------|
| ST9 | SPCLe_IET>1 | 2.23 | SPCL_R30 |

The preselection of jj events is run exactly as for the final analysis with the following changes:

- Events with electrons in the SPACAL are not rejected.
- Events with electrons in the LAr calorimeter are rejected.

The efficiency is then determined as:

$$\varepsilon = \frac{\text{\#events triggered by analysis \&\& monitor triggers}}{\text{\#events triggered by monitor trigger}}. \quad (3.5)$$

This efficiency is displayed in Figure 3.10 as a function of the P_T cut on the higher P_T candidate. P_T of the lower P_T candidate is required to be more than 5 GeV as in the analysis preselection. The hatched regions are the corresponding efficiencies and error bands obtained from the MC trigger simulation for a neutral current MC with $1 < Q^2 < 150 \text{ GeV}^2$. The efficiency errors in Figure 3.10 are calculated according to the formula [53]:

$$\delta\varepsilon = \max \left(\sqrt{\frac{\varepsilon(1-\varepsilon)}{N_0}}, \frac{1}{N_0} \right), \quad (3.6)$$

where N_0 is the total number of events in the considered bin. For the operating point of this analysis ($P_T^1 \geq 10 \text{ GeV}$) the trigger simulation is describing the data within the errors. Thus, for the jj event class the trigger simulation is used in all MC samples and a systematic error of 5% is assigned to the trigger efficiency.

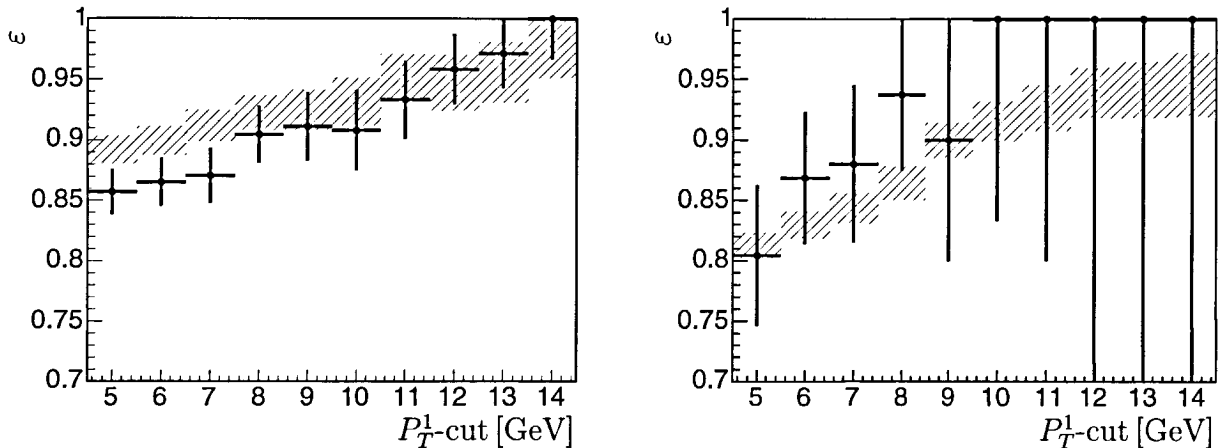


Figure 3.10: The signal efficiency distribution for the jj event class as determined from the ST9 monitor trigger sample as a function of the P_T cut on the faster candidate. The left (right) plot shows the efficiency for the 99/00 (96/97) dataset. The large efficiency errors in 96/97 are due to low statistics.

3.7 Data - MC comparison

3.7.1 The Background MC

The set of background MC samples used to compare to the data obtained after the preselection is composed of the samples summarised in Table 3.6. Neutral current processes for different regions in Q^2 and the di-lepton productions ee , $\mu\mu$ and $\tau\tau$ from SM processes are considered. The contribution from charged current was found to be negligible (about 1 event in the jj event class after preselection). All background MC samples were produced for both datasets separately.

- **Photoproduction (γp , $Q^2 < 1 \text{ GeV}^2$)**

For $Q^2 < 1 \text{ GeV}^2$ a PYTHIA61 [56] MC sample is used. The sample consists of direct and resolved contributions from uds, c and b quarks. In order to keep the number of events in the sample small a generator level cut on $\hat{p}_T > 10 \text{ GeV}$ is imposed. \hat{p}_T is the transverse momentum of the incoming particles of the hard subprocess. The \hat{p}_T distribution after preselection for a γp -sample without the generator level cut can be seen in Figure 3.11. The luminosity as calculated from PYTHIA61 is divided by a global factor of 1.2 as was determined in [57].

- **Low Q^2 ($1 < Q^2 < 100 \text{ GeV}^2$)**

For $1 < Q^2 < 100 \text{ GeV}^2$ a RAPGAP28 [58] MC with DIS scattering is used. The background for this kinematical region is expected to be small because most events produce a scattered electron in the SPACAL acceptance, with the effect that these events are almost completely rejected on preselection level already.

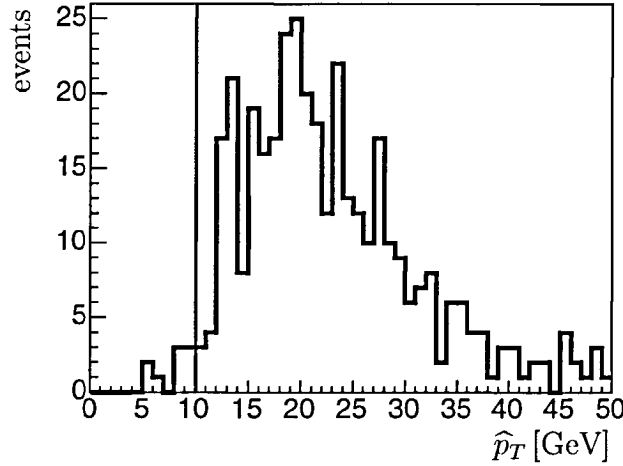


Figure 3.11: \hat{p}_T distribution after preselection for a PYTHIA61 MC sample without the constraint on \hat{p}_T . The vertical line denotes the generator level cut.

- **High Q^2 ($Q^2 > 100 \text{ GeV}^2$)**

For $Q^2 > 100 \text{ GeV}^2$ the DJANGO13 [59] MC generator is used. Contributions from heavy quarks are included. QCD parton dynamics are modelled by the colour dipole model (CDM) [60].

- **Di- $e/\mu/\tau$ production**

The GRAPE MC generator [61] is used for the simulation of di-lepton final states. All electroweak processes are included. A minimal transverse momentum for both leptons of $P_T > 4 \text{ GeV}$ and a minimal invariant mass $M > 4 \text{ GeV}$ are required. All three samples (ee , $\mu\mu$ and $\tau\tau$) were produced separately for the elastic, quasielastic and inelastic régimes, which means $Q^2 = 0 \text{ GeV}^2$, $0 \leq Q^2 \leq 1 \text{ GeV}^2$ and $Q^2 > 1 \text{ GeV}^2$ at the proton vertex respectively.

| Background | Generator | $\mathcal{L} [\text{pb}^{-1}]$ | Main cuts |
|---------------|-----------|--------------------------------|--|
| γp | PYTHIA61 | 83.3 | $0 < Q^2 < 1 \text{ GeV}^2, \hat{p}_T > 10 \text{ GeV}$ |
| NC Low Q^2 | RAPGAP28 | 174 | $1 < Q^2 < 100 \text{ GeV}^2$ |
| NC High Q^2 | DJANGO13 | 520 | $Q^2 > 100 \text{ GeV}^2$ |
| SM ee | GRAPE | 1712 | $M_{ee} > 4 \text{ GeV}, P_T^e > 4 \text{ GeV}$ |
| SM $\mu\mu$ | GRAPE | 1990 | $M_{\mu\mu} > 4 \text{ GeV}, P_T^\mu > 4 \text{ GeV}$ |
| SM $\tau\tau$ | GRAPE | 2282 | $M_{\tau\tau} > 4 \text{ GeV}, P_T^\tau > 4 \text{ GeV}$ |

Table 3.6: Set of background MC samples for comparison with the 99/00 data set. For the 96/97 data set a similar set of MC samples was used but with slightly different luminosities. See the text for a more detailed description.

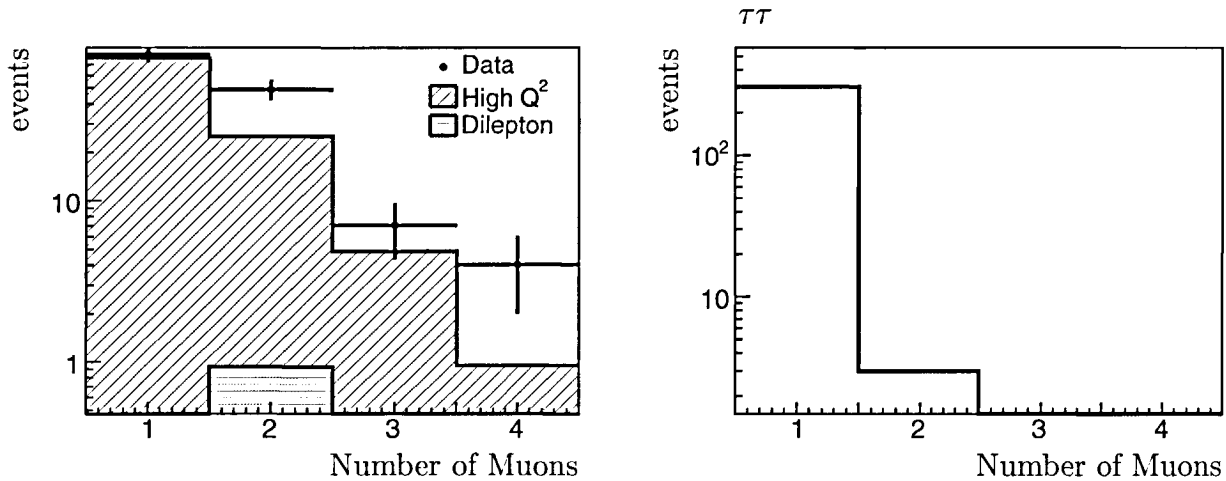


Figure 3.12: Number of Muons for data and background MC (left) and for a $\tau\tau$ -Higgs signal of 100 GeV (right). The discrepancy between data and background MC results from events with more than one muon.

3.7.2 Data - MC discrepancies

At this stage, the set of MC samples presented in the previous section is compared to the data. Control distributions yield a good agreement between data and MC in general. The remaining discrepancies are discussed in the following sections.

3.7.2.1 $e\mu$ Event Class

In the $e\mu$ event class at the current stage of the selection the number of surviving events are:

| Dataset | Data | \sum MC |
|---------|------|-----------|
| 99/00 | 141 | 108 |
| 96/97 | 52 | 46 |

The discrepancy, mainly seen in the 99/00 dataset, comes from events with more than one muon, as can be seen in figure 3.12. It could be due to several reasons. For instance remaining Cosmics or an insufficient/absent modelling of multi-muon final states (e.g. originating from vector mesons) in the MC could cause such a behaviour. The reason is of no interest for this analysis, instead it is required that

there must be exactly one identified muon in the $e\mu$ event class.

The right side of Figure 3.12 shows the number of identified muons in a signal sample for a 100 GeV Higgs decaying into $\tau\tau$. Only 1% of the events, which are selected in the $e\mu$ event class, have more than 1 muon. These are events where both τ 's have decayed into muons, but accidentally the scattered electron is taken as τ candidate.

3.7.2.2 Forward Region

Another disagreement between data and MC is observed in the ej event class at this stage of the selection for τ -jets at polar angles $\theta < 50^\circ$ (see Figure 3.13). For small polar angles the MC clearly overshoots the data.

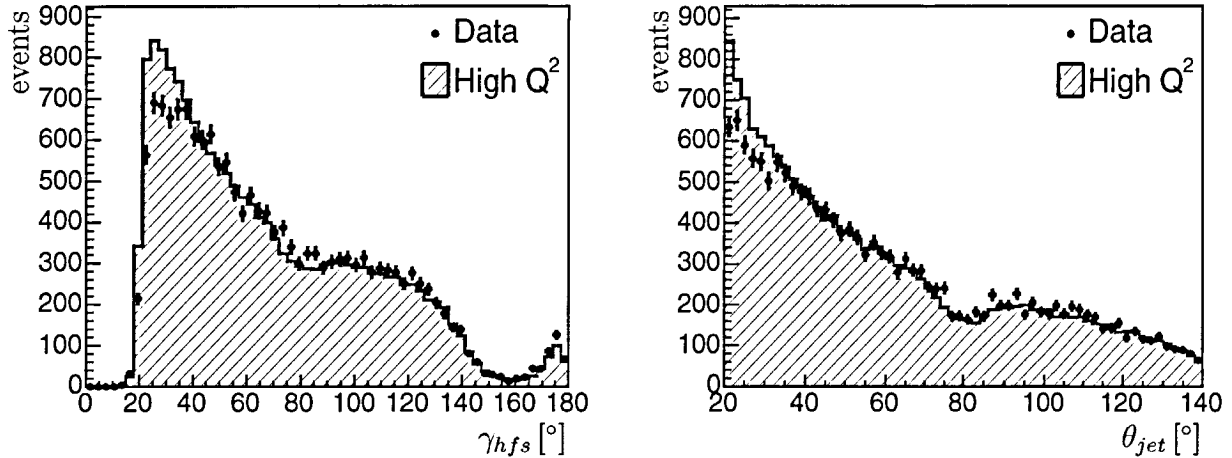


Figure 3.13: Scattering angle γ_{hfs} of the hadronic final state (left) and θ of the jet (right) for the ej event class in the 99/00 dataset. The discrepancy for angles $< 50^\circ$ is manifest.

Several types of tracks are reconstructed at H1: central, forward and combined tracks. Central (forward) tracks are based on information of the central (forward) tracker alone (see Figure 2.3). Combined tracks on the other hand use hits from the central and the forward tracker. The θ acceptance cut ($\theta > 20^\circ$) requires the candidates to pass through the CJC1 and therefore most of the tracks even in the region $20 < \theta < 50^\circ$ are of type central. This is illustrated for the 99/00 dataset in Figure 3.14. Forward tracks are badly modelled in the MC and are therefore rejected. However, the main discrepancy comes from central tracks (see Figure 3.13, right).

Several possible causes for the bad description of the forward region were investigated (e.g. dead material correction in the simulation, vertex smearing, MC fragmentation scheme, etc.). The only quantity found to have an impact on the forward region alone was the isolation of the τ -jet candidate. In section 4.2 the τ -jet candidates are required to be isolated in the sense that no additional track is allowed in a cone in the $\eta\phi$ -space between $0.15 < R_{\eta\phi} < 1.5$. The inner boundary (0.15) of this cut is chosen such as to allow for high energetic (narrow) 3-prong τ -jets. As is shown in section 4.2 the cut is very efficient in removing non signal-like jets, but for reasons of data-MC comparisons the number of surviving events in the preselection should not be too small. Therefore, only a soft version of this cut is introduced here:

Not more than 3 tracks in $0.15 < R_{\eta\phi} < 1.5$ around a τ -jet candidate allowed.

Figure 3.15 shows the scattering angle of the hadronic final state and the jet for the ej event class after this isolation cut on τ -jets for the 99/00 dataset. The forward region

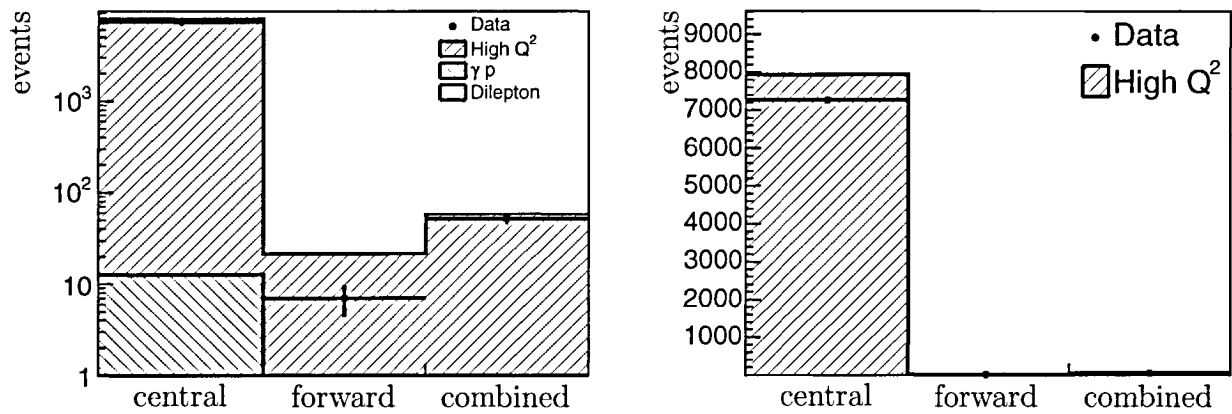


Figure 3.14: Track types for the jet candidate in the ej event class for $\theta_{jet} < 50^\circ$ in logarithmic (left) and linear (right) scale.

is clearly better described compared to Figure 3.13. In the 96/97 dataset on the other hand, in the region $25 \lesssim \theta_{jet} \lesssim 50^\circ$ a discrepancy is still apparent. Its cause is however not known.

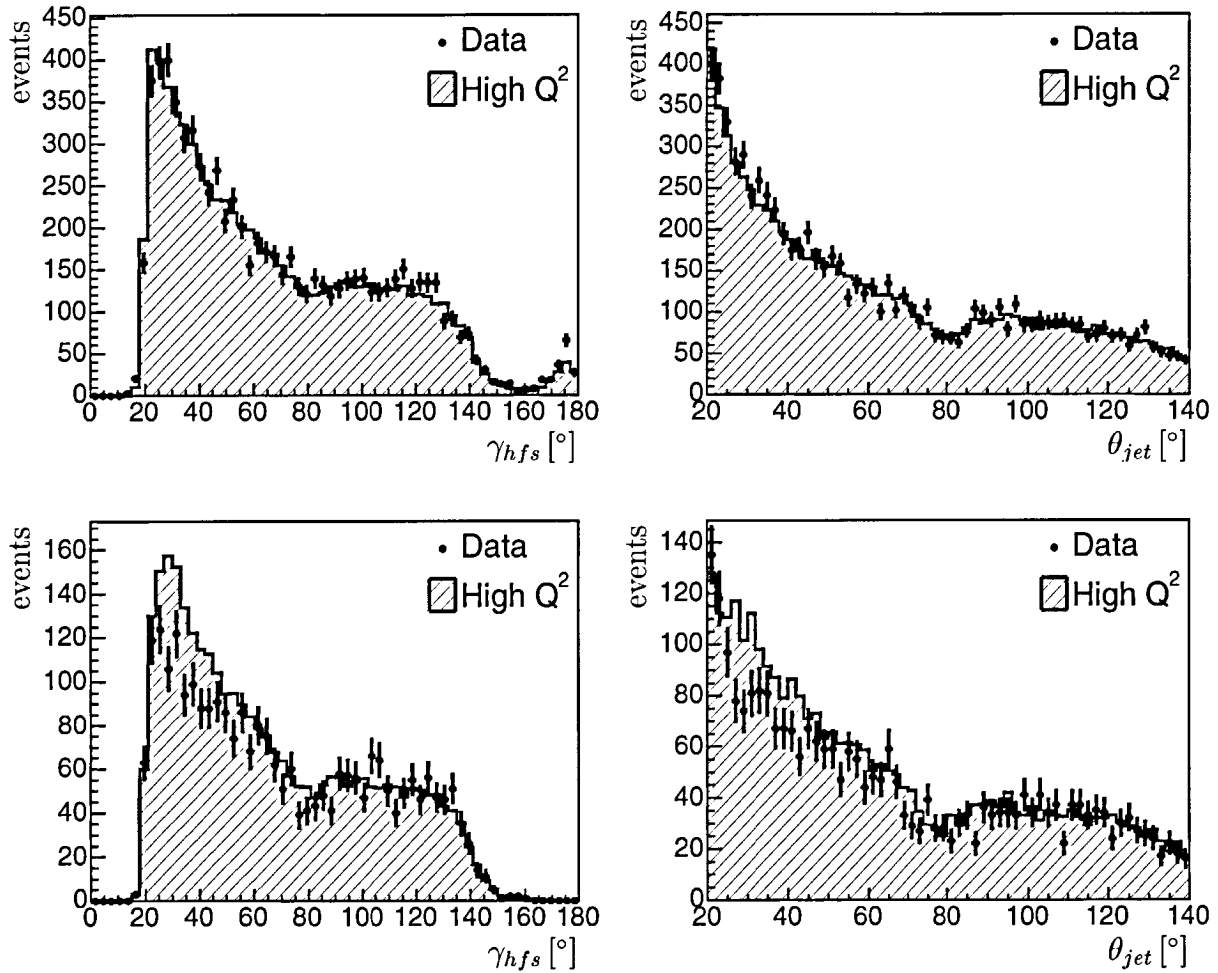


Figure 3.15: Scattering angle γ_{hfs} of the hadronic final state (left) and θ of the jet (right) for the ej event class after the soft isolation cut. The description of the forward region for 99/00 (upper plots) has clearly improved w.r.t. Figure 3.13. For the 96/97 (lower plots) dataset the forward region is still problematic.

3.7.3 τ -Jet refinement

At this stage all candidates, which are not tagged as electrons or muons are candidates for τ -jets. Unidentified muons and electrons will therefore contaminate the jet class. In order to get rid of unidentified muons, a simple cut on the ratio of the transverse energy measured in the calorimeter to the transverse momentum of the track can be applied. Unlike jets, muons deposit only a small fraction of their energy in the calorimeter. In Figure 3.16 the ratio E_T/P_T is shown for muons in the GRAPE MC. The transverse energy E_T is the uncalibrated transverse energy, which is linked to the candidate.

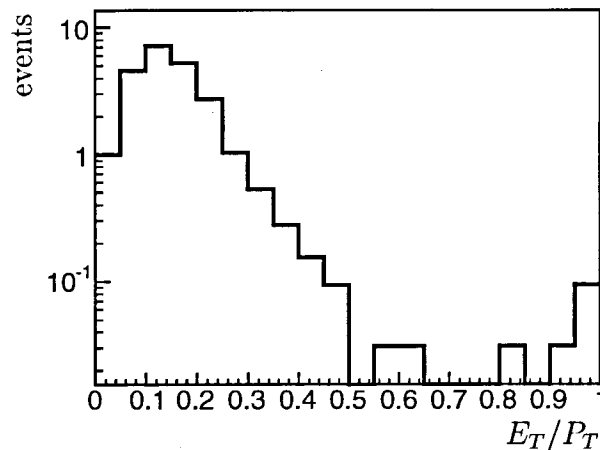


Figure 3.16: Ratio of transverse energy over transverse momentum for muons in the MC.

For τ -jet candidates it is therefore required that:

$$E_T^{jet} > 0.4 \cdot P_T^{track}.$$

Only a small amount of events is rejected by this cut in data and MC as can be seen in Figure 3.17 for the 99/00 dataset. The normalisation mismatch in the jj event class (right plot) is discussed later.

3.7.4 Control Distributions

The number of surviving events after preselection is summarised in Table 3.7. The largest discrepancies between data and MC are found in the jj class (about 4σ) for 99/00 and in the ej class (about 6σ) for 96/97. The latter discrepancy is due to a still badly described forward region in the DJANGO MC for 96/97 despite the isolation cut described in section 3.7.2.2. All discrepancies are substantially reduced by subsequent selection cuts.

In the following, a set of control distributions is shown for ej and jj event classes. Unfortunately the other event classes suffer from low statistics after preselection already.

In Figure 3.18 the number of surviving events after preselection for the different event classes can be seen. Contributions from different background MC samples are also displayed. As expected, the largest background after the preselection is found in the ej event

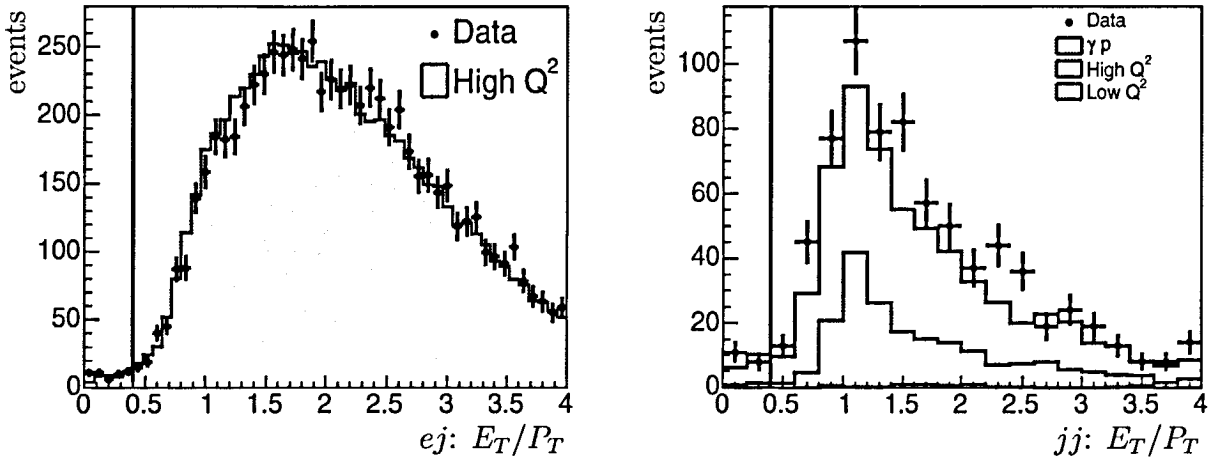


Figure 3.17: E_T/P_T for jet candidates in data and MC for the 99/00 dataset for the ej class (left) and jj class (right). The vertical bar denotes the cut position.

| Dataset | $e\mu$ | | ej | | μj | | jj | | ee | |
|---------|--------|----|------|------|---------|-----|------|-----|------|----|
| | Data | MC | Data | MC | Data | MC | Data | MC | Data | MC |
| 99/00 | 43 | 41 | 7467 | 7461 | 7 | 5.6 | 380 | 304 | 61 | 76 |
| 96/97 | 14 | 16 | 2716 | 3042 | 5 | 2.6 | 148 | 131 | 34 | 34 |

Table 3.7: Number of surviving events after preselection for different event classes and for both datasets.

class. It originates from high Q^2 NC. Di-lepton production plays only a minor role at this stage of the selection. In the jj event class photoproduction ($Q^2 \approx 0$) is dominant.

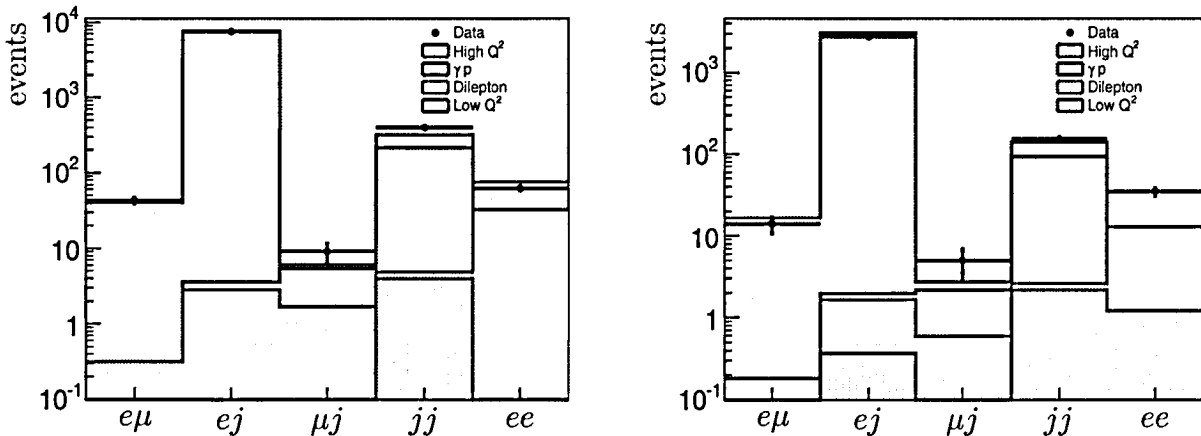


Figure 3.18: Number of surviving events after preselection for the different event classes for 99/00 (left) and 96/97 (right).

The missing transverse momentum P_T^{Miss} for the ej and jj event classes is shown in

Figure 3.19. The normalisation mismatches in the jj class (99/00) is evident. But the shapes of the distributions are described.

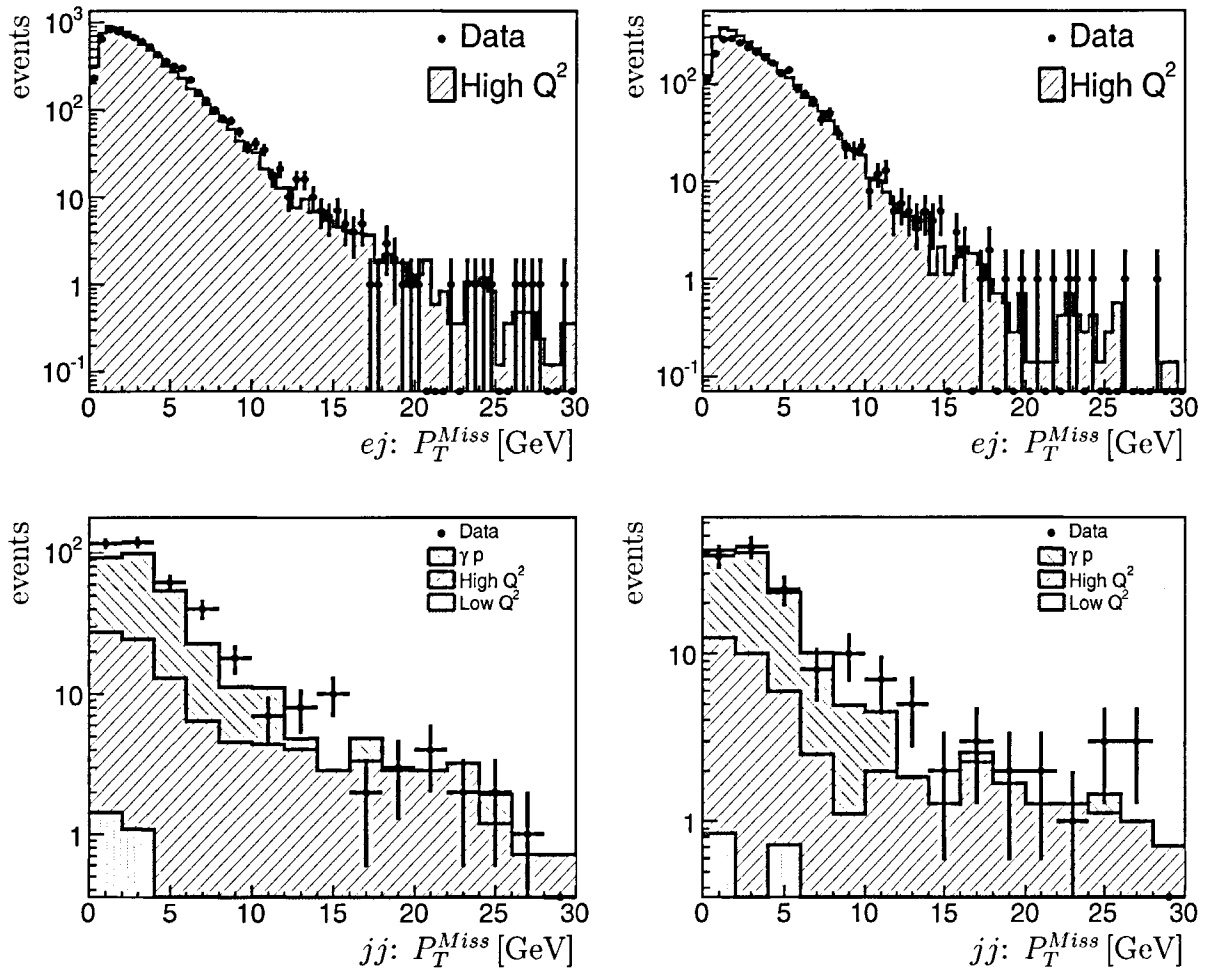


Figure 3.19: P_T^{Miss} distributions for the ej (upper) and jj (lower) event classes. Plots on the left (right) are done for 99/00 (96/97). The normalisation mismatch in jj for 99/00 (lower left) can be clearly seen.

Chapter 4

Final Selection

4.1 Rejection of NC Events

The longitudinal momentum balance of an event is conveniently described with the $E - p_z$ variable, which is just the sum over all particles in an event of their energy minus their momentum in z-direction:

$$E - p_z = \sum_{particles} (E_i - p_{z,i}). \quad (4.1)$$

Momentum balance demands that this sum is equal to that of the initial state, which is twice the incoming electron energy, i.e. $E - p_z = 2E_e = 55 \text{ GeV}$ ¹. In an event where all produced particles (except for those escaping in the proton beam direction) are within the detector acceptance, one expects to measure $E - p_z \approx 55 \text{ GeV}$. Any significant deviation from that value indicates that some particles have left the detector unobserved. This can happen e.g. for the scattered electron in photoproduction events or for neutrinos e.g. originating from τ decays.

4.1.1 $\tau\tau$ Topology

In the case of $H^{\pm\pm} \rightarrow \tau\tau$ with 2 τ leptons produced mainly in the central region (see Figure 3.1), a significantly reduced $E - p_z$ is expected. In Figure 4.1 the $E - p_z$ distributions are shown for the ej and jj classes for both datasets and for a Higgs signal of mass 100 GeV. The peak at $E - p_z = 55 \text{ GeV}$ can be seen in data and background, while for the signal $E - p_z$ is shifted towards smaller values. The cut is chosen at 45 GeV (vertical lines):

$$E - p_z < 45 \text{ GeV}.$$

The deeply inelastic NC background in the jj class is mainly due to unidentified electrons, which end up as τ -jets in this analysis (see section 3.7.3).

¹The incoming proton has $E - p_z = 0 \text{ GeV}$ because it moves along the positive z-direction.

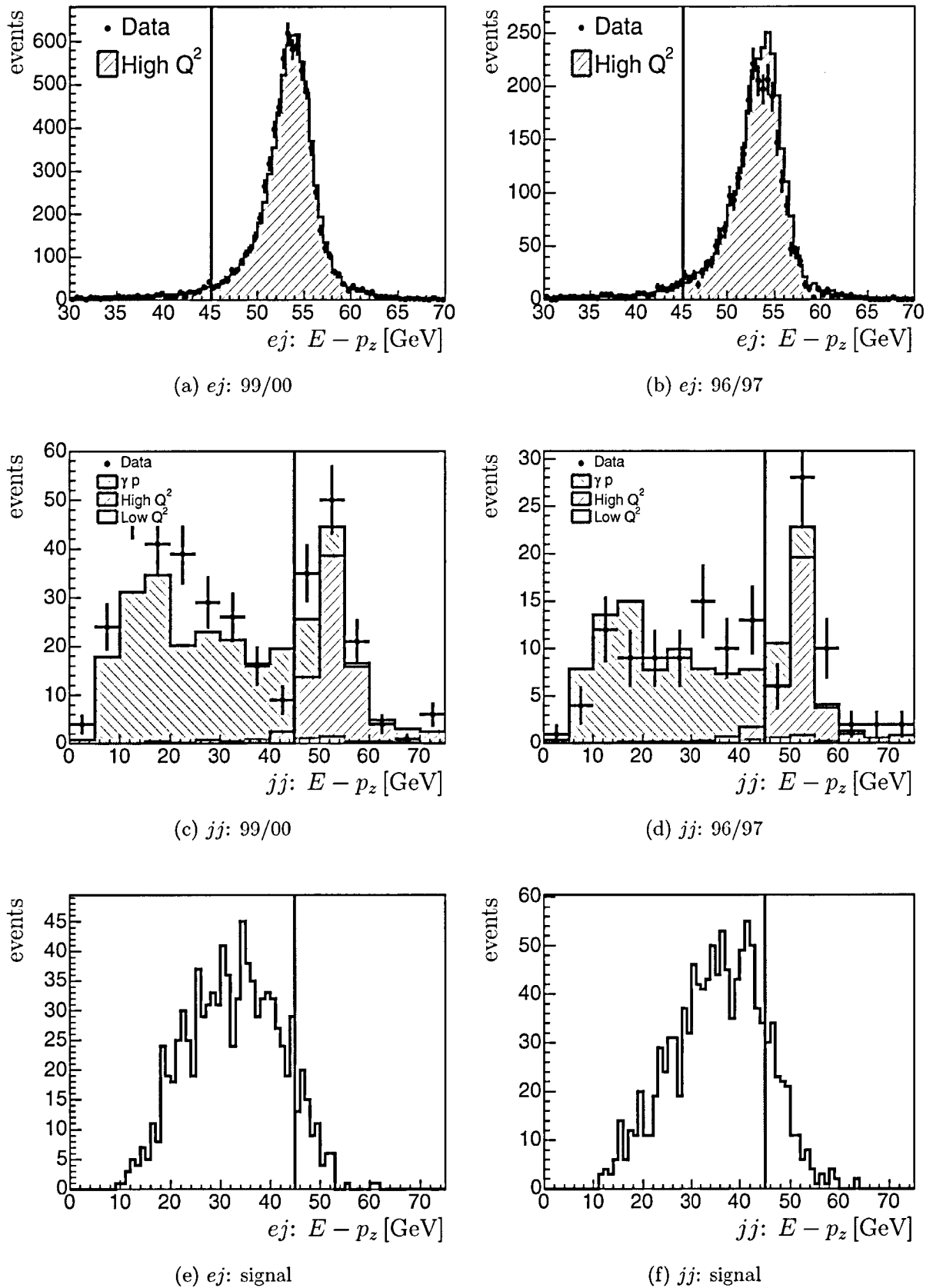


Figure 4.1: $E - p_z$ distributions for the ej and jj event classes for data and background, as well as for a signal MC of a 100 GeV Higgs. The normalisation mismatch in jj for 99/00 and ej for 96/97 can be clearly seen. The vertical line denotes the cut position.

The transverse momentum balance of the ej event class is shown in Figure 4.2 (before the $E - p_z$ cut) for the 99/00 dataset. The background could be removed in an equally efficient way e.g. by imposing $P_T^{Miss} > 10$ GeV but this would also lead to a dramatic loss in the signal. It seems that the missing transverse momentum of the two τ leptons in the signal is often balanced. Thus, no condition is imposed on P_T^{Miss} for $\tau\tau$.

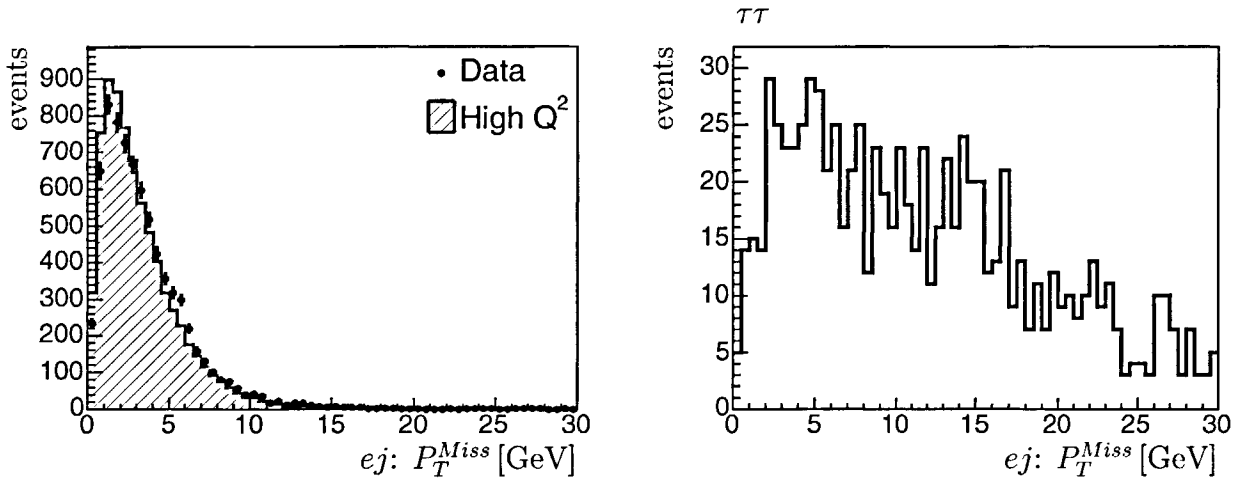


Figure 4.2: P_T^{Miss} distributions for the ej event class for data, background and a $\tau\tau$ signal MC of a 100 GeV Higgs.

4.1.2 $e\tau$ Topology

For $H^{\pm\pm} \rightarrow e\tau$ there are again two τ leptons in the final state but one of them corresponds to the pseudoscattered lepton, which has its momentum favoured parallel to the proton (see Figure 3.3). Missing energy from the decay of this latter τ has therefore only a small contribution to P_T^{Miss} and to missing $E - p_z$. This can be seen in Figure 4.3. The missing P_T of the two τ leptons is less balanced resulting in a harder P_T^{Miss} spectrum w.r.t. Figure 4.2, on the other hand the $E - p_z$ spectrum loses much of its discriminative power w.r.t. Figure 4.1.

Finding an optimised cut on these two quantities would require to run the analysis for many different cut settings, including all subsequent analysis cuts and then calculate the expected limit² on the Higgs production cross section for each cut setting. However, this procedure has the serious disadvantage to be very time consuming. Therefore, a different approach is chosen here:

1. All data and MC samples are processed once with all cuts (as described later on) except for the cut on jet isolation (see section 4.2) and the cut on $E - p_z$ and P_T^{Miss} . The jet isolation cut was found to be uncorrelated to $E - p_z$ and P_T^{Miss} and is only

²The subsequent cuts and the term “expected limit” are explained in later sections of this thesis. It is the inherent problem at this stage that for optimising one cut, all other cuts have to be applied in order to take correlations between cuts into account.

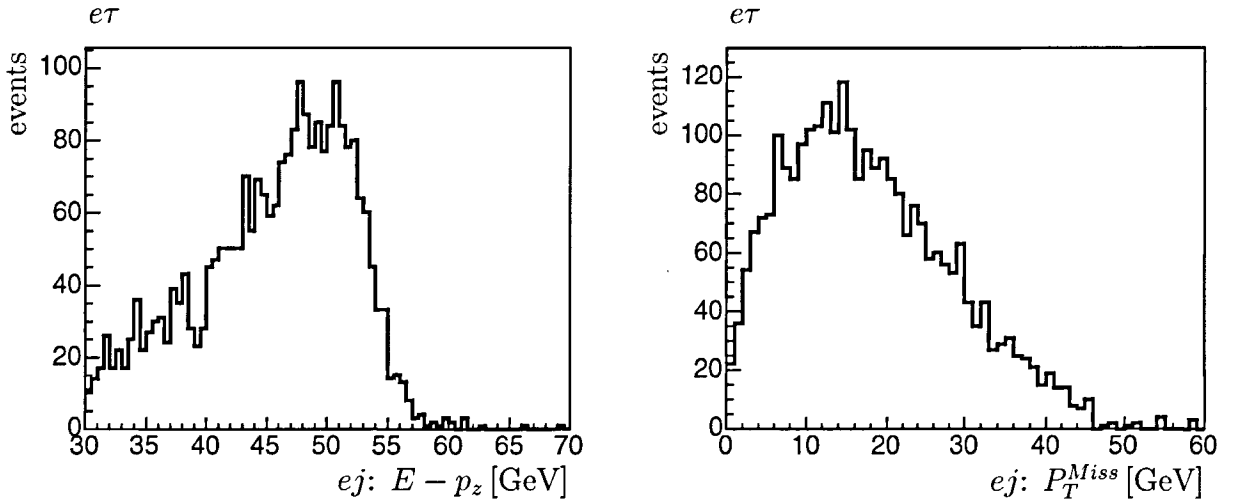


Figure 4.3: $E - p_z$ (left) and P_T^{Miss} (right) distributions for the ej event class for a signal MC of a 100 GeV Higgs.

dropped here in order to have a higher statistics background sample for the cut optimisation.

2. The following cut variants are tested:

- $P_T^{Miss} > X$
- $E - p_z < Y$
- $P_T^{Miss} > X$ OR $E - p_z < Y$
- $P_T^{Miss} > X$ AND $E - p_z < Y$

with the cut ranges $0 < X < 25$ GeV and $40 < Y < 59$ GeV. For each cut variant the signal efficiency ε and the background expectation B in the ej event class are determined.

3. The maximal value of the following estimator [62] is used as a guidance for the optimal cut:

$$\frac{\varepsilon}{a/2 + \sqrt{B}}. \quad (4.2)$$

The number a is the number of (Gaussian) standard deviations one would require a signal to differ from the SM prediction before the SM hypothesis is rejected. Common practice is to use $a = 5$, although there is a certain arbitrariness in this choice. Note, that other commonly used estimators such as S/\sqrt{B} or $S/\sqrt{S+B}$, with S the number of surviving signal events, tend to fail for analyses, which end up with low background expectations of the order of a few events. The estimator from (4.2) on the other hand is also useable for low statistics analyses.

In Table 4.1 the best cuts according to estimator (4.2) are given for a Higgs mass of 100 GeV. The logical AND combination of the P_T^{Miss} and $E - p_z$ cut produces the highest estimator value. Therefore, only this latter cut variant is considered further.

| Cut | X [GeV] | Y [GeV] | Estimator Maximum |
|------------------------------------|---------|---------|-------------------|
| $P_T^{Miss} > X$ | 17.6 | – | 169.0 |
| $E - p_z < Y$ | – | 48.8 | 121.0 |
| $P_T^{Miss} > X$ OR $E - p_z < Y$ | 11.4 | 40.0 | 132.9 |
| $P_T^{Miss} > X$ AND $E - p_z < Y$ | 14.0 | 47.6 | 237.4 |

Table 4.1: Best cut settings according to estimator (4.2) for a 100 GeV Higgs signal. The logical AND combination of the P_T^{Miss} and $E - p_z$ cut is clearly preferred.

For different Higgs masses the optimal values of X and Y according to (4.2) are given in Table 4.2. The P_T^{Miss} cut (X) is clearly increasing for increasing Higgs masses, as the P_T^{Miss} spectrum in the signal also gets harder. The $E - p_z$ (Y) cut on the other hand is mostly independent of the Higgs mass.

| Cut Value | M_H [GeV] | | | | | | | |
|-----------|-------------|------|------|------|------|------|------|------|
| | 80 | 90 | 100 | 110 | 120 | 130 | 140 | 150 |
| X [GeV] | 9.4 | 12.6 | 14.0 | 14.6 | 19.6 | 19.6 | 24.8 | 24.8 |
| Y [GeV] | 47.4 | 47.6 | 47.6 | 47.6 | 47.6 | 47.4 | 48.6 | 48.6 |

Table 4.2: Best cut settings for the cut $P_T^{Miss} > X$ AND $E - p_z < Y$ as a function of the Higgs mass.

In order to retain a reasonable sensitivity also for lower Higgs masses, the final cut on the ej class is chosen to be slightly softer than what was suggested by the estimator:

$$P_T^{Miss} > 11 \text{ GeV AND } E - p_z < 49 \text{ GeV.}$$

The cut is shown for NC background and a 100 GeV signal in Figure 4.4.

In the ee event class, the $E - p_z$ and P_T^{Miss} spectra have an analogue shape as for ej (see Figure 4.3) but the background distributions as shown in Figure 4.5 are slightly different. Generally there is much less background present w.r.t. the ej class. Also there is some background from di-lepton production at low values of $E - p_z$. Therefore, in the ee event class only a cut on P_T^{Miss} is made, namely:

$$P_T^{Miss} > 8 \text{ GeV.}$$

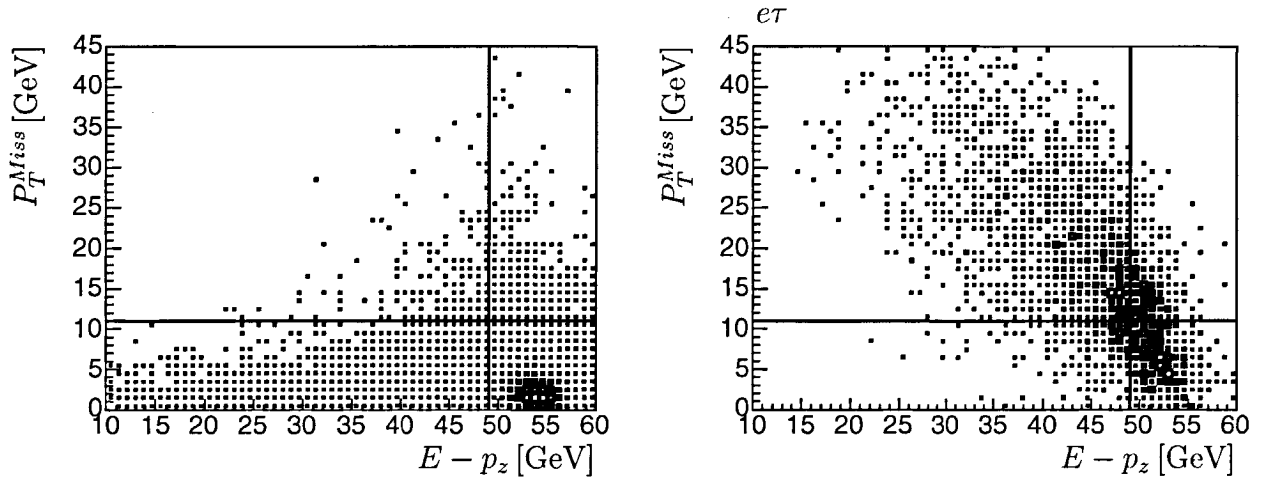


Figure 4.4: P_T^{Miss} versus $E - p_z$ for background (left) and a 100 GeV Higgs signal (right) for the ej event class. The straight lines denote the cut positions. Only the upper left quadrant as defined by these lines is allowed. The centre of gravity of the background at $E - p_z \approx 54$ GeV and low P_T^{Miss} is clearly cut out.

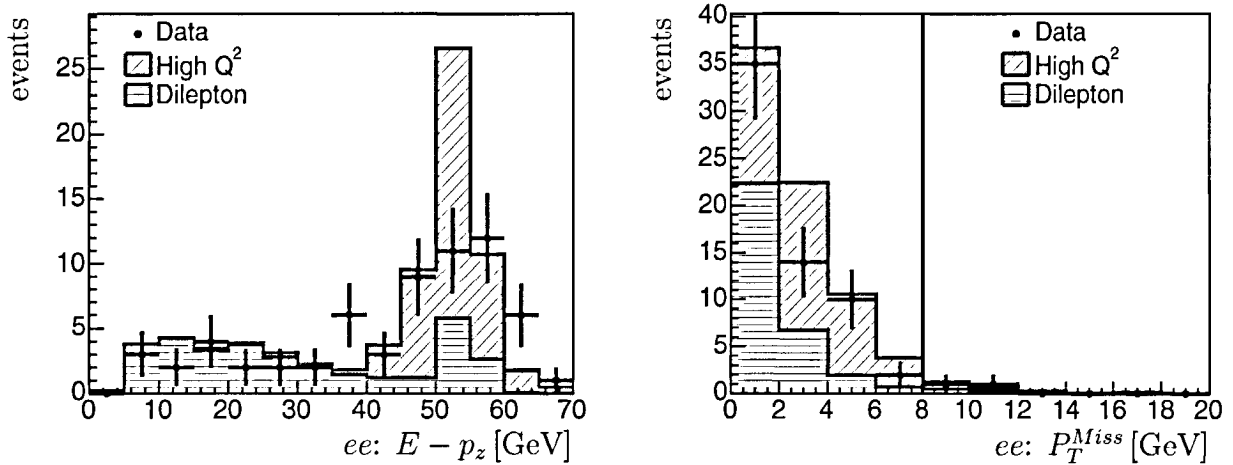


Figure 4.5: $E - p_z$ (left) and P_T^{Miss} (right) distributions for the ee event class ($e\tau$ topology) for the 99/00 dataset after preselection. The vertical line in the P_T^{Miss} spectrum denotes the cut position.

4.1.3 Electron scattering angle

In deep inelastic neutral current reactions the electron scattering angle is closely related to the transferred momentum squared Q^2 via:

$$Q^2 = 2EE'(1 + \cos\theta_e). \quad (4.3)$$

E and E' are the energies of the incoming and the scattered electron respectively. Since the deep inelastic scattering cross section drops with $1/Q^4$, the electron scattering angle θ_e will

peak towards large values. The signal on the other hand is boosted more and more in the forward direction (see Figure 3.3) with increasing Higgs mass. For $\tau\tau$ this is demonstrated in Figure 4.6, which is done after the $E - p_z$ cut. The final cut is:

For all electron classes: $\theta_e < 120^\circ$.

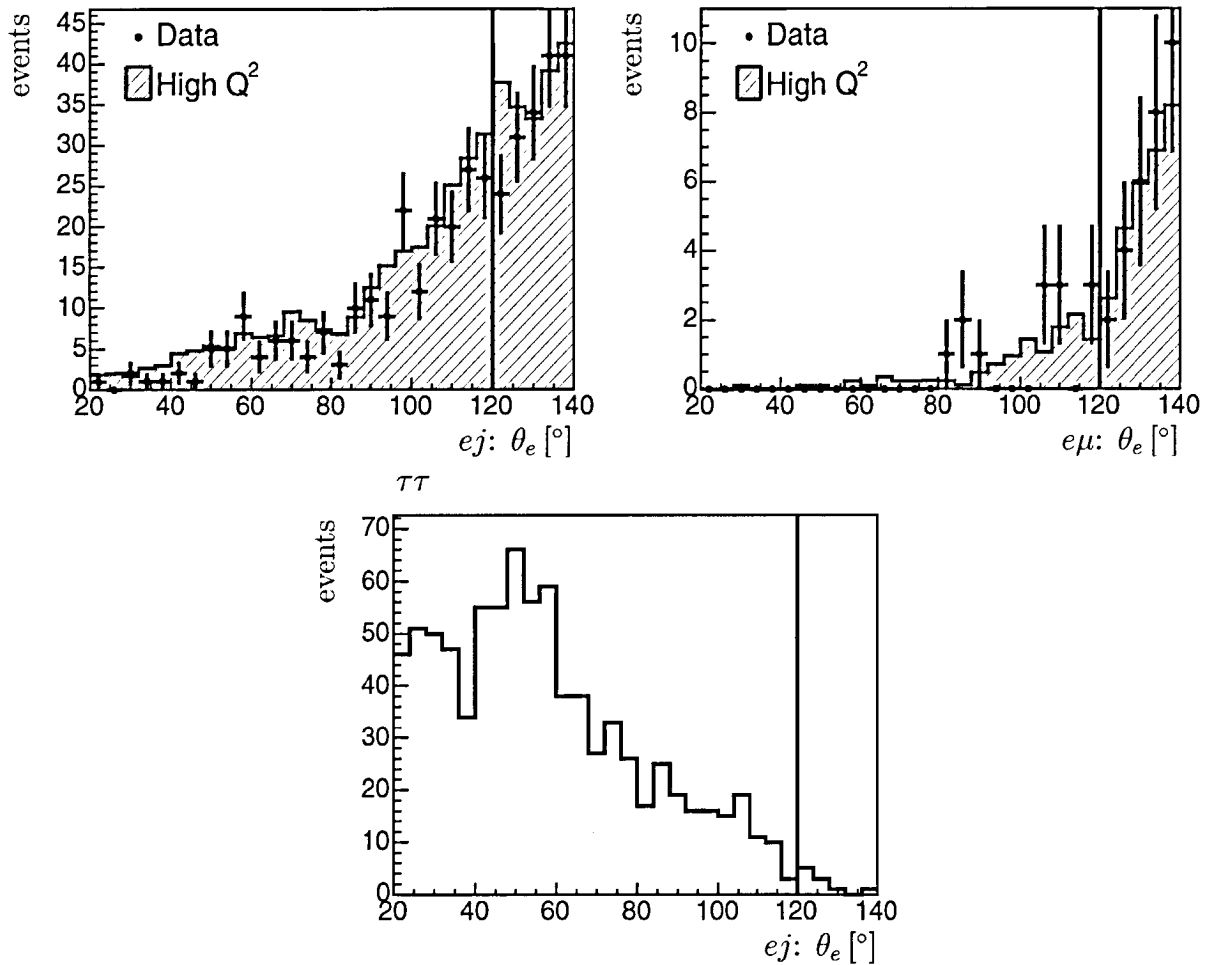


Figure 4.6: θ_e for the ej (top left) and $e\mu$ (top right) event classes for $\tau\tau$. The vertical line denotes the cut position. The cut removes a considerable amount of background but only a small amount of signal events (bottom) as shown for the case of a 100 GeV signal. The signal distribution for other event classes is analogue.

The relative loss in signal events due to this cut as a function of the Higgs mass for the ej event class in the case of $\tau\tau$ is summarised in Table 4.3. The cut affects the signal only for Higgs masses below ~ 100 GeV.

For the $e\tau$ decay topology the cut on θ_e is only applied in the $e\mu$ event class. Its distribution looks identical to Figure 4.6 (top right). The ej and ee event classes are already relatively background free compared to e.g. ej in $\tau\tau$, such that the θ_e cut is simply

| | | | | | | | | |
|------------------|-----|-----|-----|-----|-----|-----|-----|-----|
| M_H [GeV] | 80 | 90 | 100 | 110 | 120 | 130 | 140 | 150 |
| $\Delta S/S$ [%] | 4.4 | 2.3 | 1.2 | 0.5 | 0.1 | 0.0 | 0.0 | 0.0 |

Table 4.3: *Relative loss in signal events for different Higgs masses due to the cut on θ_e . These numbers were calculated for e_j in $\tau\tau$ but different event classes yield very similar numbers, since the θ distribution for the signal does basically not depend on the particle type.*

not needed there. The reason for the better background situation in $e\tau$ is the much harsher cut on P_T^{Miss} and $E - p_z$ (see previous section). The number of surviving events in data and background for both topologies after this cut is summarised in Tables 4.4 up to 4.7 on the line “ $\theta_e < 120^\circ$ ”.

4.2 Isolation Criteria

In contrast to jets from NC events, high energetic τ -jets are completely contained in a narrow cone around the initial τ momentum. Furthermore in a signal from a massive doubly charged Higgs, the Higgs decay products are back-to-back and also mostly isolated from the rest of the event (pseudoscattered lepton, proton remnant). This isolation is therefore exploited using all tracks in the event, which fulfil the Lee West track quality criteria. For this purpose two cones around the candidate tracks are defined:

- Inner cone: $R_{\eta\phi} < 0.15$
- Outer cone: $R_{\eta\phi} < 1.5$

The outer cone is chosen such that it covers a region large enough to separate NC jets (with several or many tracks inside that cone) from τ -jets. Still the outer cone does not include the second candidate track, since the candidates are back-to-back and therefore $\Delta R_{\eta\phi}^{candidates} \gtrsim \pi$. The inner cone is chosen such as to contain all tracks originating from a τ decay e.g. all charged particles from a 3-prong τ decay.

The $\eta\phi$ -distance between a τ -jet and its closest track is displayed in Figure 4.7 for a signal of a 100 GeV Higgs. For 1-prong τ -jets the closest track in $\eta\phi$ is usually the second candidate, which explains the peak at $\Delta R_{\eta\phi} \approx \pi$, while 3-prong τ -jets have their closest track well inside the inner cone (left vertical line).

The following quantities are then defined:

- #prongs $\stackrel{def}{=} \text{Number of good quality tracks}^3$ within the inner cone, including the candidate track.
- #outside tracks $\stackrel{def}{=} \text{Number of good quality tracks between the inner and outer cone.}$

³See section 3.2 for an explanation of the term “good quality track”

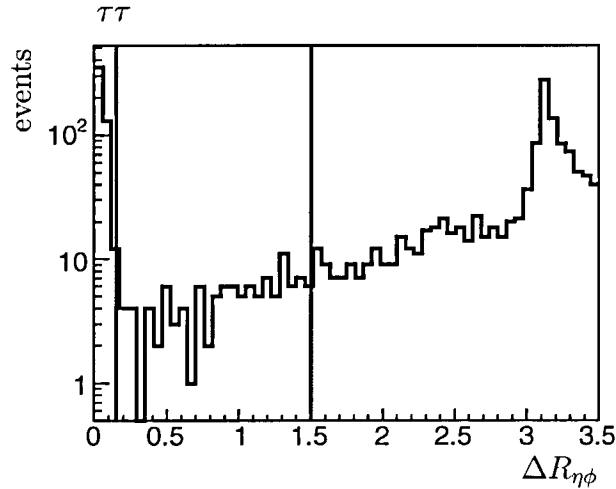


Figure 4.7: $\eta\phi$ -Distance between τ -jet candidates and their closest track. The vertical lines denote the inner and outer cone.

4.2.1 Lepton Isolation

Electrons and muons originating from τ decays are all 1-prongs. Also in most signal events there is no additional track between the inner and outer cone around a lepton candidate. It can however happen that the pseudoscattered lepton comes into the acceptance region and this will then show up in the $\eta\phi$ -region between the inner and outer cone of one of the candidates.

In the SM background also most leptons are 1-prongs and relatively isolated, e.g. the scattered electron in NC or di-lepton production. But in some cases leptons can also appear within or close to jets, e.g. from (semi-)leptonic meson decays.

Since especially the lepton classes $e\mu$ and ee are already low on background, and since signal and background look similar as far as lepton isolation is concerned, only a very soft isolation requirement is used for leptons:

For all lepton candidates: #prongs = 1 AND #outside tracks \leq 1.

Notably the requirement “#outside tracks \leq 1” allows for the possibility to have the pseudoscattered lepton in the acceptance region.

4.2.2 Hadron Isolation

As mentioned above the main use of isolation criteria is the distinction between τ -jets and other jets. The cut used here is:

For all τ -jet candidates: #outside tracks = 0.

The cut does still allow for 3-prong τ decays since all tracks from the τ will be contained in the inner cone (see Figure 4.7) and will therefore not be counted as outside tracks. It

does however not allow for the pseudoscattered lepton to end up between the inner and outer cone of a τ -jet candidate. Two quantities can be used to visualise the events, which are affected by this cut:

- $R_{close} \stackrel{def}{=} \eta\phi$ -distance to the **closest track outside of the inner cone** of $R = 0.15$. If a τ -jet candidate in an event is found with $R_{close} > 1.5$ the candidate will pass the cut since in that case there is no track within $0.15 < R < 1.5$.
- $R_{far} \stackrel{def}{=} \eta\phi$ -distance to the **furthestmost track inside the outer cone** of $R = 1.5$. If there's no track within $R = 1.5$ then $R_{far} = 0$. If a τ -jet candidate in an event is found with $R_{far} < 0.15$ the candidate will pass the cut because there is no track within $0.15 < R < 1.5$.

In the R_{close} and R_{far} distributions the number of events, which survive or are rejected by the cut described above can be seen. This is exactly the advantage over a plot, which just contains the $\eta\phi$ -distance to all other tracks in the event.

Figure 4.8 shows the R_{close} and R_{far} distributions for the 99/00 dataset for the ej and jj classes at the current cut level ($\tau\tau$ selection). For the ej class of the $e\tau$ selection, the μj class ($\tau\tau$) and for the old dataset the distributions are similar but with smaller statistics. The number of surviving events in data and background for both topologies after this cut is summarised in Tables 4.4 up to 4.7 on the line "Isolation".

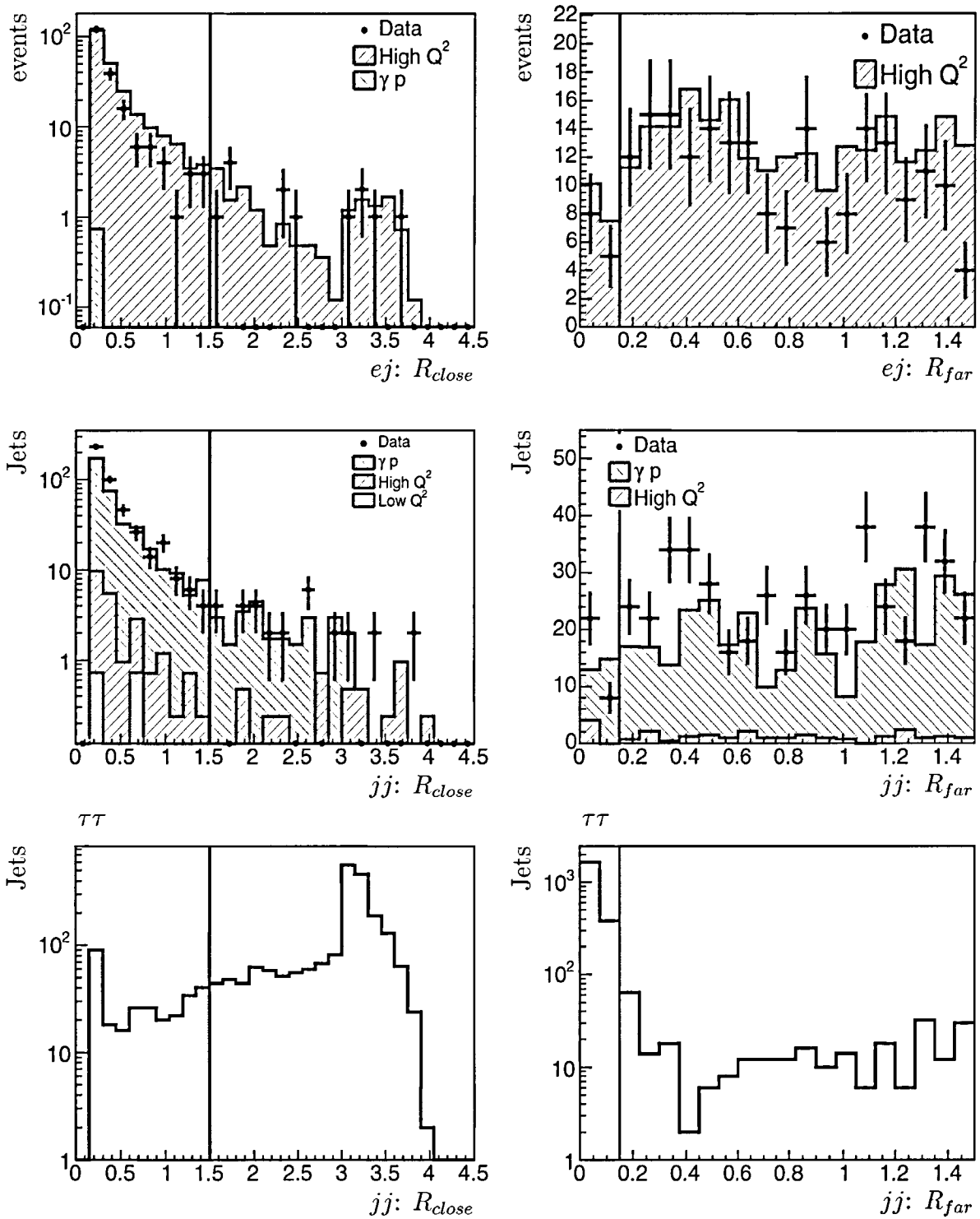


Figure 4.8: Jet isolation variables R_{close} and R_{far} as described in the text for the ej (top) and jj (middle and bottom) event classes. For jj both jets enter the plots, therefore the number of events is half the number of jets. Events/jets to the left (right) of the vertical line in the R_{close} (R_{far}) distribution are rejected. From the signal distributions (bottom plots, 100 GeV Higgs) it becomes clear that the bulk of the events/jets survives.

4.3 Inelastic Background

At this stage of the selection, most of the remaining background in the ej and jj event classes has an additional activity in the forward region in form of forward tracks and/or clusters in the LAr. This is illustrated with an event display picture for an example NC background event in Figure 4.9. The tracks and clusters in the forward region of this picture belong to the broken up proton remnant as a consequence of the inelasticity of the event.

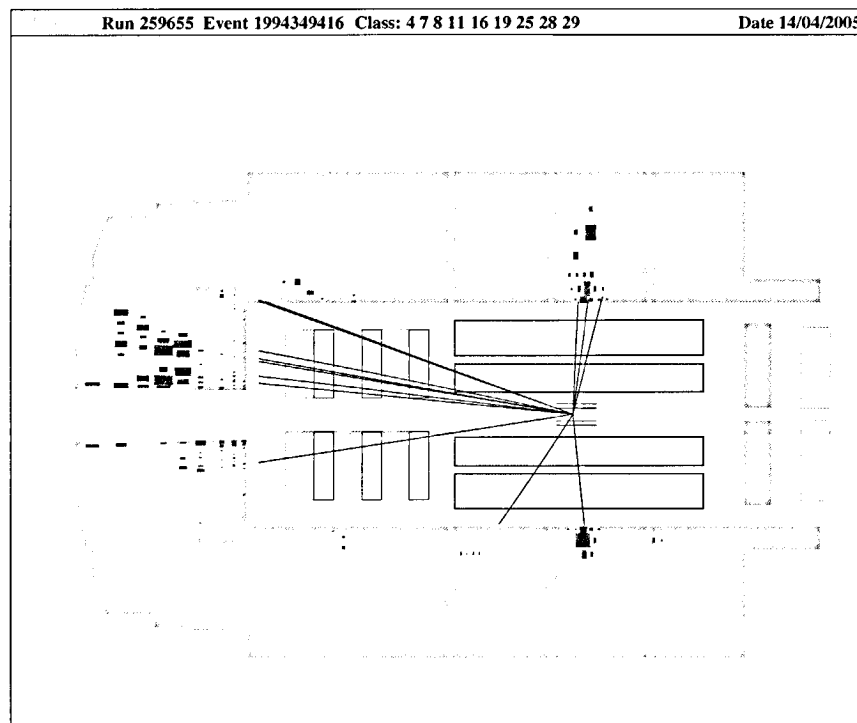


Figure 4.9: An event display (side-view) of a typical NC background event in the MC after the jet isolation cut. The isolated electron (lower hemisphere) and the isolated jet (upper hemisphere) can be clearly seen, as well as the additional activity in the forward region.

The signal on the other hand is dominantly produced elastically. From Table 1.3 it follows that the elastic and quasielastic contributions to the total Higgs production cross section are 80% for Higgs production via h_{ee} and 75% for $h_{e\tau}$. The SM background for an elastic signal is very small. The idea is therefore to separate elastic and inelastic events in order to obtain a pure, background free (especially free from inelastic background) selection for the elastically produced Higgs. The inelastic background can be identified by the use of the following quantity:

η_{max}^{def} Maximum Pseudorapidity of a LAr calorimeter cluster, which does not belong to either one of the candidates or any identified electron.

A large η_{max} is an indicator for activity, which is not connected to an elastically produced signal event, in the forward region. The exclusion of clusters belonging to identified electrons in the η_{max} calculation is useful mainly for h_{ee} induced Higgs production, because in that case the pseudoscattered lepton is an electron and has tendency to go into the forward region (see Figure 3.3). In case the pseudoscattered lepton is a τ ($e\tau$ topology), which decays hadronically, it cannot be distinguished from a proton remnant and therefore η_{max} may be large even for a certain amount of elastic signal events. The following separation is made:

An event is called inelastic (elastic) for $\eta_{max} > 2.8$ ($\eta_{max} \leq 2.8$).

This distinction is only made for the ej ($\tau\tau$ and $e\tau$) and jj event classes, where the inelastic background is large. The separation of events into elastic/inelastic is shown in Figure 4.10. For the signal most of the elastically produced Higgs (4.10a) end up with $\eta_{max} \leq 2.8$. Inelastically produced Higgs (4.10b) and most data and background events are inelastic. The η_{max} distribution for the quasielastic Higgs signal ($0 < Q^2 < 4 \text{ GeV}^2$) looks very similar to the elastic signal. The jj class shows 3 potentially interesting data events at $\eta_{max} = 0$ (4.10d), which are not predicted by the background MC, but the statistics is already very small. The η_{max} distribution for ej in the $e\tau$ topology is analogue to ej in $\tau\tau$.

4.4 Invariant Mass Reconstruction

4.4.1 $\tau\tau$ Topology

Since in every τ decay there is at least one unobservable neutrino, which carries away a fraction of the initial τ energy, the reconstruction of the invariant mass of a τ -pair is not as straightforward as e.g. for a μ -pair. However, for high energetic τ leptons ($E_\tau \gg m_\tau$) the invariant mass of the τ -pair can be reconstructed, since all particles from the τ decay are contained in a narrow cone around the initial τ momentum vector. Assuming in that case, that the unobserved (neutrino) momenta are parallel to the visible (charged) τ decay particles is therefore a good approximation. Thus with the direction of the neutrino momenta fixed, there are only the two unknown neutrino energies to be determined.

If the neutrinos can be supposed to be the only source for missing energy in the event, these neutrino energies can be determined by requiring that the overall momentum balance should be established in the event. This means:

$$\begin{aligned} E_{\nu 1} \hat{p}_{\nu 1}^x + E_{\nu 2} \hat{p}_{\nu 2}^x + p_{vis}^x &= r_x \\ E_{\nu 1} \hat{p}_{\nu 1}^y + E_{\nu 2} \hat{p}_{\nu 2}^y + p_{vis}^y &= r_y \\ E_{\nu 1} (1 - \hat{p}_{\nu 1}^z) + E_{\nu 2} (1 - \hat{p}_{\nu 2}^z) + (E - p_z)_{vis} &= 55 \end{aligned} \quad (4.4)$$

Here $\hat{p}_\nu^{x,y,z}$ means the x, y or z component of the unit momentum vector of the charged particle(s) of the τ decay. p_{vis}^x, p_{vis}^y and $(E - p_z)_{vis}$ denote the total visible momentum in x or y direction, and the total visible $E - p_z$ in the event respectively. r_x and r_y are the x

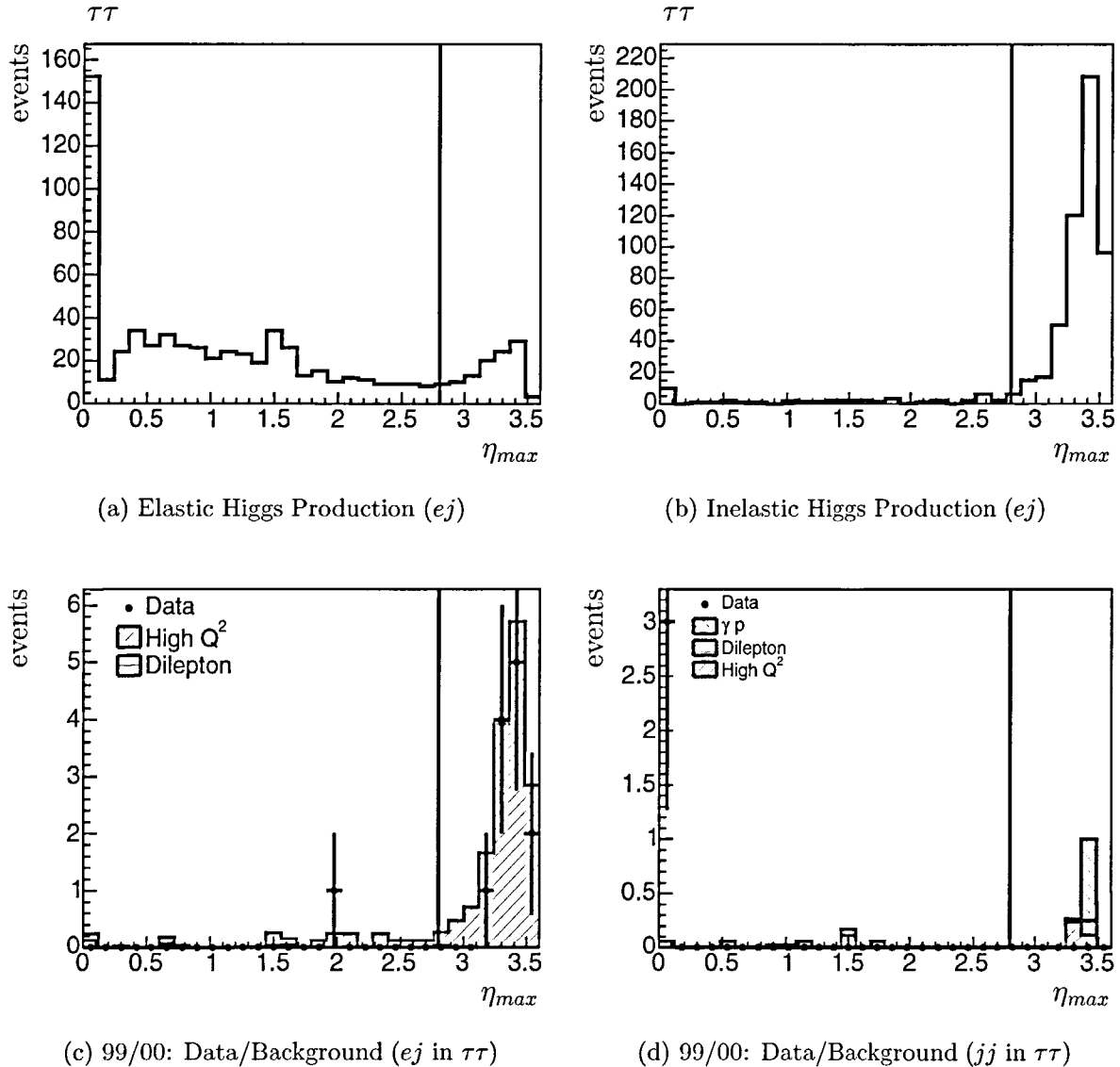


Figure 4.10: η_{max} distributions for elastically ($Q^2 = 0 \text{ GeV}^2$) (top left) inelastically ($Q^2 > 4 \text{ GeV}^2$) (top right) produced Higgs and data/background (bottom). Events to the left (right) of the vertical line are called elastic (inelastic). Events where η_{max} is undefined (e.g. events, where there are only LAr clusters, which belong to one of the candidates) are plotted at $\eta_{max} = 0$ and are therefore treated as elastic.

and y component of the missing transverse momentum of the event, e.g. missing p_T of the proton remnant in the beam pipe.

The system of equations (4.4) is over constrained with 3 equations and only 2 unknown quantities, namely the neutrino energies E_{ν_1} and E_{ν_2} . Several ways of solving this system of equations exist. In this analysis the third equation in (4.4) is used to express E_{ν_2} in terms

of $E_{\nu 1}$ and the first two equations are combined to give the total missing transverse momentum squared $r^2 \equiv r_x^2 + r_y^2$. Finally r^2 is minimised w.r.t. $E_{\nu 1}$:

$$\begin{aligned} E_{\nu 2} &= \frac{55 - (E - p_z)_{vis} - E_{\nu 1}(1 - \widehat{p}_{\nu 1}^z)}{1 - \widehat{p}_{\nu 2}^z} \\ \frac{\partial r^2}{\partial E_{\nu 1}} &= 0 \end{aligned} \quad (4.5)$$

The calculation yields:

$$\begin{aligned} E_{\nu 1} &= \frac{-B}{A} \\ B &= \frac{(\widehat{p}_{\nu 2}^x \widehat{p}_{\nu 1}^x + \widehat{p}_{\nu 2}^y \widehat{p}_{\nu 1}^y)(55 - (E - p_z)_{vis})}{(1 - \widehat{p}_{\nu 2}^z)} + \widehat{p}_{\nu 1}^x p_{vis}^x + \widehat{p}_{\nu 1}^y p_{vis}^y \\ A &= (\widehat{p}_{\nu 1}^x)^2 + (\widehat{p}_{\nu 1}^y)^2 - \frac{(\widehat{p}_{\nu 2}^x \widehat{p}_{\nu 1}^x + \widehat{p}_{\nu 2}^y \widehat{p}_{\nu 1}^y)(1 - \widehat{p}_{\nu 1}^z)}{(1 - \widehat{p}_{\nu 2}^z)} \end{aligned} \quad (4.6)$$

Now the invariant mass of the τ pair can be reconstructed by adding the calculated neutrino momenta $p_{\nu i} = E_{\nu i} \cdot \widehat{p}_{\nu i}$ to the visible τ momenta p_i^{vis} ($i = 1, 2$):

$$M^2 = (p_1^{vis} + p_{\nu 1} + p_2^{vis} + p_{\nu 2})^2, \quad (4.7)$$

where all $p_{1,2,\nu 1,\nu 2}$ are now the full 4-momentum vectors. The results from this calculation are shown in Figure 4.11 for the combined signal MC containing elastic, quasielastic and inelastic Higgs production, weighted each to its relative contribution. The reconstructed mass distributions have resolutions $\sigma_{res} \lesssim 3$ GeV. The mass resolution for 96/97 is slightly better for 99/00, because of a better θ resolution in the former dataset.

4.4.2 $e\tau$ Topology

For the $e\tau$ decay topology the momentum balance equations are even simpler than (4.4) because there is only one τ -candidate, or in other words only one missing neutrino momentum.

$$\begin{aligned} E_{\nu} \widehat{p}_{\nu}^x + p_{vis}^x &= r_x \\ E_{\nu} \widehat{p}_{\nu}^y + p_{vis}^y &= r_y \\ E_{\nu}(1 - \widehat{p}_{\nu}^z) + (E - p_z)_{vis} &= 55 \end{aligned} \quad (4.8)$$

For instance from the last equation in (4.8) the neutrino energy E_{ν} could be directly calculated, which then could be used to calculate the invariant mass of the $e\tau$ system. However, this is not done but instead the same calculation as for $\tau\tau$ is performed. Formally this has the ‘‘advantage’’ that both longitudinal and transverse momentum balance are taken into account. It means also that even the direct electron in $e\tau$ gets a missing momentum assigned to it. The calculation from the previous section should take care by

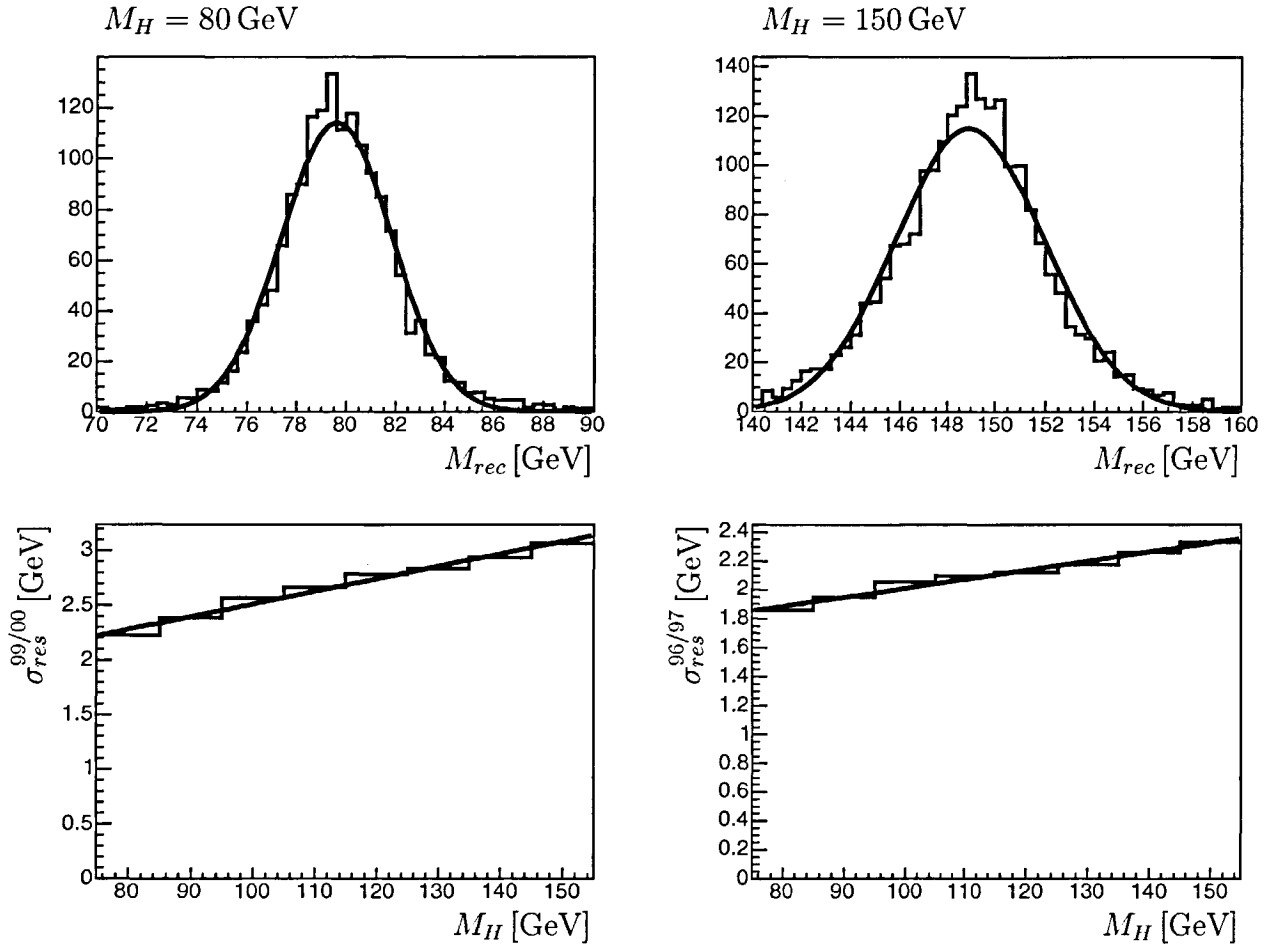


Figure 4.11: Reconstructed $\tau\tau$ masses for true Higgs masses of 80 GeV (top left) and 150 GeV (top right) and their respective Gaussian fits. 1-sigma mass resolutions for 99/00 conditions (bottom left) and 96/97 conditions (bottom right) as a function of the true Higgs mass. Both resolution plots include a linear fit. The 96/97 mass resolution is slightly better than for 99/00.

itself that this missing electron momentum turns out to be small for a real $e\tau$ signal.

The results for $e\tau$ are displayed in Figure 4.12. The mass resolutions are slightly worse than for $\tau\tau$, but still $\sigma_{res} \lesssim 4$ GeV. The reason for this difference is due to the harder P_T spectrum of the scattered lepton for $e\tau$ (see Figure 3.3), where the scattered lepton is a τ and therefore part of its momentum is undetected even if it ends up in the detector acceptance region. This additional missing momentum in the event is not taken into account in the method described above.

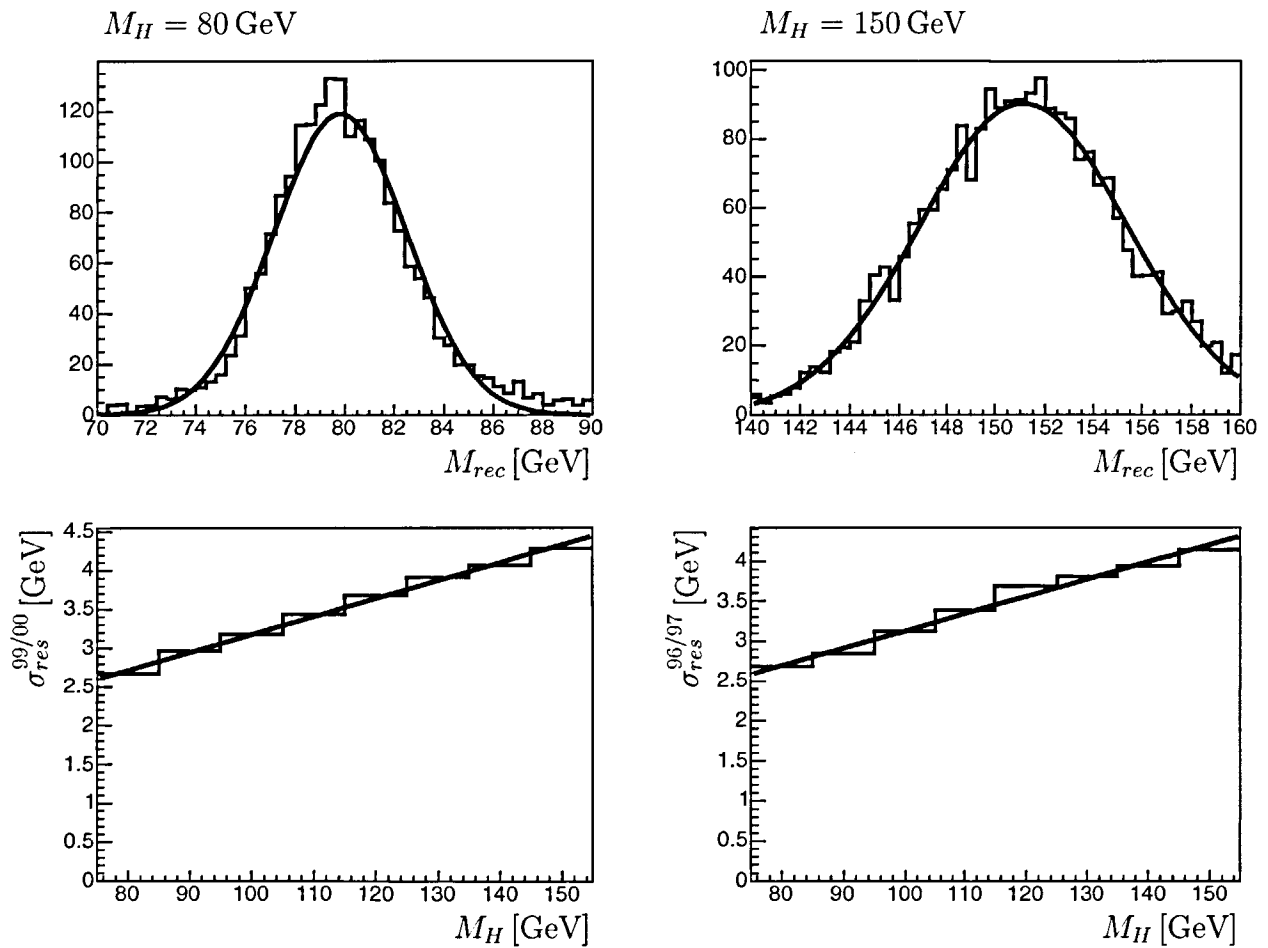


Figure 4.12: Same plots as in Figure 4.11 but for the $e\tau$ decay topology. Mass resolutions are slightly worse than for $\tau\tau$.

4.4.3 Mass Requirement

Since the invariant mass of the doubly charged Higgs can be reliably determined, a simple cut is applied to reject background, which lies clearly below the considered mass range of $80 < M_H < 150$ GeV for this analysis. The cut is applied on all event classes in $\tau\tau$ and $e\tau$.

$$M_{rec} > 65 \text{ GeV}$$

The effect of the cut is shown in Figures 4.13 and 4.14 for the 99/00 dataset.

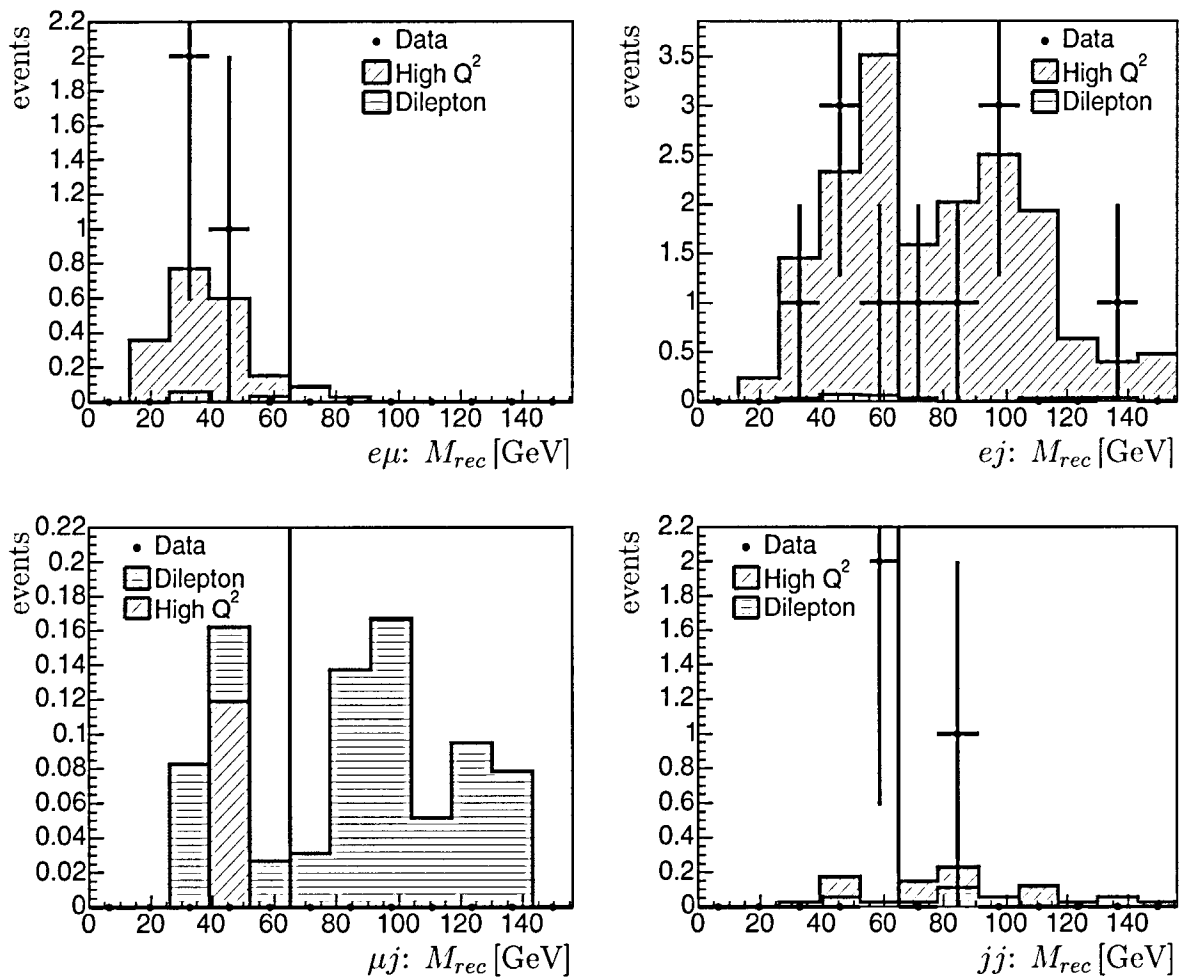


Figure 4.13: Reconstructed Mass distributions for all event classes in $\tau\tau$ for the 99/00 dataset. The vertical line denotes the cut position.

The number of surviving events in data and background for both topologies after this cut is summarised in Tables 4.4 up to 4.7 on the line “ $M > 65$ ”. The event numbers are small already and agree within about $\pm 1\sigma$. In other words: No excess is found in the data.

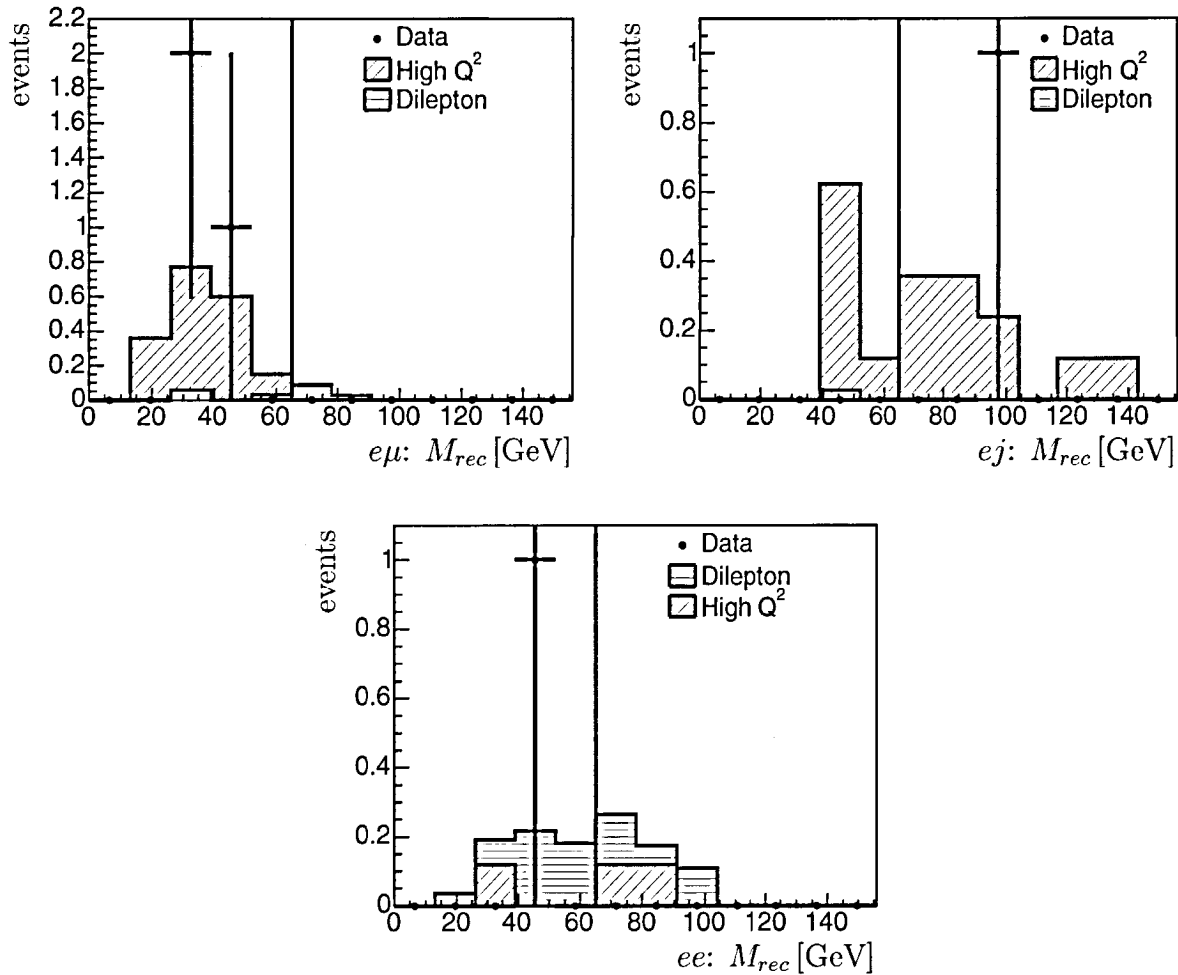


Figure 4.14: Same as Figure 4.13 but for the $e\tau$ event classes.

4.5 Charge Requirement

The last property, which is exploited to separate signal from background is the condition on the charge of the two candidates. The sum of the candidate's charges must equal twice the incoming lepton beam charge. For both datasets the incoming lepton was positive, therefore:

$$C_1 = +1 \quad \text{AND} \quad C_2 = +1.$$

$C_{1,2}$ are the candidate's charges (in multiples of the elementary charge). The background from di-lepton production is expected to be dominantly at $C_1 + C_2 = 0$. In order to assure that the charges are reliably measured, this cut is only applied for candidates, which fulfil two charge quality conditions.

1. For $\#prongs > 1$ (see section 4.2) the sum of the charges of all prongs makes up for the total charge of a candidate. It is however not clear how well e.g. 3 tracks in a

narrow cone can be separately measured. Since the di-lepton background is made almost exclusively from 1-prong candidates, the cut is only applied for candidates where $\#\text{prongs}=1$.

2. The charges are determined by the curvatures $\kappa_{1,2}$ of the tracks. For short tracks or tracks with very high P_T the curvature becomes difficult to measure. The cut is only applied if the relative error on the curvature of a candidate is less than 50%: $\delta\kappa_i/\kappa_i < 0.5$.

In Figure 4.15 the sum of the charges for a $\tau\tau$ and $e\tau$ signal is plotted. Events with charge ± 1 can occur if only one of the candidates fulfils the conditions above. Events with $\sum C_i \geq 1$ pass the cut (vertical lines). In rare cases even both candidates can fail the charge quality conditions. Then the event is forced to have $C_1 + C_2 = 2$, which means that the cut is passed.

Apparently more events are rejected in $\tau\tau$ than in $e\tau$. An analysis of the rejected events shows that in almost all cases the pseudoscattered lepton (which has opposite charge) is wrongly taken as a candidate. This is more likely to happen in $\tau\tau$ where the scattered electron has a harder P_T spectrum than the decay products from the scattered τ in $e\tau$. For both topologies the cut enhances the purity⁴ of the sample. The purity of the events, which survive the charge cut, is $\sim 100\%$.

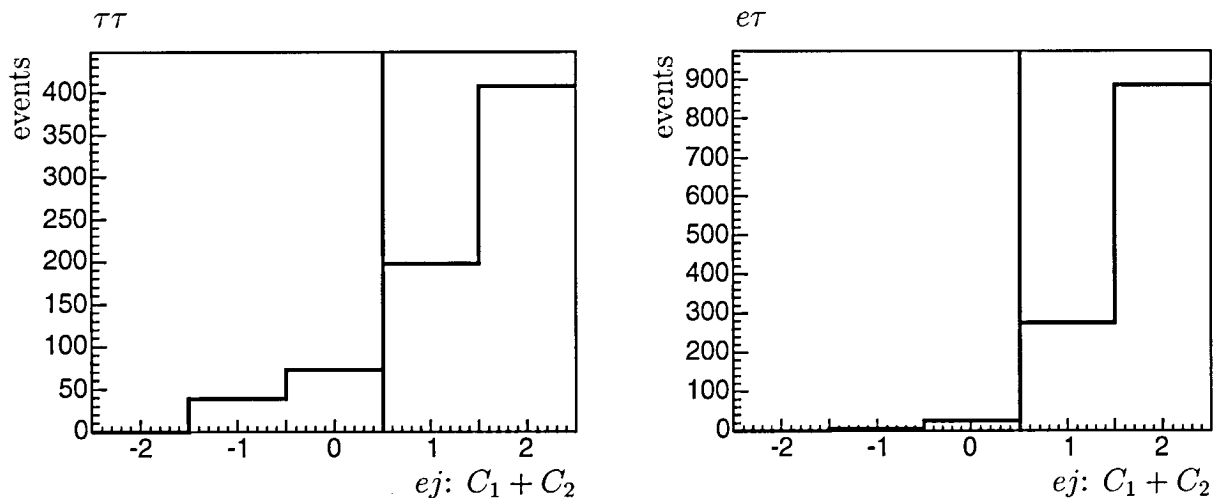


Figure 4.15: Sum of the charges for a 100 GeV Higgs signal in the ej class for $\tau\tau$ (left) and $e\tau$ (right).

The same plots for data and background are given in Figure 4.16 ($\tau\tau$) and 4.17 ($e\tau$). Di-lepton background is removed by the charge cut, while NC background still survives, mostly in ej .

⁴The purity in this context is the number of events with correct choice of the candidates in the signal divided by all events.

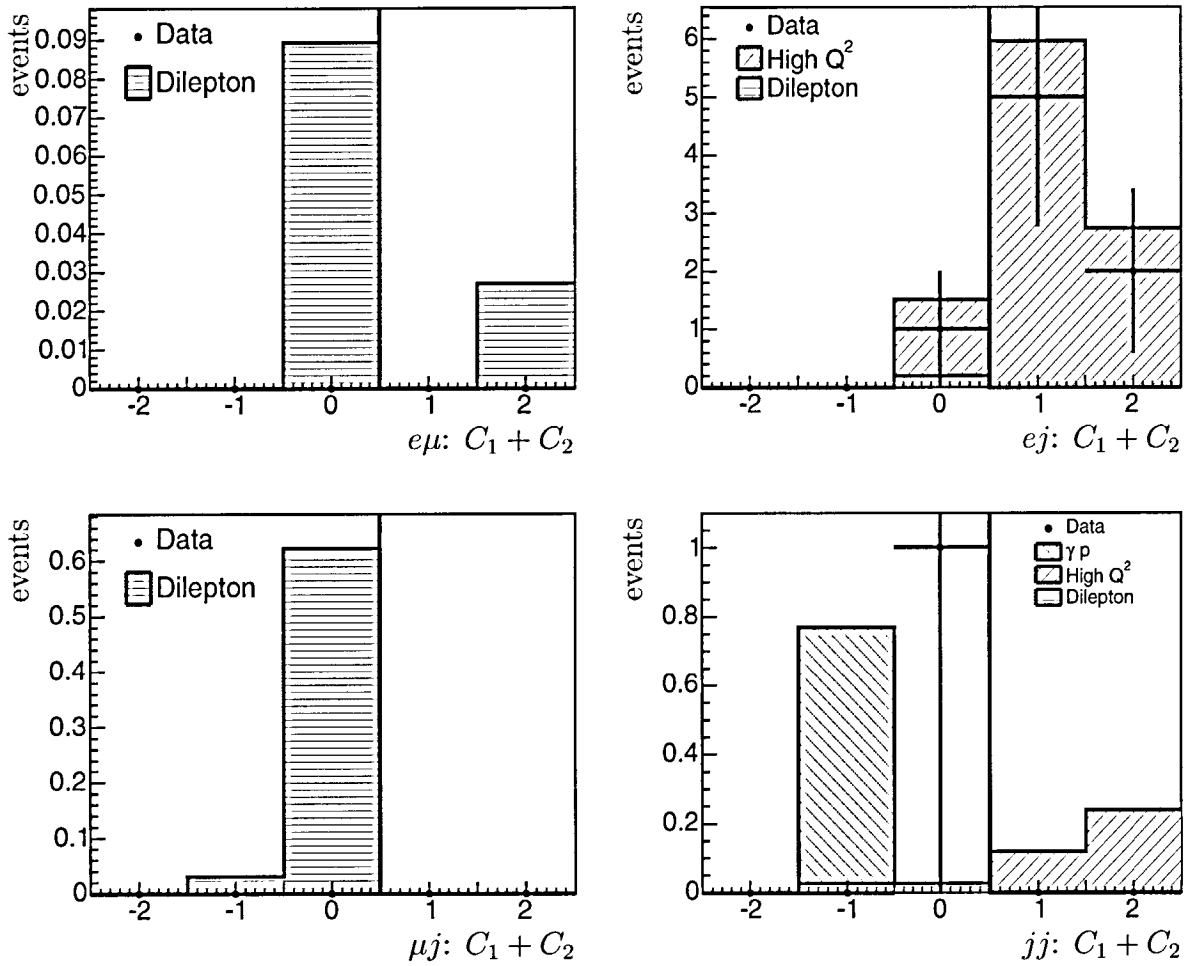


Figure 4.16: Sum of the charges ($\tau\tau$) of the candidates for the 99/00 dataset after the cut on the invariant mass. Events to the right of the vertical lines survive the charge criteria.

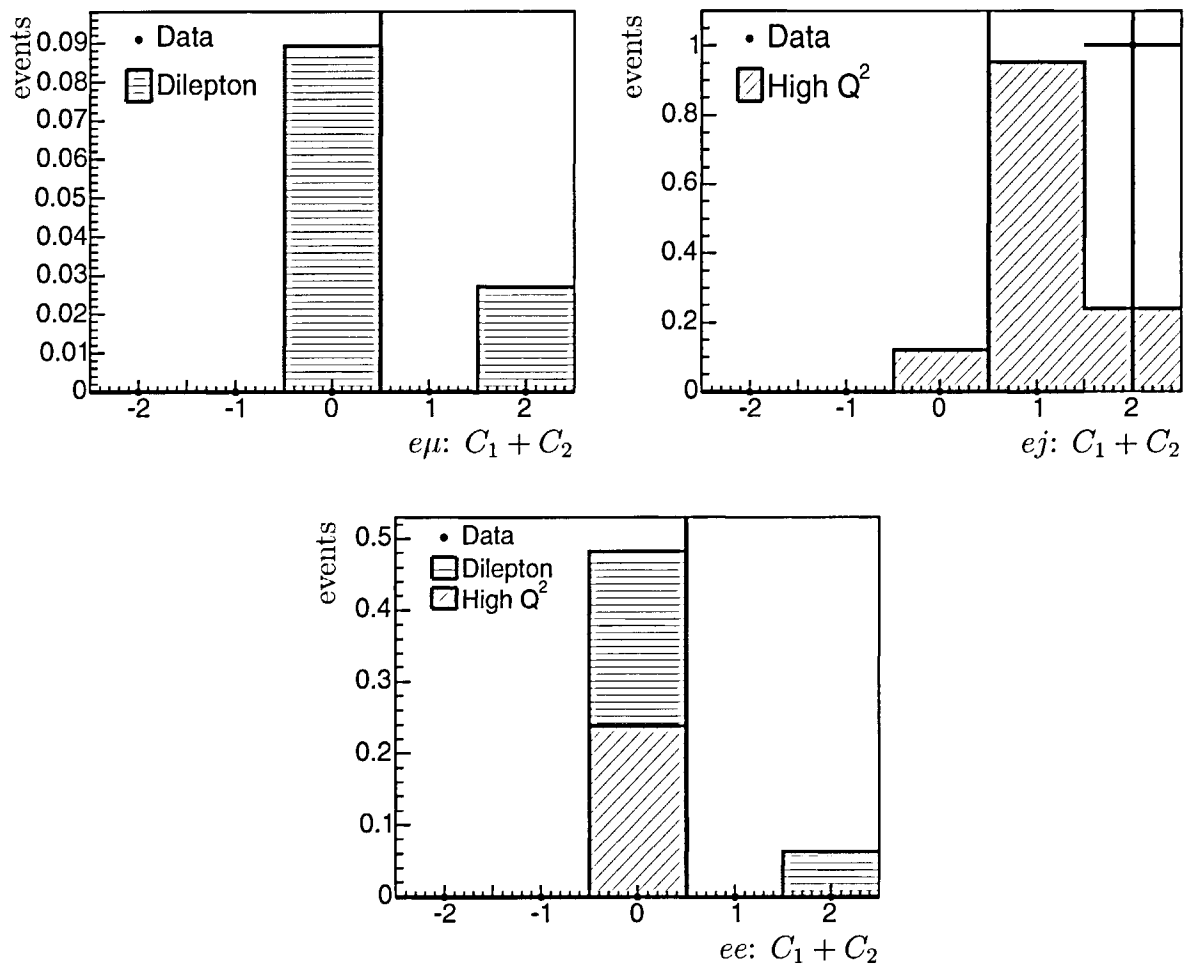


Figure 4.17: Same as Figure 4.16 but for the $e\tau$ topology.

4.6 Final Cutflows

The numbers of surviving events after each cut are summarised in the Tables 4.4, 4.5, 4.6 and 4.7 for the different datasets and decay topologies. The last line in each Table shows the number of surviving elastic and inelastic events after the charge cut for the ej and jj event classes where this separation is made. Most of the remaining background in ej is inelastic.

| Cut | Bkg MC | | | | | Data 99/00 | | | | |
|------------------|--------|---------|---------|-----------|------|------------|------|---------|-------|------|
| | $e\mu$ | ej | μj | jj | Sum | $e\mu$ | ej | μj | jj | Sum |
| Preselection | 40.8 | 7461 | 5.6 | 304 | 7811 | 43 | 7467 | 7 | 380 | 7897 |
| $E - p_z < 45$ | (40.8) | 448 | (5.6) | 193 | 687 | (43) | 386 | (7) | 243 | 679 |
| $\theta_e < 120$ | 12.3 | 260 | (5.6) | (193) | 471 | 13 | 215 | (7) | (243) | 478 |
| Isolation | 2.0 | 17.8 | 0.89 | 1.7 | 22.4 | 3 | 13 | 0 | 3 | 19 |
| $M > 65$ | 0.12 | 10.5 | 0.63 | 1.5 | 12.8 | 0 | 8 | 0 | 1 | 9 |
| Charge | 0.03 | 8.7 | 0.00 | 0.44 | 9.2 | 0 | 7 | 0 | 0 | 7 |
| ela/inela | | 0.8/7.9 | | 0.15/0.29 | | | 0/7 | | 0/0 | |

Table 4.4: Cutflow for background and data for $\tau\tau$ in the 99/00 dataset. Numbers in brackets indicate that the cut is not applied for this event class.

| Cut | Bkg MC | | | | | Data 96/97 | | | | |
|------------------|--------|---------|---------|-----------|------|------------|------|---------|------|------|
| | $e\mu$ | ej | μj | jj | Sum | $e\mu$ | ej | μj | jj | Sum |
| Preselection | 16.4 | 3042 | 2.6 | 131 | 3192 | 14 | 2716 | 5 | 148 | 2883 |
| $E - p_z < 45$ | (16.4) | 193 | (2.6) | 81.6 | 293 | (14) | 170 | (5) | 86 | 275 |
| $\theta_e < 120$ | 5.1 | 116 | (2.6) | (81.6) | 205 | 4 | 92 | (5) | (86) | 187 |
| Isolation | 1.3 | 8.8 | 0.32 | 1.2 | 11.6 | 0 | 8 | 0 | 0 | 8 |
| $M > 65$ | 0.10 | 5.5 | 0.28 | 0.91 | 6.8 | 0 | 3 | 0 | 0 | 3 |
| Charge | 0.06 | 4.3 | 0.00 | 0.48 | 4.8 | 0 | 3 | 0 | 0 | 3 |
| ela/inela | | 0.4/3.8 | | 0.32/0.16 | | | 0/3 | | 0/0 | |

Table 4.5: Cutflow for $\tau\tau$ in the 96/97 dataset.

| Cut | Bkg MC | | | | Data 99/00 | | | |
|-----------------------|--------|----------|-------|------|------------|------|-----|------|
| | $e\mu$ | ej | ee | Sum | $e\mu$ | ej | ee | Sum |
| Preselection | 40.8 | 7461 | 76.0 | 7577 | 43 | 7467 | 61 | 7571 |
| $E - p_z, P_T^{Miss}$ | (40.8) | 27.2 | 2.5 | 70.5 | (43) | 28 | 1 | 72 |
| $\theta_e < 120$ | 12.3 | (27.2) | (2.5) | 42.0 | 13 | (28) | (1) | 42 |
| Isolation | 2.0 | 2.2 | 1.17 | 5.3 | 3 | 1 | 1 | 5 |
| $M > 65$ | 0.12 | 1.3 | 0.55 | 1.9 | 0 | 1 | 0 | 1 |
| Charge | 0.03 | 1.22 | 0.06 | 1.31 | 0 | 1 | 0 | 1 |
| ela/inela | | 0.0/1.22 | | | | 0/1 | | |

Table 4.6: Cutflow for $e\tau$ in the 99/00 dataset.

| Cut | Bkg MC | | | | Data 96/97 | | | |
|-----------------------|--------|-----------|-------|------|------------|------|-----|------|
| | $e\mu$ | ej | ee | Sum | $e\mu$ | ej | ee | Sum |
| Preselection | 16.4 | 3042 | 33.9 | 3092 | 14 | 2716 | 34 | 2764 |
| $E - p_z, P_T^{Miss}$ | (16.4) | 13.2 | 1.2 | 30.8 | (14) | 19 | 1 | 34 |
| $\theta_e < 120$ | 5.1 | (13.2) | (1.2) | 19.5 | 4 | (19) | (1) | 24 |
| Isolation | 1.3 | 0.92 | 0.49 | 2.7 | 0 | 0 | 1 | 1 |
| $M > 65$ | 0.10 | 0.86 | 0.23 | 1.15 | 0 | 0 | 0 | 0 |
| Charge | 0.06 | 0.85 | 0.14 | 1.05 | 0 | 0 | 0 | 0 |
| ela/inela | | 0.42/0.42 | | | | 0/0 | | |

Table 4.7: Cutflow for $e\tau$ in the 96/97 dataset.

The cutflows are also presented for a 100 GeV Higgs signal for $\tau\tau$ (Table 4.8) and $e\tau$ (Table 4.9) for 99/00 conditions. These Tables contain all kinematic régimes (elastic, quasielastic and inelastic) weighted with their relative contributions. The event numbers are normalised such that the sum of all kinematical contributions and all event classes before the first cut is 10000 events. The event numbers after the last cut can be identified as the global efficiencies of this analysis as discussed in section 5.2. They are: 21.7% for $\tau\tau$ and 24.5% for $e\tau$ for a Higgs mass of 100 GeV. It has to be noted that the numbers for the individual event classes do also depend on the branching ratio (see Table 3.4) of the respective event class.

| Cut | $\tau\tau$ signal, $M = 100$ GeV | | | | Sum |
|------------------|----------------------------------|---------|---------|---------|-------------|
| | $e\mu$ | ej | μj | jj | |
| Preselection | 282 | 989 | 739 | 1139 | 3149 |
| $E - p_z < 45$ | (282) | 884 | (739) | 1086 | 2991 |
| $\theta_e < 120$ | 280 | 876 | (739) | (1086) | 2981 |
| Isolation | 260 | 711 | 619 | 791 | 2381 |
| $M > 65$ | 256 | 700 | 617 | 789 | 2362 |
| Charge | 208 | 568 | 613 | 782 | 2171 |
| ela/inela | | 413/155 | | 592/190 | |

Table 4.8: Cutflow for a $\tau\tau$ signal of mass 100 GeV under 99/00 conditions.

| Cut | $e\tau$ signal, $M = 100$ GeV | | | Sum |
|-----------------------|-------------------------------|---------|-------|-------------|
| | $e\mu$ | ej | ee | |
| Preselection | 703 | 2802 | 888 | 4393 |
| $E - p_z, P_T^{Miss}$ | (703) | 1631 | 812 | 3146 |
| $\theta_e < 120$ | 697 | (1631) | (812) | 3140 |
| Isolation | 632 | 1193 | 725 | 2550 |
| $M > 65$ | 627 | 1183 | 715 | 2525 |
| Charge | 599 | 1159 | 688 | 2446 |
| ela/inela | | 621/538 | | |

Table 4.9: Cutflow for an $e\tau$ signal of mass 100 GeV under 99/00 conditions.

Finally, for the ej event class, which has a background expectation significantly different from zero, the invariant mass distributions for data and background are shown in Figure 4.18 after all cuts. See the appendix for a list of the surviving data events.

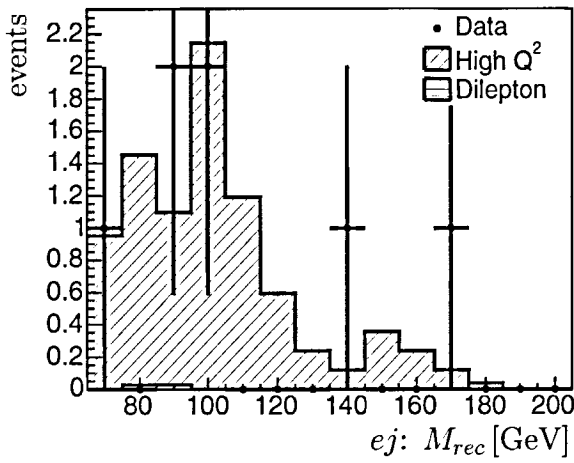
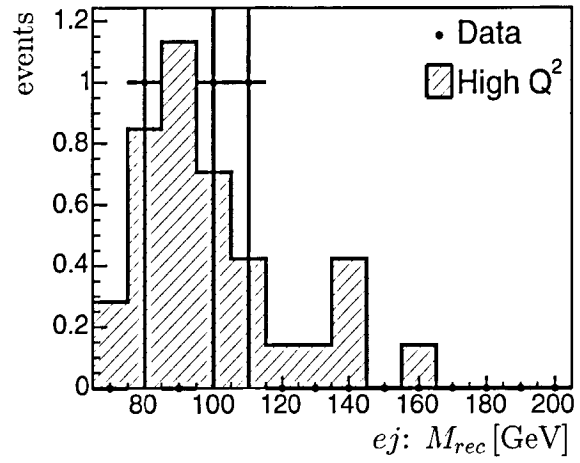
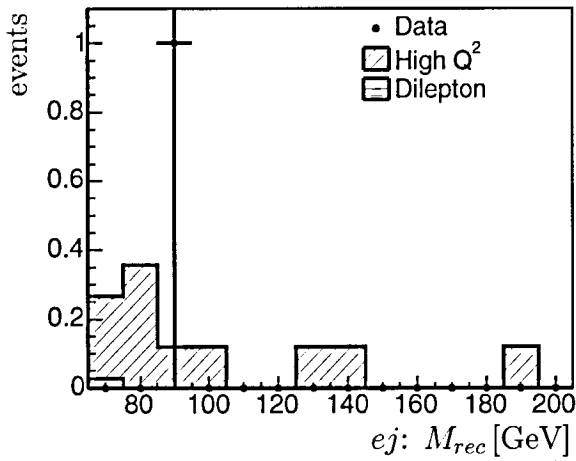
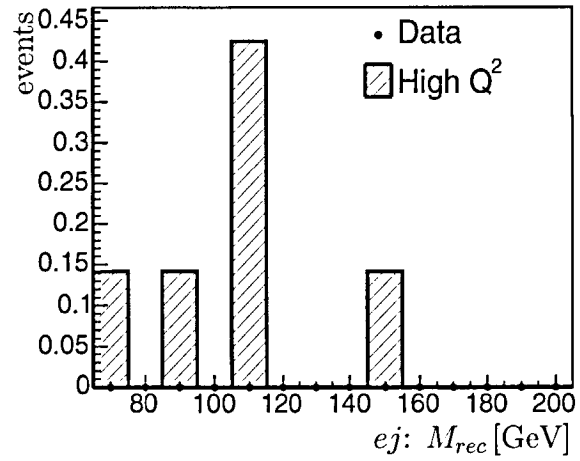
(a) $\tau\tau$ topology, 99/00 dataset(b) $\tau\tau$ topology, 96/97 dataset(c) $e\tau$ topology, 99/00 dataset(d) $e\tau$ topology, 96/97 dataset

Figure 4.18: Reconstructed invariant mass distributions for data and background for the ej event class after all cuts, for both topologies and datasets.

Chapter 5

Results

As neither for the $\tau\tau$ nor for the $e\tau$ selection an excess in data has been found (see previous section), the focus in this chapter is on setting upper limits on the doubly charged Higgs production cross section. For this purpose, systematic errors are estimated first, although they have only a small influence on the final limits.

5.1 Systematic Errors

The total error on the event numbers listed in section 4.6 is made up from a statistical and a systematic error added in quadrature. For low statistics event counting experiments, such as this analysis, the statistical error is usually dominant. Nonetheless, in this section the most important sources for systematic uncertainties are estimated. Most of the systematic errors are the same for signal and background and apply equally to all event classes. It is explicitly noted when a distinction is made.

5.1.1 Signal

Most of the errors were estimated using the signal samples of a 100 GeV Higgs. The list of uncertainties includes:

- **Theoretical uncertainty on the Higgs production cross section.**

Several effects were investigated:

- The uncertainty on the elastic and quasi-elastic contributions depends on the knowledge of the proton form factors, for which 2% are assumed. The inelastic Higgs production cross section on the other hand depends on the parton density function (pdf) used. A variation of the pdf and the scale (Q^2), at which it is evaluated, yields a 20% uncertainty [63] for the inelastic cross section. Weighting these uncertainties by their relative contributions (see Table 1.3) gives the theoretical errors for $\tau\tau$ and $e\tau$:

$$\delta_{theo}^{\tau\tau} = 4.9\% \qquad \delta_{theo}^{e\tau} = 5.3\%.$$

- Initial state radiation (ISR) affects the production cross section. For all generated signal MC, ISR was switched off. The inclusion of ISR affects the cross section by $\sim 1\%$.
- The efficiencies from the quasielastic signal MC may depend on the modelling of the photon-proton interaction. The SOPHIA [31] package is used for this analysis. However for a 100 GeV Higgs ($\tau\tau$ topology) two additional samples with different modelling of the photon-proton vertex have been produced. One with the EPSOFT [64] and the other with the DIFFVM [65] packages. Each sample contains 10000 events and the total number of events surviving after the $\tau\tau$ selection are:

| SOPHIA | DIFFVM | EPSOFT |
|--------|--------|--------|
| 2261 | 2278 | 2272 |

The difference is smaller than a statistical 1-sigma fluctuation and the corresponding systematic uncertainty is therefore neglected.

- **Luminosity measurement and High Voltage control.**

The luminosity and High Voltage uncertainty was globally determined to be 1.5% for HERA I analyses.

- **Lepton identification.**

A 2% error on the electron identification efficiency for electrons with energies $E_e > 10$ GeV (see [52]) is assigned to all electron classes. In the ee event class 4% is used, because the systematic uncertainty for the identification of both electrons is correlated. For the muon identification uncertainty 6% [66] is used in the $e\mu$ and μj event classes.

- **Trigger efficiency.**

For all electron event classes a systematic uncertainty of 0.5% as determined in [52] is assigned to the trigger decision. For the jj class a systematic error of 5% (see section 3.6) is used. For the μj channel, the charged current trigger efficiencies are quoted in [52] to be $\delta_{trig} = (1 - \varepsilon) \cdot 15\% \oplus 2\%$. For a mean trigger efficiency of $\langle \varepsilon \rangle \approx 95\%$ (see section 3.6) this would result in an uncertainty of about 2%. Also the muon triggers ST18 and ST34 are important for μj and their systematic uncertainties have been determined in [54] to be 5% each. No exact determination from data is possible because of the lack of statistics in this event class. An uncertainty of 5% is finally assumed.

- **Tracking uncertainty.**

A 3% systematic uncertainty is assigned to single track reconstruction. Since in this analysis all events need to have at least two tracks and since the systematic uncertainty for the reconstruction of both tracks is correlated, 6% is used for all event classes.

- **θ measurement.**

The θ of all tracks was varied by 3 mrad in either direction. This mainly affects the θ acceptance cuts. The jet isolation requirement is studied separately. The resulting effect on the signal was found to be less than 0.5%.

- **Jet Isolation.**

The global shift in θ for all tracks has only a small impact on the jet isolation cut (see section 4.2), because this cut depends rather on distances between tracks in $\eta\phi$ -space than on absolute angles. The sizes of the inner and outer cone are therefore varied separately by $\pm\Delta R(\theta)$ defined as:

$$\Delta\eta = \frac{\Delta\theta}{\sin\theta} \quad \Rightarrow \quad \Delta R = \sqrt{\left(\frac{\Delta\theta}{\sin\theta}\right)^2 + \Delta\phi^2}, \quad (5.1)$$

where $\Delta\theta = 3$ mrad and $\Delta\phi = 1$ mrad. For the signal only the jj event class is affected by 1.7%.

- **LAr electromagnetic energy scale.**

The LAr electromagnetic energy is varied by 3%. A small effect $< 1\%$ is observed for all event classes except for μj where no shift can be seen.

- **LAr hadronic energy scale.**

A variation of 2% in the hadronic energy yields shifts of 1.3% in jj and 1.6% in ej for $\tau\tau$. The systematic shift in ej for $e\tau$ is much larger with about 7%. The reason for this difference between $\tau\tau$ and $e\tau$ has to be related to the harsh P_T^{Miss} cut in the ej class in $e\tau$.

| Effect | Variation | Event Classes | | | | |
|-----------------------|----------------|---------------|------------|----------|-------------|----------|
| | | $e\mu$ [%] | ej [%] | ee [%] | μj [%] | jj [%] |
| Theory | - | 5.0 (5.4) | 5.0 (5.4) | 5.4 | 5.0 | 5.0 |
| HV, Lumi | - | 1.5 | 1.5 | 1.5 | 1.5 | 1.5 |
| Tracking | - | 6 | 6 | 6 | 6 | 6 |
| μ -ID | - | 6 | - | - | 6 | - |
| e-ID | - | 2 | 2 | 4 | - | - |
| Trigger | - | 0.5 | 0.5 | 0.5 | 5 | 5 |
| Track θ | 3 mrad | <0.5 | <0.5 | <0.5 | <0.5 | <0.5 |
| Jet Isolation | equation (5.1) | 0 | 0 | 0 | 0 | 1.7 |
| LAr e.m. scale | 3% | <1 | <1 | <1 | 0 | <1 |
| LAr had. scale | 2% | 0 | 1.6 (7) | 0 | <0.5 | 1.3 |
| $\sqrt{\Sigma err^2}$ | | 10.2 (10.4) | 8.4 (11.0) | 9.2 | 11.2 | 9.7 |

Table 5.1: Relative systematic errors estimated for the signal efficiency. In cases where the errors differ for $\tau\tau$ and $e\tau$, the numbers in brackets refer to $e\tau$.

5.1.2 Background

Because of the lack of candidate events in data, the background uncertainties are mostly irrelevant for the subsequent limit calculation. If no data events are observed, the limit should not depend on the number of expected background events. Nevertheless in order to show that the background expectation is compatible with zero, a coarse estimate on systematic errors is given for the background also. Only the errors, which are different w.r.t. the signal or which are separately determined for background, are listed here. The list includes:

- **Theoretical background production cross sections and Fragmentation.**

In the ee and ej event classes, the bulk of the remaining background is due to High Q^2 NC as can be seen e.g. in Figures 4.16 and 4.17. While the production cross section for this background can be accurately calculated (to the percent level), the modelling of the fragmentation has an important impact on the P_T spectra of the individual particles inside a jet and therefore on the number of selected events in this analysis. The effect of the fragmentation was studied with two low statistics DJANGO MC samples, which differ only by the fragmentation model. One was done with the colour-dipole fragmentation (CDM) [60] and the other with the so-called MEPS (Matrix Element calculation and Parton Shower) [67]. The difference in the number of surviving events is roughly 15%.

In the jj event class the largest background contribution comes from di-jet photoproduction. The dependence of the cross section on the renormalisation and factorisation scales, on the pdf and the fragmentation and the description of so-called soft underlying events¹ was studied in [57]. An error of 20% is assumed here.

The $e\mu$ and μj event classes are practically background-free. The theory uncertainty of the dominant contribution after preselection is quoted for these classes, namely 15% for high Q^2 NC in $e\mu$ and 20% for γp in μj .

- **θ measurement.**

The only measurable effect is found in the ej class, where the difference is 3%. Other event classes suffer from very low background statistics.

- **Jet Isolation.**

The variations on R_{close} , R_{far} according to (5.1) produces shifts of 2.5% in ej and 10% in jj .

- **LAr electromagnetic energy scale.**

The variation of 3% leads to an effect of 3% in the ej class. In the ee class in $e\tau$ also an effect is expected, but the background statistics is too small in order to observe any deviation. The same holds for the jj class ($\tau\tau$).

- **LAr hadronic energy scale.**

A variation of 2% leads to an effect of 10% in jj , 6% in ej (18% in $e\tau$) and 1% in μj .

¹In resolved photoproduction additionally to the hard scattering process there may be interactions between the proton and the photon remnants. This is often referred to as soft underlying event.

| Effect | Variation | Event Classes | | | | |
|-----------------------|----------------|---------------|-------------|----------|-------------|----------|
| | | $e\mu$ [%] | ej [%] | ee [%] | μj [%] | jj [%] |
| Theory | - | 15 | 15 | 15 | 20 | 20 |
| HV, Lumi | - | 1.5 | 1.5 | 1.5 | 1.5 | 1.5 |
| Tracking | - | 6 | 6 | 6 | 6 | 6 |
| μ -ID | - | 6 | - | - | 6 | - |
| e-ID | - | 2 | 2 | 4 | - | - |
| Trigger | - | 0.5 | 0.5 | 0.5 | 5 | 5 |
| Track θ | 3 mrad | 0 | 3 | 0 | 0 | 0 |
| Jet Isolation | equation (5.1) | 0 | 2.5 | 0 | 0 | 10 |
| LAr e.m. scale | 3% | 0 | 3 | 0 | 0 | 0 |
| LAr had. scale | 5% | 0 | 6 (18) | 0 | 1 | 10 |
| $\sqrt{\Sigma err^2}$ | | 17.4 | 18.1 (24.8) | 16.7 | 22.4 | 25.8 |

Table 5.2: Same as Table 5.1 but for the background.

5.2 Efficiencies

From the number of surviving events in the signal MC a global efficiency is determined for each event class. This efficiency includes all detector acceptance effects and branching ratios from τ decay(s) and can therefore be viewed as a probability for observing a doubly charged Higgs signal event in a specific event class. MC samples were generated for Higgs masses between 80 and 150 GeV in steps of 10 GeV for all kinematic régimes (elastic, quasielastic and inelastic) and weighted according to their contribution to the total cross section (see section 1.7).

Figure 5.1 shows the efficiencies as a function of the Higgs mass for the different event classes for the $\tau\tau$ topology and the 99/00 conditions. For ej and jj the distinction is made between elastic and inelastic events as discussed in section 4.3. The efficiencies for the inelastic channels are however clearly inferior w.r.t. their elastic counterparts. The drawn line represents a polynomial (of order 2) fit to the sample points. The fit will be used in the limit calculation to compute efficiencies in steps of 1 GeV. The steep rise in the efficiencies at low Higgs masses ($80 \lesssim M_H \lesssim 100$ GeV) is mainly due to the more intense P_T spectrum of the candidate tracks for larger masses. The saturation or even fall of the efficiencies at large Higgs masses ($140 \lesssim M_H \lesssim 150$ GeV) is due to the acceptance in the forward region, since more massive particles are produced with harder boosts in the proton direction. For a Higgs mass of 100 GeV the total efficiency (sum over all channels) is 21.2%.

The procedure is repeated for the 96/97 dataset, where the efficiency distributions are similar. The ratios between the efficiencies for 96/97 and 99/00 are approximately independent of the Higgs mass, as can be seen in Figure 5.2. Furthermore a polynomial fit of order zero shows that the ratios are compatible with 1 within the errors except for the μj event class, where the difference can be explained by different muon trigger prescales in the two data taking periods.

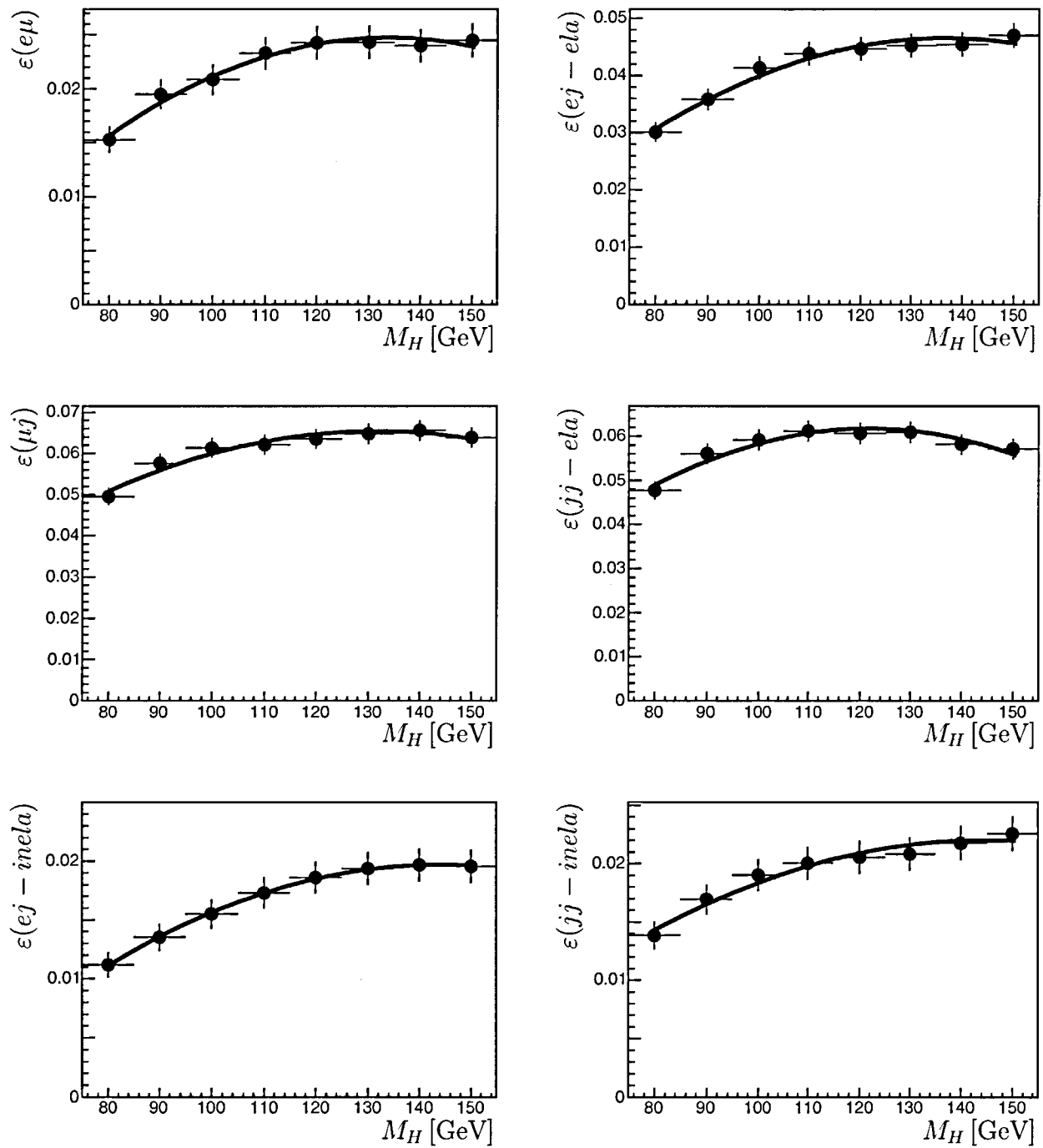


Figure 5.1: Final signal efficiencies as a function of the Higgs mass for $\tau\tau$ and the 99/00 conditions.

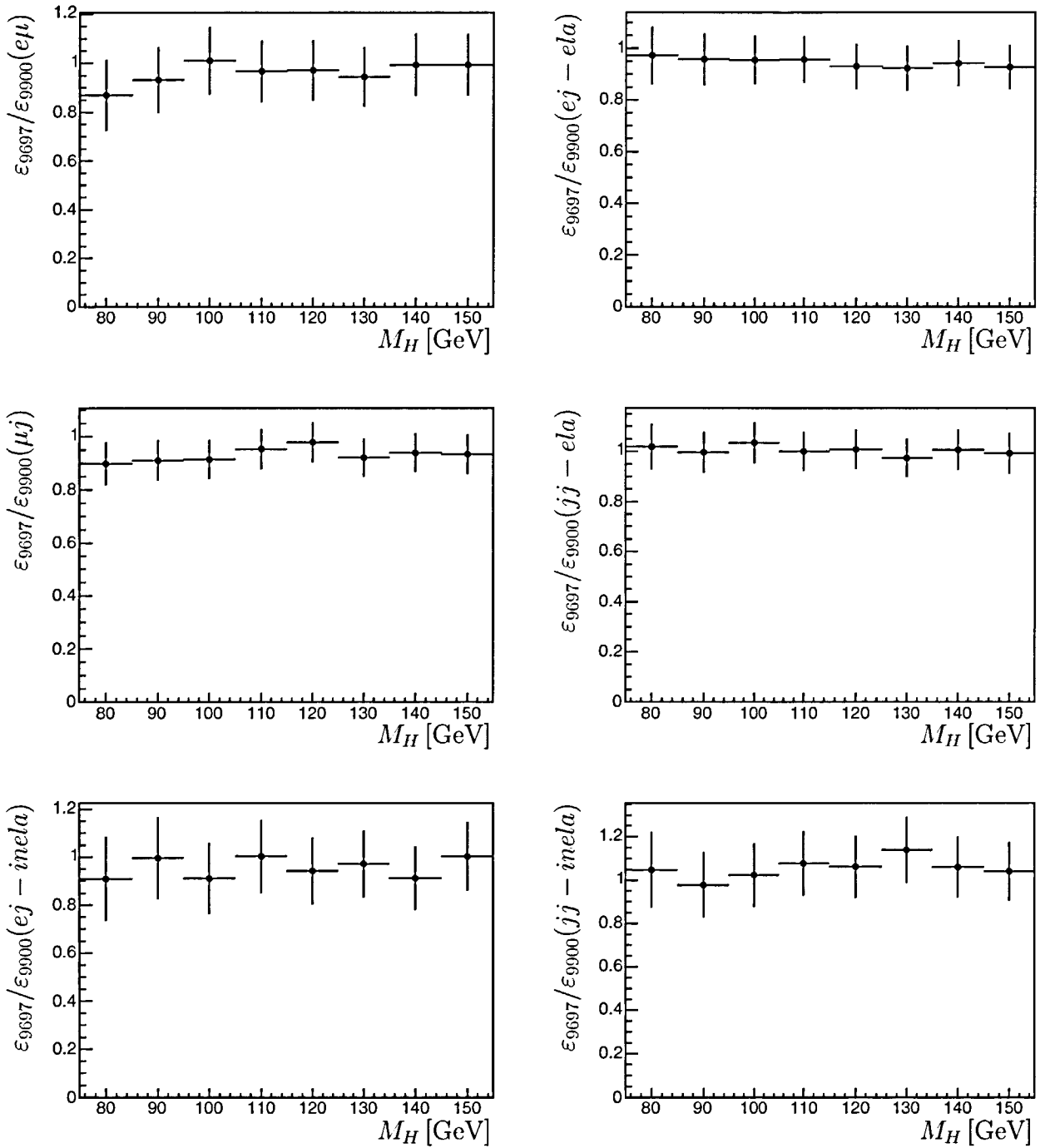


Figure 5.2: Efficiency ratios between the 96/97 and 99/00 datasets for the different event classes for $\tau\tau$ as a function of the Higgs mass.

The corresponding plots for the $e\tau$ topology are given in Figures 5.3 and 5.4. The total efficiency for a Higgs mass of 100 GeV is about 24.5% for $e\tau$ and therefore slightly higher than the corresponding $\tau\tau$ efficiency. The order zero polynomial fit shows that the efficiency ratios (see Figure 5.4) between the two datasets are compatible with 1, except for the ee event class, where the discrepancy is due to the requirement on the start radius of the electron track ($R_S < 30$ cm as discussed in section 3.5.1). It is known [68] that in 1997 the CJC1 had a region with reduced sensitivity.

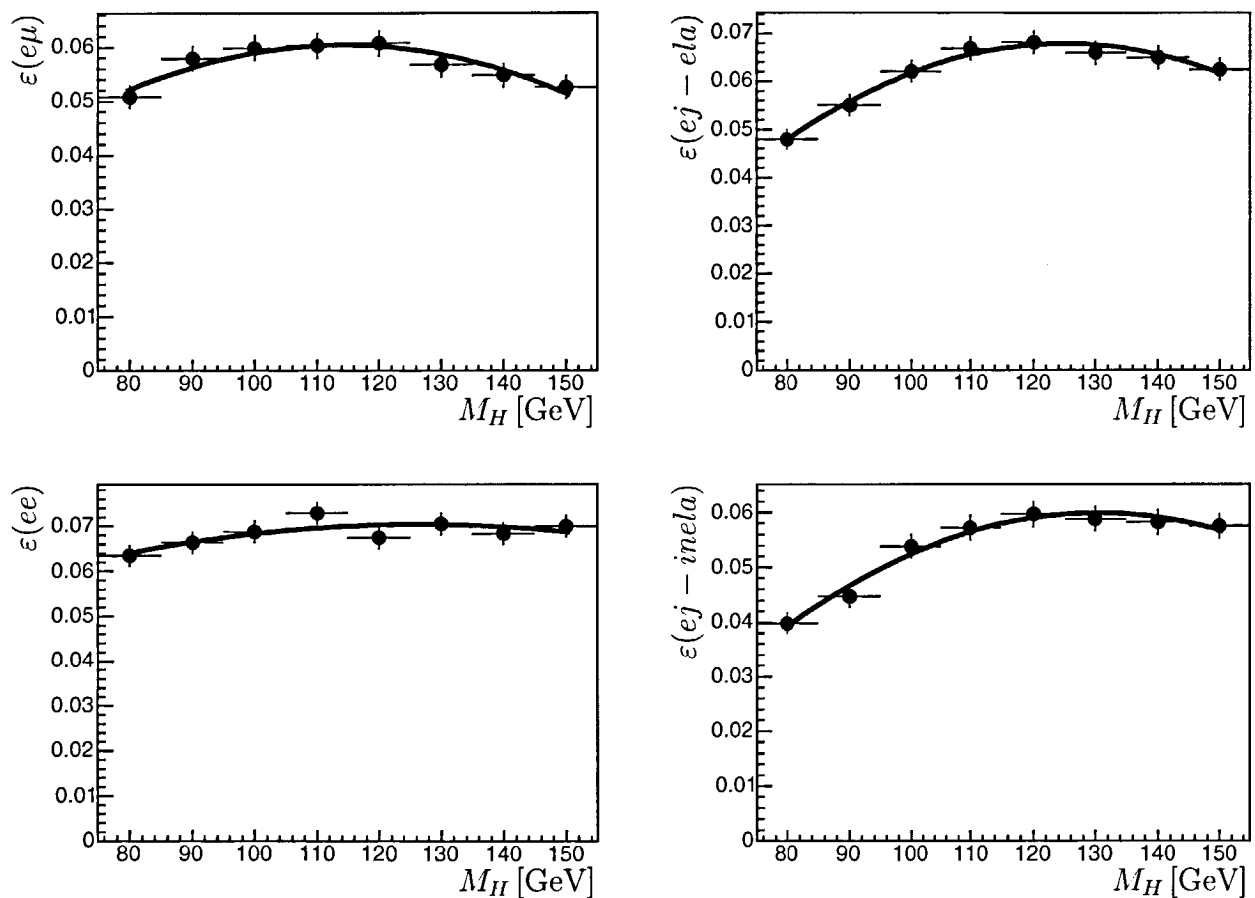
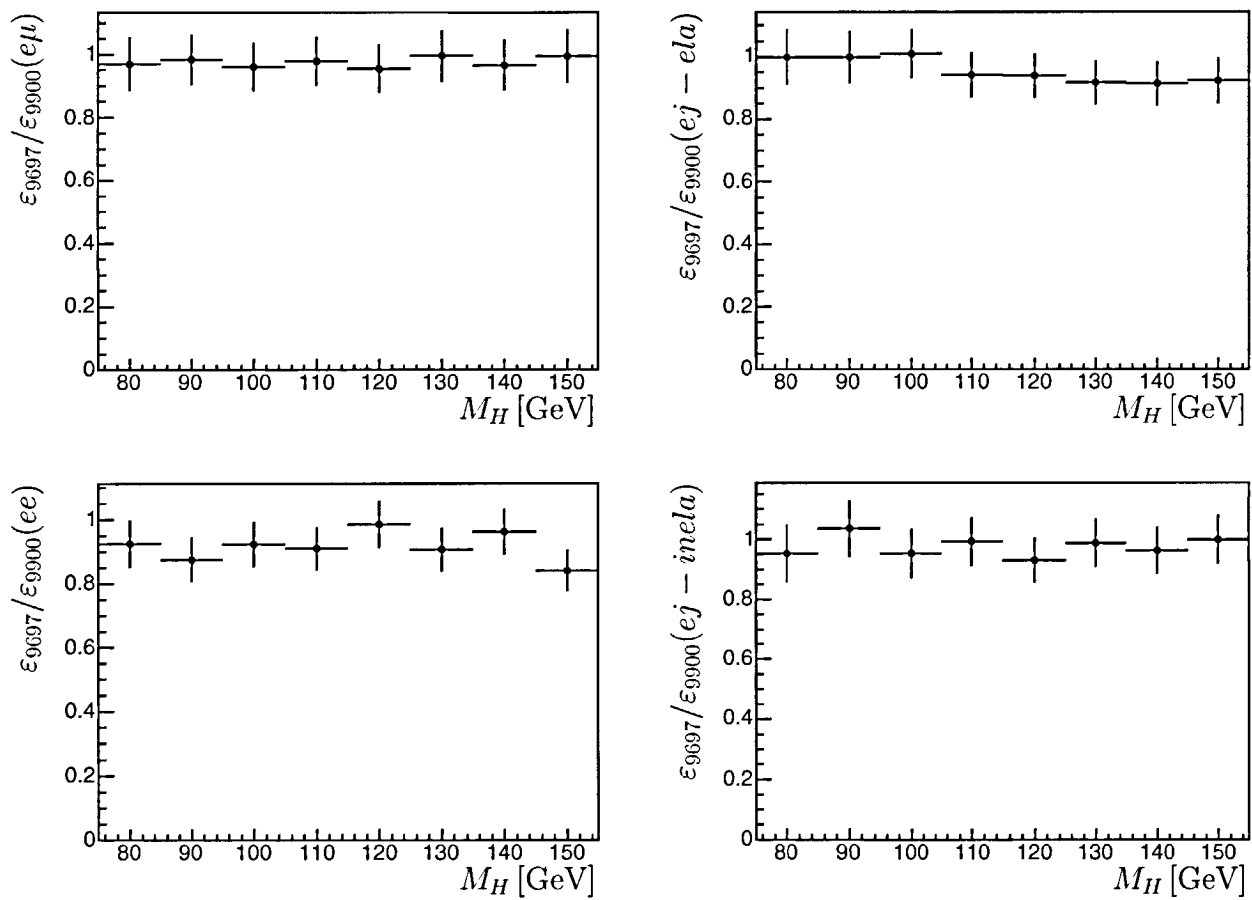


Figure 5.3: Same as Figure 5.1 but for $e\tau$.

Figure 5.4: Same as Figure 5.2 but for $e\tau$.

5.3 Limit Calculation

In the absence of signal, the interpretation of the results focuses on the task of setting upper exclusion limits for doubly charged Higgs production. For low statistics analyses usually confidence intervals are calculated with a test statistic X in the form of a Poisson Likelihood ratio [9]:

$$X = \frac{e^{-(s+b)}(s+b)^N}{N!} \bigg/ \frac{e^{-b}b^N}{N!} \quad (5.2)$$

N is the number of observed data events, b and s are the number of expected background, and signal events respectively. The test statistic X is monotonically increasing with N . The confidences in the signal+background (CL_{s+b}) and the background only (CL_b) hypothesis are then defined as:

$$\begin{aligned} CL_{s+b} &= P_{s+b}(X \leq X_{obs}) \\ CL_b &= P_b(X \leq X_{obs}) \\ CL_s &= CL_{s+b}/CL_b. \end{aligned} \quad (5.3)$$

CL_s is then the confidence in the presence of signal. P_{s+b} (P_b) is the probability to find a specific outcome X_{obs} under a signal+background (background only) hypothesis. Since the test statistic X is defined as the probability ratio of the two hypothesis for finding exactly N events in data, these two probabilities are simply:

$$P_{s+b}(X \leq X_{obs}) = \sum_{n=0}^N \frac{e^{-(s+b)}(s+b)^n}{n!} \quad \text{and} \quad P_b(X \leq X_{obs}) = \sum_{n=0}^N \frac{e^{-b}b^n}{n!}. \quad (5.4)$$

The confidence level $CL = 1 - CL_s$ is then used to set limits on the signal expectation s . For instance a limit at a CL of 95% as will be derived for this analysis corresponds to $CL_s = 5\%$. In mathematical form this reads:

$$1 - CL = \left(\sum_{n=0}^N \frac{e^{-(s+b)}(s+b)^n}{n!} \right) \bigg/ \left(\sum_{n=0}^N \frac{e^{-b}b^n}{n!} \right). \quad (5.5)$$

The ratio to the right of equation (5.5) is just the Poisson probability of observing N (or less) events under a signal + background hypothesis divided by the Poisson probability for observing N (or less) events under a background only hypothesis.

For a given confidence level, an upper limit can then be calculated by numerically solving (5.5) for s with the use of the experimentally measured input (N) and the input from the background MC (b). The outcome s_{CL} is the number of expected signal events, which can be excluded at the given CL .

The simple method outlined above can in principle be used to calculate limits for all the different event classes (which can be regarded as independent search channels) in the

present analysis, but in order to produce a combined limit of all event classes a more sophisticated technique is required.

5.3.1 Multiple Search Channels

The approach chosen here is described in detail in [69, 70] and was used extensively for the various Higgs searches at the OPAL experiment. The test statistic X for the multi-channel search is the product of the test statistics X_i for the individual channels. Each channel i has a number of data candidates n_i and the computation of CL_{s+b} requires building the sum over all probabilities

$$P_{s+b}(\{n_i\}) = \prod_{i=1}^N \frac{e^{-(s_i+b_i)}(s_i+b_i)^{n_i}}{n_i!} \quad (5.6)$$

for which $X(\{n_i\}) \leq X_{obs}$ holds for the outcome $\{n_i\}$. The same procedure is required for the computation of CL_b with the probability $P_b(\{n_i\})$. As the number of search channels N grows large, the combinatorics grows exponentially with N and thus making the calculation of the confidence levels difficult. The solution outlined in [69, 70] consists in combining two channels at a time and keeping only a representative number of possible outcomes for the further combination process.

The software used to derive the 95% CL limits for multiple search channels is included in the reference. In its basic usage it requires n_i , b_i and initial values for s_i^{init} as input. From that it calculates a scale factor f to be applied on the initial value $\sum s_i^{init}$, which then yields the number of expected signal events s_{95} that can be excluded at 95% CL. In this analysis the efficiencies in the individual search channels are used as initial values for the number of expected signal events: $s_i^{init} = \varepsilon_i$. This has the advantage that from the resulting scale factor the limit on the cross section σ_{95} can be most easily derived:

$$\sigma_{95} = \frac{s_{95}}{(\sum_i \varepsilon_i) \mathcal{L}} = \frac{f \cdot (\sum_i \varepsilon_i)}{(\sum_i \varepsilon_i) \mathcal{L}} = \frac{f}{\mathcal{L}} \quad (5.7)$$

where \mathcal{L} denotes the data luminosity.

In order to produce a limit in steps of 1 GeV in the hypothetical Higgs mass, all event classes are divided into 91 channels, each channel corresponding to one bin of width 1 GeV in the reconstructed mass histogram (mass range $69.5 \leq M_{rec} \leq 160.5$ GeV) of that event class. Since all events in data and background end up in exactly one bin of the reconstructed mass, these bins can be regarded as independent search channels. For $\tau\tau$ with 6 different event classes the number of search channels for the combined limit is then $N = 6 \cdot 91 = 546$ and for $e\tau$ (4 event classes) $N = 364$.

Efficiencies ε_i in the different search channels

The total efficiency for any event class (see section 5.2) is distributed among the 91 channels (mass bins) according to the mass resolution of the signal for the considered Higgs mass. This is illustrated in Figure 5.5 for a hypothetical Higgs mass of 100 GeV. Assuming that a data candidate is found e.g. at $M = 90$ GeV, this candidate will have only a very small influence on the limit calculated for a 100 GeV Higgs, because the efficiency (probability) to reconstruct a signal event at 90 GeV while the true Higgs mass is 100 GeV is very small. If however a candidate is found near 100 GeV it will have a large signal-significance and will therefore push the limit upwards. Thus, by varying the hypothetical Higgs mass in the range $80 \leq M_H \leq 150$ GeV one expects to see “bumps” in the limit at masses where the data candidates are. The width of these “bumps” will correspond to the mass resolution at the candidate’s mass.

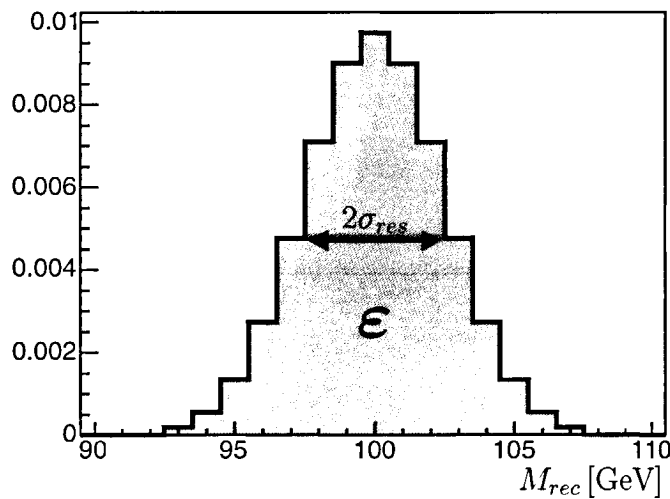


Figure 5.5: The efficiencies ε_i (corresponding to the individual bins in the Figure) passed to the limit calculation program for a hypothetical Higgs mass of 100 GeV. The surface under the Gaussian distribution is the total efficiency $\varepsilon = \sum \varepsilon_i$ in the considered event class. The width of the Gaussian is equal to the mass resolution σ_{res} at 100 GeV as determined in Figures 4.11 and 4.12.

In order to increase the numerical stability of the limit calculation program the Gaussian efficiency distributions as seen in Figure 5.5 are cut off at $\pm 3\sigma$. All channels i , which are outside of the $\pm 3\sigma$ -band around the hypothetical Higgs mass, are assigned an efficiency $\varepsilon_i = 0$ and are not passed to the limit calculation at all.

Background b_i in the different search channels

As the analysis deals with very little background, and the statistics in the background MCs is not sufficient to produce a meaningful shape in the reconstructed mass histogram, the background expectation in each event class is just summed up and distributed equally among all mass bins (channels) in that event class:

$$\langle b_i \rangle = \frac{1}{91} \sum_{i=1}^{91} b_i \quad (5.8)$$

where 91 is the number of channels per event class. This improves the numerical stability in the subsequent limit calculation without having an influence on the shape of the obtained limit.

5.3.2 Treatment of Systematic Uncertainties

The efficiencies ε_i and background expectations b_i for each channel are subject to systematic errors as estimated in section 5.1. This is taken into account in the implementation of the limit calculation in reference [69, 70] by smearing the probabilities and test statistics for all search channels by their systematic uncertainty probability distributions, which are assumed Gaussian. For instance the probability to observe j events in channel i under the signal+background hypothesis with an expected number of signal events $s_i \pm \sigma_{s_i}$ and an expected number of background events $b_i \pm \sigma_{b_i}$ is:

$$p_i^j = \frac{\int ds' \int db' \frac{e^{-((s'-s_i)^2/2\sigma_{s_i}^2 + (b'-b_i)^2/2\sigma_{b_i}^2)} \cdot e^{-(s'+b')(s'+b')^j}}{2\pi\sigma_{s_i}\sigma_{b_i}} \cdot j!}{\int ds' \int db' \frac{e^{-((s'-s_i)^2/2\sigma_{s_i}^2 + (b'-b_i)^2/2\sigma_{b_i}^2)}}{2\pi\sigma_{s_i}\sigma_{b_i}}} \quad (5.9)$$

The shortcoming of this implementation is that correlated systematic errors between different search channels are not correctly treated. In section 5.1 the systematic errors were estimated for different event classes. However, there are errors, such as e.g. on the luminosity, which are correlated among all event classes. Also the splitting of one event class into 91 search channels (mass bins) will produce 100% correlated errors for these search channels. A correct treatment of correlated uncertainties would require to average the probabilities and test statistics simultaneously and only once for all search channels, which are affected by the error in question. However, it is noted that treating all uncertainties for all search channels as independent means that errors are double counted and the resulting limit is therefore conservative. Also, all limits have been produced under the assumption $\sigma_{s_i} = \sigma_{b_i} = 0$ for all channels. The change in the observed limit with respect to the case where all systematic errors are taken into account as described above is $< 1\%$.

5.3.3 Limits for individual Event Classes

With the procedure outlined in the previous sections, limits at 95% CL on

- $\sigma(ep \rightarrow H^{++}) \times BR(H^{++} \rightarrow \tau\tau)$ for the $\tau\tau$ topology, and
- $\sigma(ep \rightarrow H^{++}) \times BR(H^{++} \rightarrow e\tau)$ for the $e\tau$ topology

are calculated for Higgs masses in the range $80 \leq M_H \leq 150$ GeV. Although not as interesting as the combined limits (see next section), the limits for the individual event classes are presented here. In Figure 5.6 (5.7) the limits for the $\tau\tau$ ($e\tau$) topology are shown. Only the inelastic ej class has data candidates left. These show up as “bumps” in the limits at their reconstructed masses. See also the appendix for a list of the data candidates.

5.3.4 Combined Limits

The combination of the different event classes and datasets is straightforward as it only requires to use all available search channels together for the limit calculation. The limits on cross section \times branching ratio are given in Figures 5.8 and 5.9. In these plots also a *mean expected limit* is drawn (dashed line), which represents the limit one would expect to obtain if the background-only hypothesis was true. It can be calculated by doing many MC experiments, where the number of data events is randomly generated according to a Poisson probability with a mean number of events equal to the background expectation b . The $\pm 2\sigma$ error band of this expected limit is also drawn (shaded region). The -2σ boundary of this error band almost coincides with the expected limit for almost all plots. This is because an observed limit smaller than the expected limit would correspond to a downward fluctuation of the number of data events with respect to the expected background. Since most event classes are almost background free already, a downward fluctuation almost cannot occur in these classes. Only in the $e\tau$ topology the observed limit exceeds the $+2\sigma$ boundary at 92 GeV. In the combination of the datasets however the observed limit is everywhere well contained inside the error band.

For the $e\tau$ topology an additional limit on the coupling $h_{e\tau}$ is calculated under the assumption that $BR(H^{++} \rightarrow e\tau) = 100\%$. Since the Higgs production cross section is proportional to $h_{e\tau}^2$, the limit on the coupling can be calculated in that case from the cross section limit as:

$$h_{e\tau}^{95} = h_{e\tau}^{gen} \cdot \sqrt{\frac{\sigma_{95}}{\sigma_{gen}}}. \quad (5.10)$$

$h_{e\tau}^{gen}$ is the coupling, for which the MC samples were generated and for which the calculated cross section was σ_{gen} . The resulting limit for $e\tau$ is displayed in Figure 5.10. For $\tau\tau$ the same limit can not be calculated because for the assumption $BR(H^{++} \rightarrow \tau\tau) = 100\%$ the Higgs can not be produced in the first place, since that would require $h_{ee} \neq 0$. Instead for $\tau\tau$ the democratic assumption $h_{ee} = h_{\mu\mu} = h_{\tau\tau}$ or equivalently $BR(H^{++} \rightarrow ee/\mu\mu/\tau\tau) = 33\%$ is made and the corresponding coupling limit is shown in Figure 5.11.

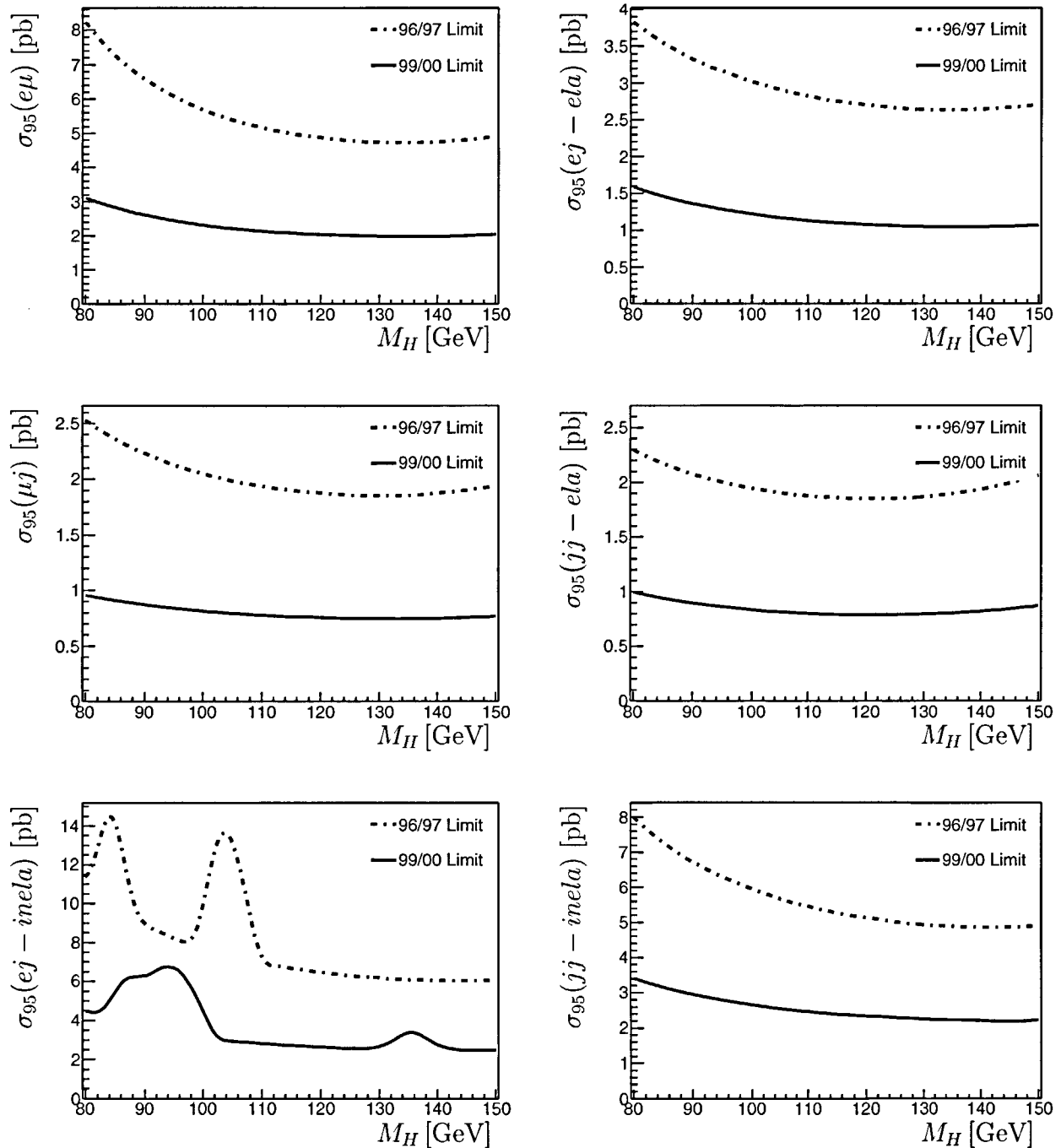


Figure 5.6: 95% CL limits on $\sigma(ep \rightarrow H^{++}) \times BR(H^{++} \rightarrow \tau\tau)$ for individual event classes for both data sets. The region above the limits is excluded. The strictest limits are derived in the μj and the elastic $j j$ event class.

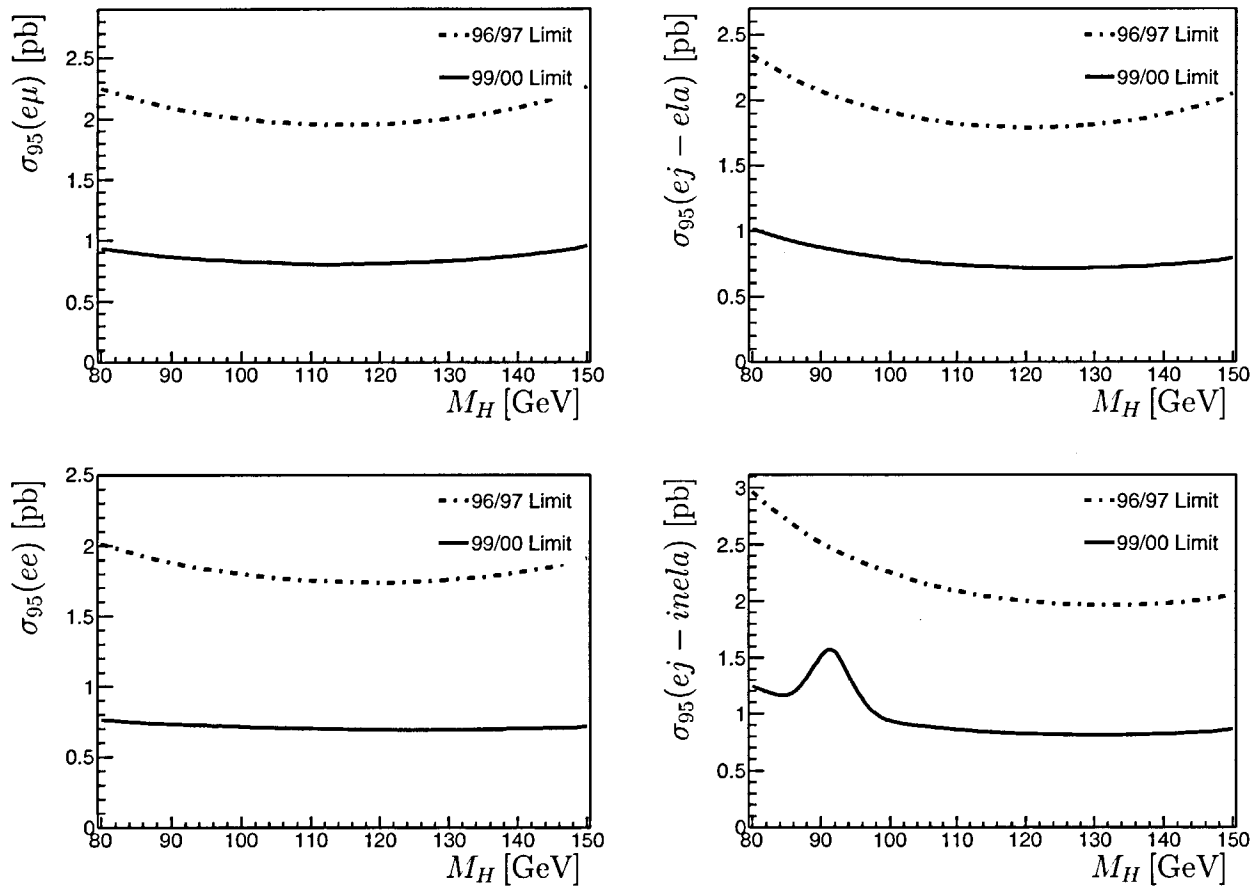


Figure 5.7: 95% CL limits on $\sigma(ep \rightarrow H^{++}) \times BR(H^{++} \rightarrow e\tau)$ for individual event classes for both data sets. The strictest limits are derived in the ee event class. However, the limits for the different event classes are more similar than for $\tau\tau$, where especially the inelastic channels are much less sensitive than the elastic ones.

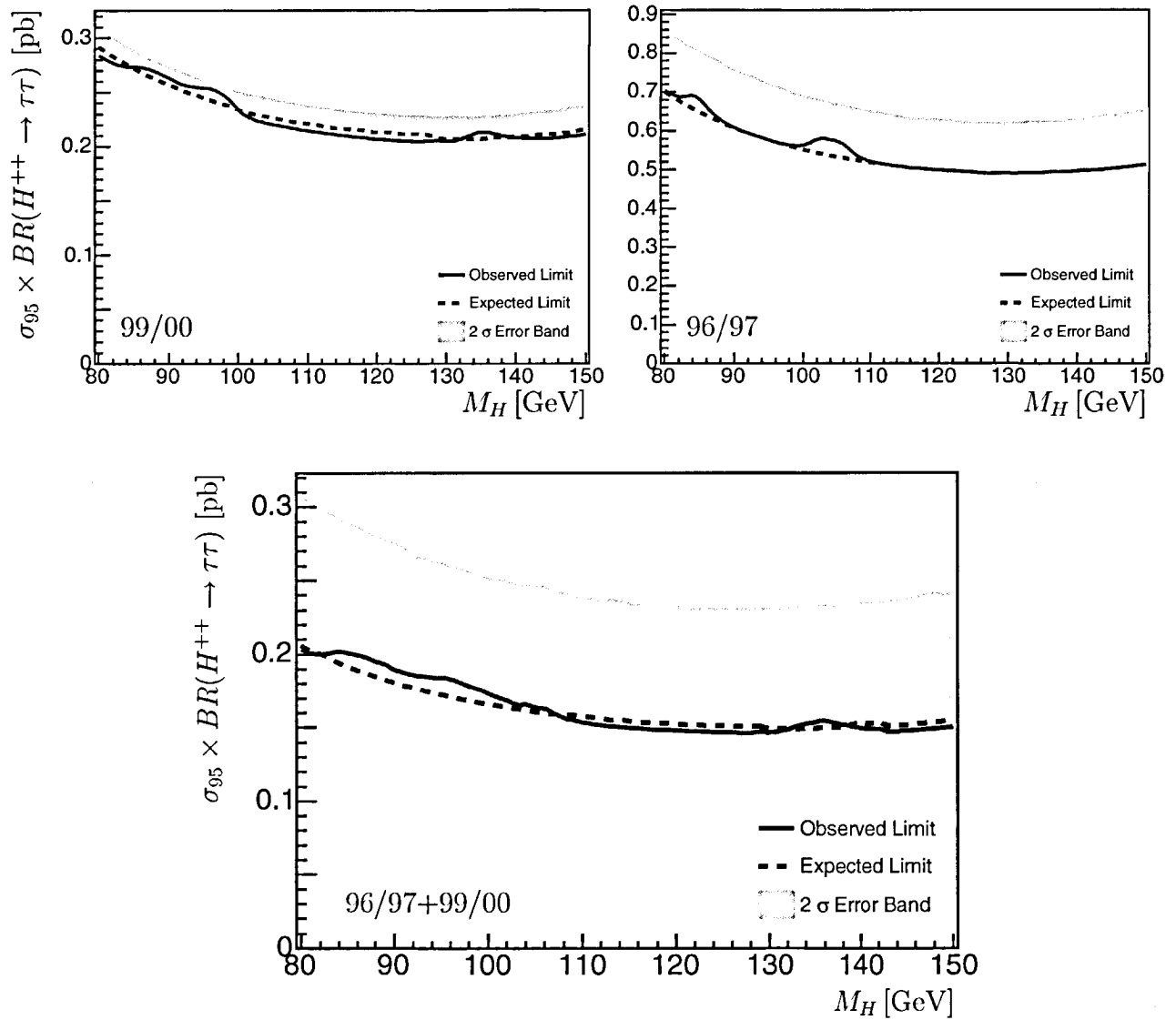


Figure 5.8: Combined 95% CL limits on $\sigma(ep \rightarrow H^{++}) \times BR(H^{++} \rightarrow \tau\tau)$ for the individual datasets (top) and for the combination of both datasets (bottom). Also shown is the expected limit and its $\pm 2\sigma$ fluctuation band. The observed limit is everywhere contained inside the error band.

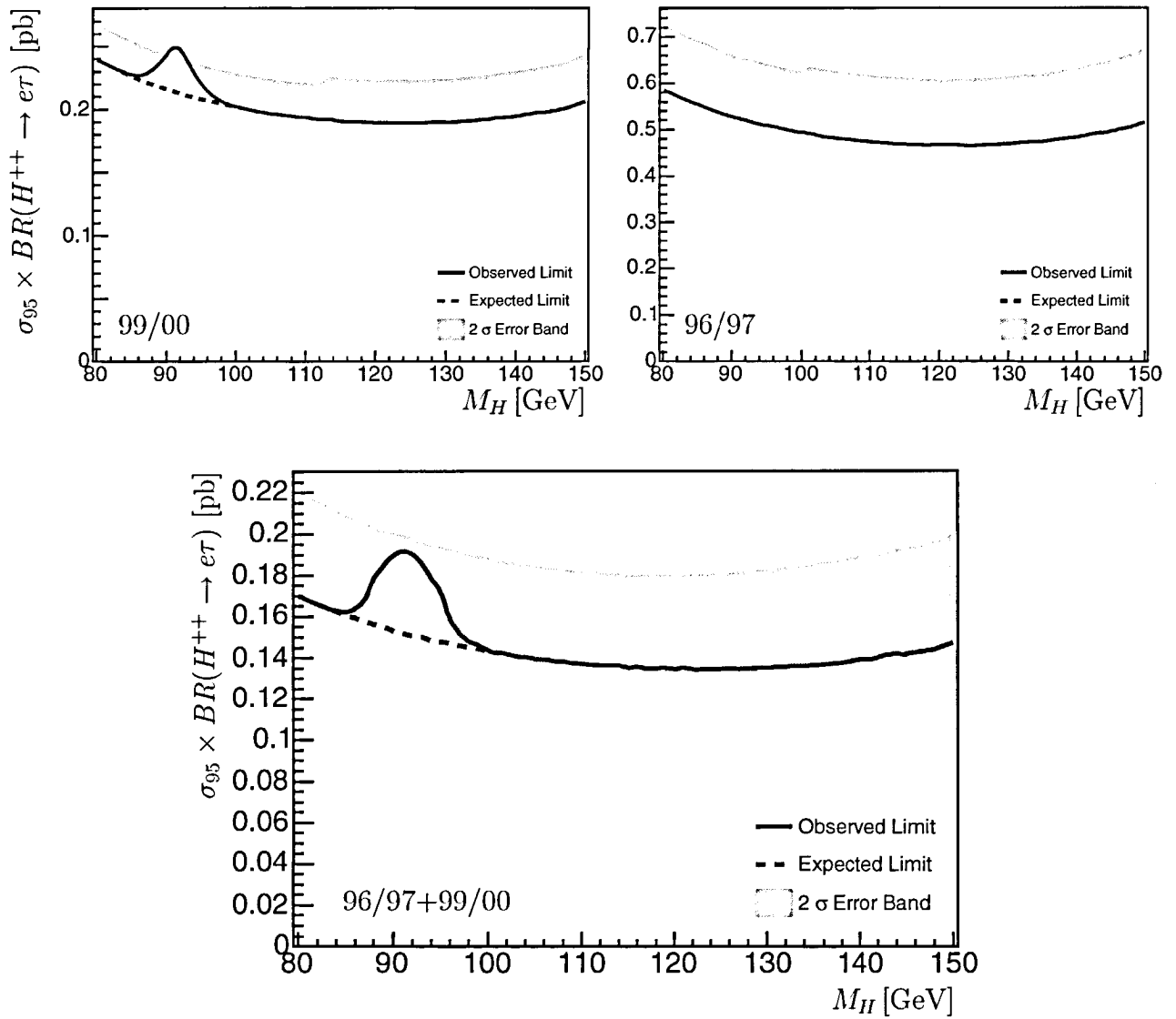


Figure 5.9: Combined 95% CL limits on $\sigma(ep \rightarrow H^{++}) \times BR(H^{++} \rightarrow e\tau)$ for the individual datasets (top) and for the combination of both datasets (bottom). The observed limit exceeds the 2σ error band of the expected limit only at 92 GeV and only for the 99/00 dataset. In the combination of both datasets (bottom) the limit is contained inside the error band.

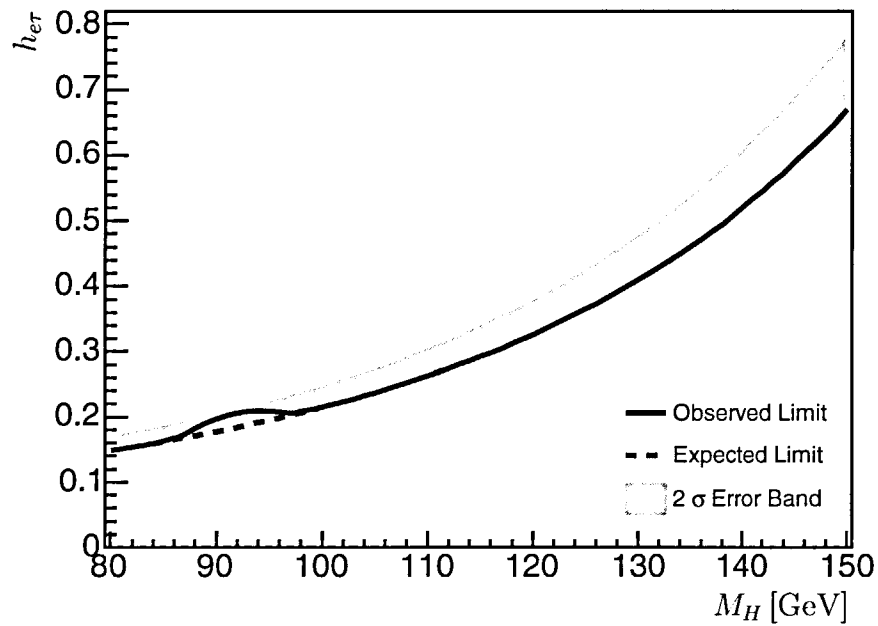


Figure 5.10: 95% CL limit on the coupling $h_{e\tau}$ including both datasets and all event classes. The assumption $BR(H^{++} \rightarrow e\tau) = 100\%$ is made in this plot.

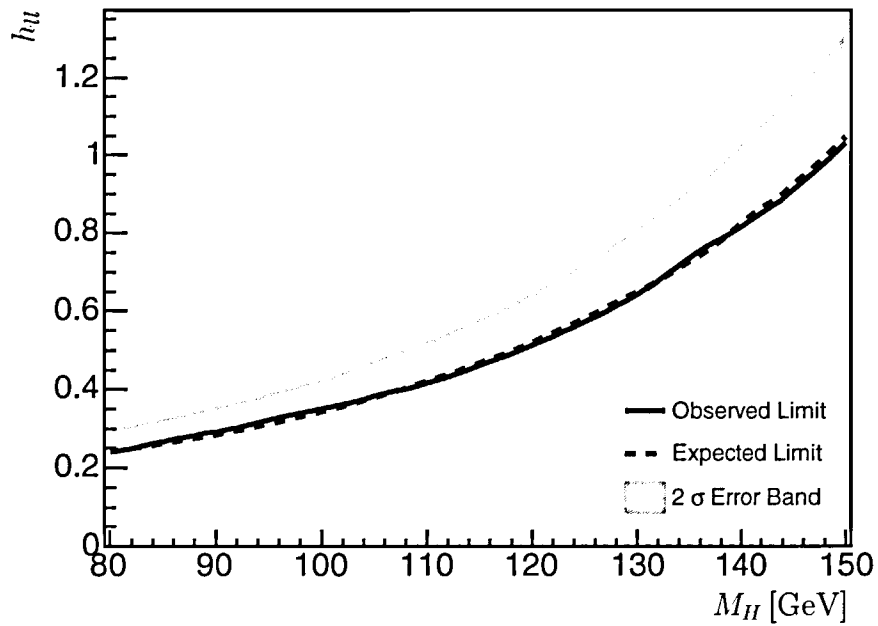


Figure 5.11: 95% CL limit on the diagonal coupling $h_{\mu\mu}$ as determined from the $\tau\tau$ selection. The democratic assumption $BR(H^{++} \rightarrow ee/\mu\mu/\tau\tau) = 33\%$ is made in this plot.

Seite Leer /
Blank leaf

Chapter 6

Conclusion

In this thesis a search for the doubly charged Higgs particle and its subsequent decay into $\tau\tau$ and $e\tau$ final states in the HERA I dataset is performed. The analysis is based on high transverse momentum tracks measured in the central H1 tracking chamber. The final state invariant mass is fully reconstructed by applying momentum balance constraints on the candidate events. The missing neutrino momenta originating from τ decays are thereby approximated. From the MC simulation of potential H^{++} decays, a mass resolution of $\sigma^{res} \lesssim 4 \text{ GeV}$ is derived. Simple τ identification techniques are used in this analysis, since the doubly charged Higgs topology can be well separated from background by simple kinematic and jet isolation criteria. In order to suppress background from di-lepton production, two like-sign charged tracks are required.

Throughout the entire selection process an agreement between data and the SM expectation is found or in other words: No evidence for a doubly charged Higgs signal in the investigated search channels is observed. Upper limits at 95% confidence level on $\sigma(ep \rightarrow H^{++}) \times BR(H^{++} \rightarrow \tau\tau)$ and $\sigma(ep \rightarrow H^{++}) \times BR(H^{++} \rightarrow e\tau)$ are calculated as a function of the Higgs mass in the range $80 \leq M_H \leq 150 \text{ GeV}$. In this mass range the limits are found to be:

- $\sigma(ep \rightarrow H^{++}) \times BR(H^{++} \rightarrow \tau\tau) \lesssim 0.2 \text{ pb}$
- $\sigma(ep \rightarrow H^{++}) \times BR(H^{++} \rightarrow e\tau) \lesssim 0.2 \text{ pb}$.

These cross section times branching ratio limits can be directly compared to results from the other H1 analyses [3] as shown in Figure 6.1. The τ topologies yield less stringent limits mostly for the lower Higgs masses. The reason is the loss in signal efficiency due to the conditions on the transverse momentum (P_T) on the secondary τ decay tracks, which have a smaller P_T than primary particles (i.e. electrons or muons) from the Higgs decay. This difference is reduced towards higher Higgs masses.

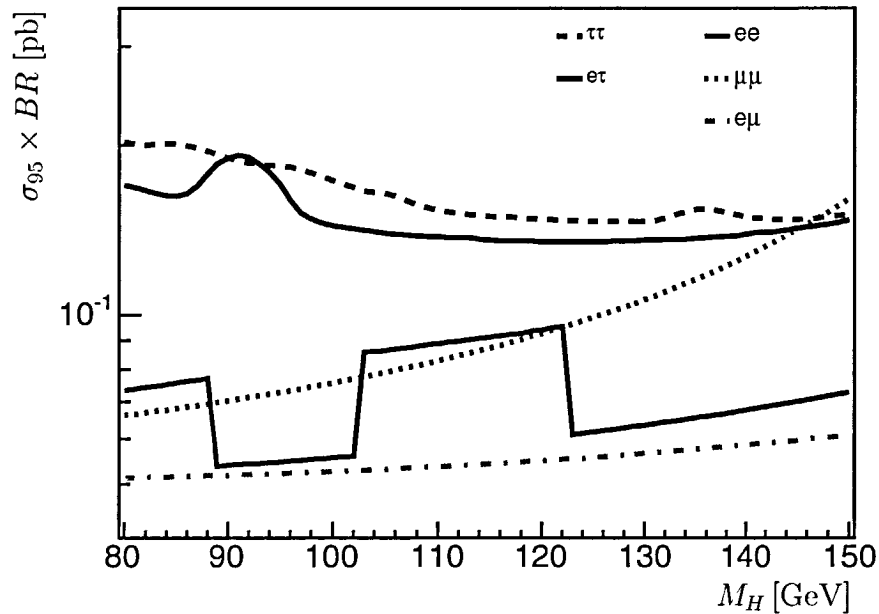


Figure 6.1: 95% CL limits on cross section times branching ratio for all investigated doubly charged Higgs decay topologies at H1. The uppermost two curves are the results of the present thesis. The ee , $e\mu$ and $\mu\mu$ limits can be found in [3].

In comparison with other experiments, some of the limits derived at H1 are not yet competitive. The CDF limits [29] exclude the existence of left-handed doubly charged Higgs $H_L^{\pm\pm}$ below masses of about 130 GeV for the ee and $\mu\mu$ channels and right-handed $H_R^{\pm\pm}$ below masses of about 110 GeV. The OPAL limits [24] are difficult to compare to the H1 limits because in their analysis the Higgs is always produced via the coupling h_{ee} and all Higgs decay topologies are used to set limits on h_{ee} under the assumption $h_{ee} \ll h_{ll'}$ where l, l' stands for the lepton pair of the considered decay topology. For the decay $H^{\pm\pm} \rightarrow ee$ the OPAL limit is however clearly more constraining than the corresponding H1 limit. The H1 limits on the flavour violating couplings $h_{e\mu}$ and $h_{e\tau}$ (this analysis) on the other hand are unique. However, the LEP experiments are expected to have higher sensitivities for these couplings than H1.

As the present analysis is only statistically limited, the increased luminosity of the HERA II running period¹ will gain about a factor of 10 in sensitivity for the H1 search for doubly charged Higgs bosons. Under the assumption that no deviation from the SM is found in the new data, all cross section limits can be expected to improve by a factor of 10 and the coupling limits by a factor of $\sqrt{10}$.

¹Design luminosity for the HERA II data taking period is 1 fb^{-1} .

List of Figures

| | | |
|------|--|----|
| 1.1 | Higgs Potential for a single complex scalar field | 7 |
| 1.2 | Feynman diagrams for tree level H^{++} production at HERA via the Yukawa process | 14 |
| 1.3 | Feynman diagrams for H^{++} production and decay | 14 |
| 1.4 | Feynman diagrams for $H^{\pm\pm}$ pair production and Bhabha scattering via doubly charged Higgs exchange at LEP | 15 |
| 1.5 | Feynman diagrams for $H^{\pm\pm}$ pair production and single production via W -fusion at Tevatron and LHC | 16 |
| 1.6 | Higgs production cross sections for a coupling constant $h_{ee} = h_{\tau\tau} = 0.3$. . . | 18 |
| 1.7 | Higgs production cross sections for a coupling constant $h_{e\tau} = 0.3$ | 19 |
| 2.1 | The HERA and PETRA accelerator rings at DESY | 21 |
| 2.2 | View of the H1 detector and the definition of the coordinate system. | 23 |
| 2.3 | Side view of the H1 tracking system | 24 |
| 2.4 | Side view of the upper half of the liquid argon calorimeter | 25 |
| 2.5 | Schematic of the different trigger levels | 27 |
| 2.6 | The H1 Luminosity System | 28 |
| 3.1 | P_T and η spectra of the Higgs decay particles. | 34 |
| 3.2 | P_T of the faster versus P_T of the slower candidate track for a Higgs signal of 100 GeV. | 36 |
| 3.3 | Generator level P_T and η spectra of the pseudoscattered lepton. | 37 |
| 3.4 | Distance in $\eta\phi$ between the two candidates. | 38 |
| 3.5 | Number of signal events rejected by the background finders in the signal. . | 39 |
| 3.6 | $\sum \theta$ of the candidates for a $\tau\tau$ signal MC of a 100 GeV Higgs. | 39 |
| 3.7 | Electron energy for the event classes $e\mu$ and ej | 43 |
| 3.8 | P_T^{hfs} (left) and γ^{hfs} (right) for the μj class for a 100 GeV Higgs | 44 |
| 3.9 | The signal efficiency of single events distribution for the μj event class. . . | 45 |
| 3.10 | The signal efficiency distribution for the jj event class. | 46 |
| 3.11 | \hat{p}_T distribution after preselection for a PYTHIA61 MC sample. | 47 |
| 3.12 | Number of Muons for data, background MC and signal. | 48 |
| 3.13 | Scattering angle γ_{hfs} of the hadronic final state and θ of the jet. | 49 |
| 3.14 | Track types for the jet candidates. | 50 |

| | | |
|------|---|----|
| 3.15 | Scattering angle γ_{hfs} of the hadronic final state and θ of the jet after the soft isolation cut. | 51 |
| 3.16 | Ratio of transverse energy over transverse momentum for muons in the MC | 52 |
| 3.17 | E_T/P_T for jet candidates in data and MC. | 53 |
| 3.18 | Number of surviving events after preselection. | 53 |
| 3.19 | P_T^{Miss} distributions for the ej and jj event classes. | 54 |
| 4.1 | $E - p_z$ distributions for the ej and jj event classes. | 56 |
| 4.2 | P_T^{Miss} distributions for the ej event class. | 57 |
| 4.3 | $E - p_z$ and P_T^{Miss} distributions for the ej event class for signal. | 58 |
| 4.4 | P_T^{Miss} versus $E - p_z$ for background and an $e\tau$ signal. | 60 |
| 4.5 | $E - p_z$ and P_T^{Miss} distributions for the ee event class. | 60 |
| 4.6 | θ_e for the ej and $e\mu$ event classes. | 61 |
| 4.7 | $\eta\phi$ -Distance between τ -jet candidates and their closest track. | 63 |
| 4.8 | Jet isolation variables R_{close} and R_{far} | 65 |
| 4.9 | An event display of a typical NC background event. | 66 |
| 4.10 | η_{max} distributions for signal and data/background. | 68 |
| 4.11 | Reconstructed $\tau\tau$ masses and mass resolutions. | 70 |
| 4.12 | Reconstructed $e\tau$ masses and mass resolutions. | 71 |
| 4.13 | Reconstructed Mass distributions for data and background in $\tau\tau$ | 72 |
| 4.14 | Reconstructed Mass distributions for data and background in $e\tau$ | 73 |
| 4.15 | Sum of the charges for a 100 GeV Higgs signal in the ej class for $\tau\tau$ and $e\tau$ | 74 |
| 4.16 | Sum of the charges of the candidates for data/background in $\tau\tau$ | 75 |
| 4.17 | Sum of the charges of the candidates for data/background in $e\tau$ | 76 |
| 4.18 | Reconstructed Mass distributions for data and background for ej after all cuts. | 80 |
| 5.1 | Final signal efficiencies as a function of the Higgs mass for $\tau\tau$ and the 99/00 conditions | 86 |
| 5.2 | Efficiency ratios between the 96/97 and 99/00 datasets for the different event classes for $\tau\tau$ as a function of the Higgs mass | 87 |
| 5.3 | Same as Figure 5.1 but for $e\tau$ | 88 |
| 5.4 | Same as Figure 5.2 but for $e\tau$ | 89 |
| 5.5 | The efficiencies ε_i passed to the limit calculation program for a hypothetical Higgs mass of 100 GeV. | 92 |
| 5.6 | 95% CL limits on $\sigma(ep \rightarrow H^{++}) \times BR(H^{++} \rightarrow \tau\tau)$ for individual event classes. | 95 |
| 5.7 | 95% CL limits on $\sigma(ep \rightarrow H^{++}) \times BR(H^{++} \rightarrow e\tau)$ for individual event classes. | 96 |
| 5.8 | Combined 95% CL limits on $\sigma(ep \rightarrow H^{++}) \times BR(H^{++} \rightarrow \tau\tau)$ | 97 |
| 5.9 | Combined 95% CL limits on $\sigma(ep \rightarrow H^{++}) \times BR(H^{++} \rightarrow e\tau)$ | 98 |
| 5.10 | 95% CL limit on the coupling $h_{e\tau}$ under the assumption $BR(H^{++} \rightarrow e\tau) = 100\%$ | 99 |
| 5.11 | 95% CL limit on the diagonal coupling h_{ll} under the assumption $BR(H^{++} \rightarrow ee/\mu\mu/\tau\tau) = 33\%$ | 99 |

6.1 95% CL limits on cross section times branching ratio for all investigated doubly charged Higgs decay topologies at H1. 102

Seite Leer /
Blank leaf

List of Tables

| | | |
|-----|--|----|
| 1.1 | Properties of the fermions in the Standard Model | 4 |
| 1.2 | Interactions in the standard model | 4 |
| 1.3 | Relative contributions to the total Higgs production cross section of the different kinematic régimes for the couplings h_{ee} and $h_{e\tau}$ | 17 |
| 2.1 | CJC geometry | 25 |
| 3.1 | Properties of the different data sets used | 32 |
| 3.2 | Summary: non- ep physics suppression | 40 |
| 3.3 | τ decay modes and branching ratios. | 40 |
| 3.4 | Branching ratios of the different event classes for $\tau\tau$ and $e\tau$ | 40 |
| 3.5 | Subtriggers used in the analysis. | 42 |
| 3.6 | Set of background MC samples. | 47 |
| 3.7 | Number of surviving events after preselection. | 53 |
| 4.1 | Optimal $E - p_z$ and P_T^{Miss} cut settings for $e\tau$ | 59 |
| 4.2 | Optimal $E - p_z$ and P_T^{Miss} cut settings as a function of the Higgs mass. . . | 59 |
| 4.3 | Relative loss in signal events due to the cut on θ_e | 62 |
| 4.4 | Cutflow for $\tau\tau$ in the 99/00 dataset. | 77 |
| 4.5 | Cutflow for $\tau\tau$ in the 96/97 dataset | 77 |
| 4.6 | Cutflow for $e\tau$ in the 99/00 dataset | 78 |
| 4.7 | Cutflow for $e\tau$ in the 96/97 dataset | 78 |
| 4.8 | Cutflow for a $\tau\tau$ signal of mass 100 GeV under 99/00 conditions | 79 |
| 4.9 | Cutflow for an $e\tau$ signal of mass 100 GeV under 99/00 conditions | 79 |
| 5.1 | Relative systematic errors estimated for the signal efficiency. | 83 |
| 5.2 | Relative systematic errors estimated for the background. | 85 |

Seite Leer /
Blank leaf

Bibliography

- [1] R. Barate et al., Search for the standard model Higgs boson at LEP, *Phys. Lett.* **B565**, 61 (2003).
- [2] A. Aktas et al., Multi-electron production at high transverse momenta in e p collisions at HERA, *Eur. Phys. J.* **C31**, 17 (2003).
- [3] H1 Collaboration, Search for Doubly Charged Higgs Production at HERA, ICHEP 2004 Contribution Paper Nr. 12-0767, 2004.
- [4] F. Halzen and A. D. Martin, *Quarks and Leptons: An Introductory Course in Modern Particle Physics*, John Wiley and sons, 1984.
- [5] F. Mandl and G. Shaw, *Quantum Field Theory*, John Wiley and sons, 1984.
- [6] S. L. Glashow, Partial Symmetries of Weak Interactions, *Nucl. Phys.* **22**, 579 (1961).
- [7] S. Weinberg, A Model of Leptons, *Phys. Rev. Lett.* **19**, 1264 (1967).
- [8] A. Salam, *Proceedings of the Eighth Nobel Symposium on Elementary particle theory*, Almquist and Wiksless, 1968.
- [9] S. Eidelman et al., Review of particle physics, *Phys. Lett.* **B592**, 1 (2004).
- [10] M. Kobayashi and T. Maskawa, CP violation in the renormalizable theory of weak interaction, *Prog. Theor. Phys.* **49**, 652 (1973).
- [11] C. Giunti and M. Laveder, Neutrino mixing, (2003).
- [12] J. F. Gunion, H. E. Haber, G. L. Kane, and S. Dawson, *The Higgs Hunter's Guide*, Perseus Publishing, 1990.
- [13] S. L. Glashow and S. Weinberg, Natural Conservation Laws For Neutral Currents, *Phys. Rev.* **D15**, 1958 (1977).
- [14] G. B. Gelmini and M. Roncadelli, Left-handed neutrino mass scale and spontaneously broken Lepton number, *Phys. Lett.* **B99**, 411 (1981).
- [15] R. Godbole, B. Mukhopadhyaya, and M. Nowakowski, Triplet Higgs bosons at e+ e- colliders, *Phys. Lett.* **B352**, 388 (1995).

- [16] J. F. Gunion, R. Vega, and J. Wudka, Higgs triplets in the standard model, *Phys. Rev.* **D42**, 1673 (1990).
- [17] R. E. Marshak and R. N. Mohapatra, Quark - Lepton symmetry and B-L as the U(1) generator of the electroweak symmetry group, *Phys. Lett.* **B91**, 222 (1980).
- [18] J. F. Gunion, J. Grifols, A. Mendez, B. Kayser, and F. I. Olness, Higgs Bosons in left-right symmetric models, *Phys. Rev.* **D40**, 1546 (1989).
- [19] T. Yanagida, Proceedings of the Workshop on Unified Theory and the Baryon Number of the Universe, KEK, Japan, 1979.
- [20] F. Gell-Mann, P. Ramond, and R. Slansky, *Supergravity*, North-Holland, 1979.
- [21] R. N. Mohapatra and G. Senjanovic, Neutrino mass and spontaneous parity nonconservation, *Phys. Rev. Lett.* **44**, 912 (1980).
- [22] J. F. Gunion, C. Loomis, and K. T. Pitts, Searching for doubly-charged Higgs bosons at future colliders, *ECONF C960625*, LTH096 (1996).
- [23] K. Huitu, J. Maalampi, A. Pietila, and M. Raidal, Doubly charged Higgs at LHC, *Nucl. Phys.* **B487**, 27 (1997).
- [24] G. Abbiendi et al., Search for doubly charged Higgs bosons with the OPAL detector at LEP, *Phys. Lett.* **B526**, 221 (2002).
- [25] P. Achard et al., Search for doubly-charged Higgs bosons at LEP, *Phys. Lett.* **B576**, 18 (2003).
- [26] J. Abdallah et al., Search for doubly charged Higgs bosons at LEP2, *Phys. Lett.* **B552**, 127 (2003).
- [27] G. Abbiendi et al., Search for the single production of doubly-charged Higgs bosons and constraints on their couplings from Bhabha scattering, *Phys. Lett.* **B577**, 93 (2003).
- [28] V. M. Abazov et al., Search for doubly-charged Higgs boson pair production in the decay to $\mu^+ \mu^+ \mu^- \mu^-$ in p anti-p collisions at $s^{*(1/2)} = 1.96$ -TeV, *Phys. Rev. Lett.* **93**, 141801 (2004).
- [29] D. Acosta et al., Search for doubly-charged Higgs bosons decaying to dileptons in p anti-p collisions at $s^{*(1/2)} = 1.96$ -TeV, *Phys. Rev. Lett.* **93**, 221802 (2004).
- [30] E. Perez, H1 internal note, in preparation.
- [31] A. Mucke, R. Engel, J. P. Rachen, R. J. Protheroe, and T. Stanev, SOPHIA: Monte Carlo simulations of photohadronic processes in astrophysics, *Comput. Phys. Commun.* **124**, 290 (2000).

- [32] H. L. Lai et al., Improved parton distributions from global analysis of recent deep inelastic scattering and inclusive jet data, *Phys. Rev.* **D55**, 1280 (1997).
- [33] T. Sjostrand, PYTHIA 5.7 and JETSET 7.4: Physics and manual, (1995).
- [34] I. Abt et al., The H1 detector at HERA, *Nucl. Instrum. Meth.* **A386**, 310 (1997).
- [35] W. Erdmann, *Untersuchung der Photoproduktion von D^* Mesonen am ep-Speicherring HERA*, PhD thesis, ETH Zürich, 1996.
- [36] B. Andrieu et al., The H1 liquid argon calorimeter system, *Nucl. Instrum. Meth.* **A336**, 460 (1993).
- [37] E. Iarocci, Plastic Streamer Tubes and their applications in High- Energy Physics, *Nucl. Instrum. Meth.* **217**, 30 (1983).
- [38] H. Itterbeck, *Techniques and Physics of the Central-Muon-Trigger System of the H1 Detector at HERA*, PhD thesis, University of Aachen, 1997.
- [39] E. Elsen, The H1 Trigger and Data Acquisition System, H1 internal note H1-01/93-262, 1993.
- [40] J. Rauschenberger, *Prozesse des geladenen Stromes in tiefunelastischer Positron-Proton Streuung bei HERA*, PhD thesis, Universität Hamburg, 2002.
- [41] GEANT - Detector Description and Simulation Tool, CERN Program Library Long Writeup W5013, 1997.
- [42] S. Lüders, *A Measurement of the Beauty Production Cross Section via $B \rightarrow J/\psi X$ at HERA*, PhD thesis, ETH Zürich, Oct. 2001.
- [43] L. West, How to use the Heavy Flavour working group track, muon and electron selection code, H1 internal note, 1997.
- [44] A. Levy, Low-x physics at HERA, DESY preprint 97-013 (1996).
- [45] E. Chabert et al., QBGFMAR: An updated PHAN package for cosmic and halo muon topological rejection in high p_T physics analysis, H1 internal note H1-11/98-556, 1998.
- [46] P. Bruel, *Recherche d'interactions au-delà du modèle standard à HERA*, PhD thesis, Université Paris Orsay, May 1998.
- [47] The H100 Physics Analysis Project, H1 internal note, 2004.
- [48] R. Sell, *Untersuchung der J/ψ -Produktion über den Zerfall $J/\psi \rightarrow \mu^+\mu^-$ am e-p-Speicher-ring HERA*, PhD thesis, 1996.
- [49] G. Schmidt, *Untersuchung der diffraktiven Photoproduktion von J/ψ Mesonen im H1-Detektor bei HERA*, PhD thesis, 1996.

- [50] U.-P. Krüger, *Untersuchung der Erzeugung schwerer Quarks durch ihren Zerfall in Muonen im H1-Detektor bei HERA*, PhD thesis, Universität Hamburg, 1994.
- [51] C. Veelken, *Search for Events with Isolated leptons and Large Missing Transverse Momentum in ep collisions at HERA*, PhD thesis, University of Liverpool, 2005.
- [52] B. Heinemann, *Measurement of Charged Current and Neutral Current Cross Sections in Positron-Proton Collisions at $\sqrt{s} \approx 300$ GeV*, PhD thesis, Universität Hamburg, 1999.
- [53] A. Schöning, *Untersuchung von Prozessen mit virtuellen und reellen W^\pm -Bosonen am H1-Detektor bei HERA*, PhD thesis, Universität Hamburg, 1996.
- [54] B. Leissner, *Muon Pair Production in Electron-Proton Collisions*, PhD thesis, RWTH Aachen, 2002.
- [55] S. Egli et al., Calculating Event Weights in Case of Downscaling on Trigger Levels 1-4, H1 internal note H1-04/97-517, 1997.
- [56] T. Sjostrand, L. Lonnblad, and S. Mrenna, PYTHIA 6.2: Physics and manual, (2001).
- [57] C. Adloff et al., Measurement of dijet cross sections in photoproduction at HERA, *Eur. Phys. J. C* **25**, 13 (2002).
- [58] H. Jung, Hard diffractive scattering in high-energy e p collisions and the Monte Carlo generation RAPGAP, *Comp. Phys. Commun.* **86**, 147 (1995).
- [59] G. A. Schuler and H. Spiesberger, DJANGO: The Interface for the event generators HERACLES and LEPTO, In *Hamburg 1991, Proceedings, Physics at HERA, vol. 3* 1419-1432. (see HIGH ENERGY PHYSICS INDEX 30 (1992) No. 12988).
- [60] L. Lonnblad, The colour-dipole model and the ARIADNE program at high Q^2 , (1999).
- [61] T. Abe, GRAPE-Dilepton (Version 1.1): A generator for dilepton production in e p collisions, *Comput. Phys. Commun.* **136**, 126 (2001).
- [62] G. Punzi, Sensitivity of searches for new signals and its optimization, *ECONF C030908, MODT002* (2003).
- [63] B. Olivier and E. Perez, Private Communications, 2005.
- [64] M. Kasprzak, *Inclusive properties of diffractive and non-diffractive photoproduction at HERA*, PhD thesis, 1996.
- [65] B. List and A. Mastroberardino, DIFFVM: A Monte Carlo generator for diffractive processes in e p scattering, Prepared for Workshop on Monte Carlo Generators for HERA Physics (Plenary Starting Meeting), Hamburg, Germany, 27-30 Apr 1998.

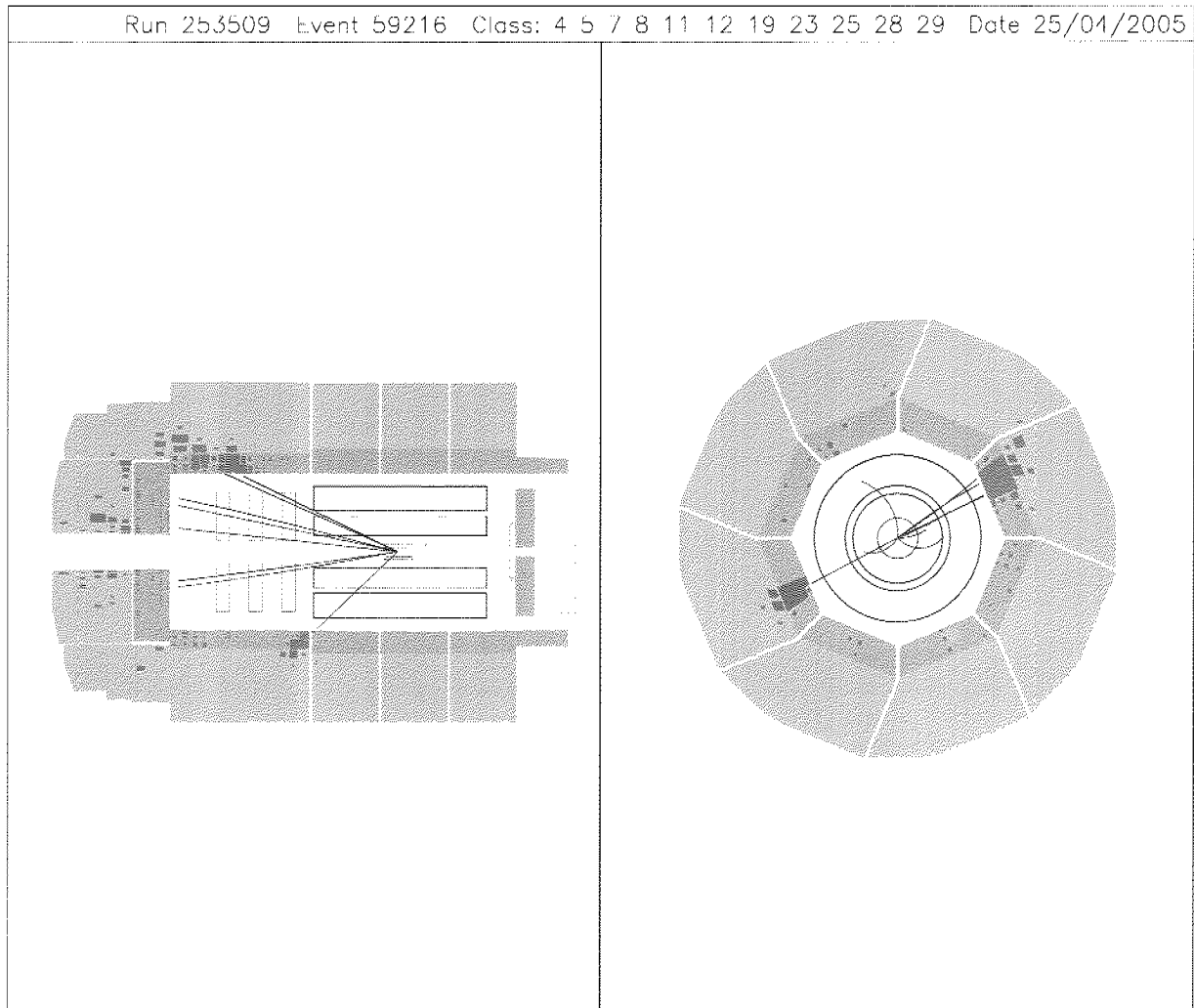
- [66] A. Aktas et al., Muon pair production in e p collisions at HERA, *Phys. Lett.* **B583**, 28 (2004).
- [67] G. Ingelman, A. Edin, and J. Rathsman, LEPTO 6.5 - A Monte Carlo Generator for Deep Inelastic Lepton-Nucleon Scattering, *Comput. Phys. Commun.* **101**, 108 (1997).
- [68] A. Schwank, *Effizienzbestimmung von Detektorkomponenten des H1-Experiments mit Hilfe kosmischer Strahlung*, Diploma Thesis, 1998.
- [69] T. Junk, Confidence level computation for combining searches with small statistics, *Nucl. Instrum. Meth.* **A434**, 435 (1999).
- [70] T. Junk, Confidence Level Computation for Combining Searches using the Likelihood Ratio, OPAL Technical Note TN-570, 1999.

Seite Leer /
Blank leaf

Appendix A

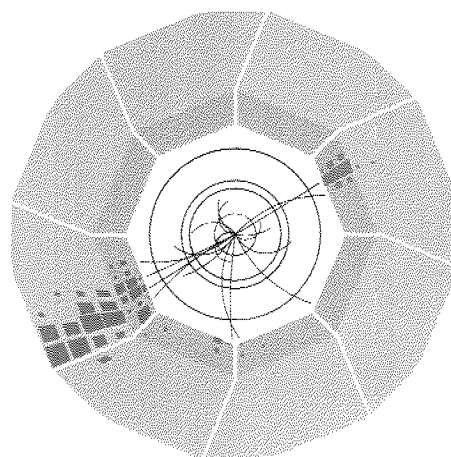
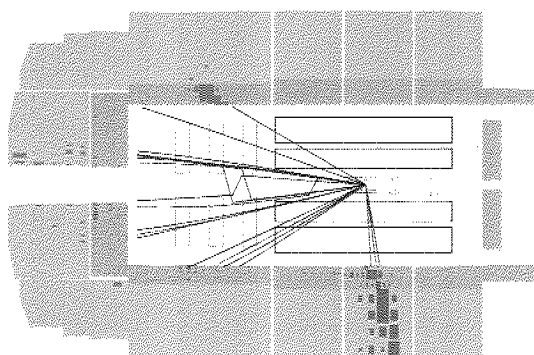
Data Events

The data events presented here survive all analysis cuts. They are all found in the **inelastic ej event class**, which is the only class with a background expectation significantly different from zero. However, the background expectation is in good agreement with the number of data events found (s. Tables 4.4, 4.5, 4.6 and 4.7). The electron can be identified in these events in the sideview event displays from the electron polar angle θ_e given in each Table. Surprisingly for many of the events the jet isolation cut seems to have failed. The reason is that in the event displays all tracks are drawn, while only good quality tracks are considered for the isolation requirements.

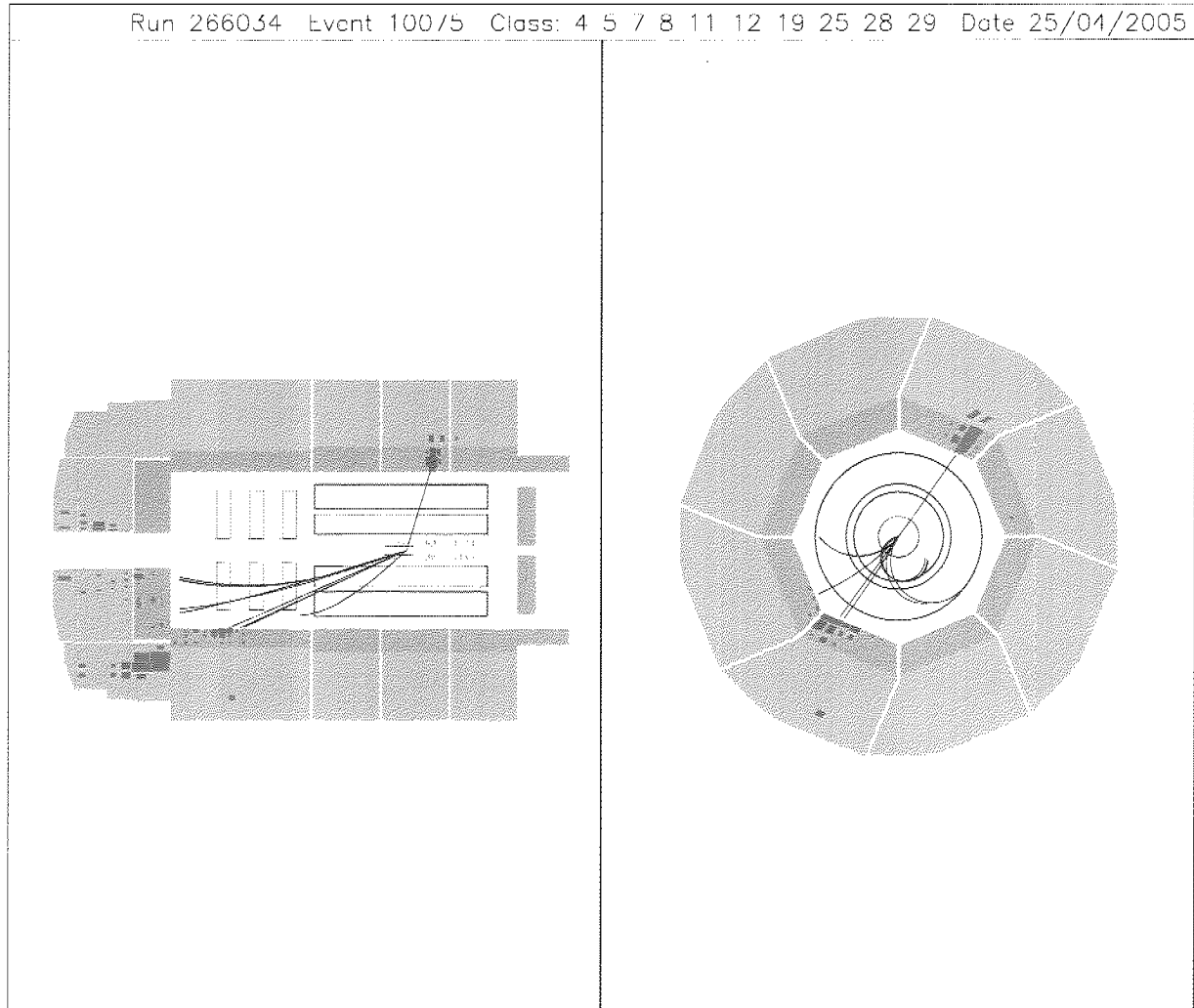


| | |
|--------------------|------------|
| Dataset | 99/00 |
| Topology | $\tau\tau$ |
| Run Number | 253509 |
| Event Number | 59216 |
| Reconstructed Mass | 170 GeV |
| $E - p_z$ | 34 GeV |
| P_T^{Miss} | 7.2 GeV |
| η_{max} | 3.2 |
| θ_e | 44° |

Run 263530 Event 61821 Class: 4 5 / 8 11 12 19 25 28 29 Date 25/04/2005

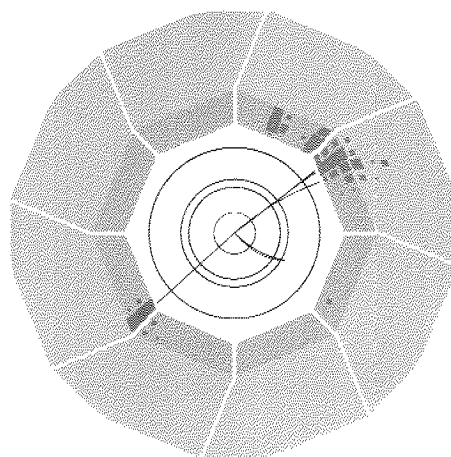
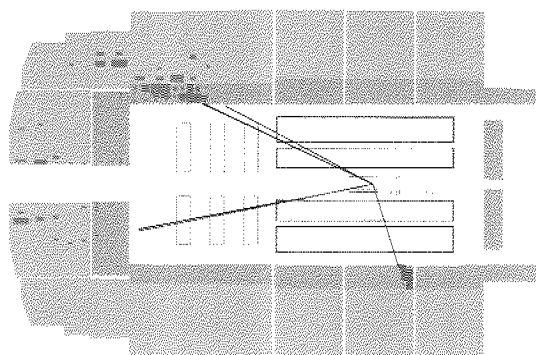


| | |
|--------------------|------------|
| Dataset | 99/00 |
| Topology | $\tau\tau$ |
| Run Number | 263530 |
| Event Number | 61821 |
| Reconstructed Mass | 97 GeV |
| $E - p_z$ | 44 GeV |
| P_T^{Miss} | 9.4 GeV |
| η_{max} | 3.3 |
| θ_e | 30° |

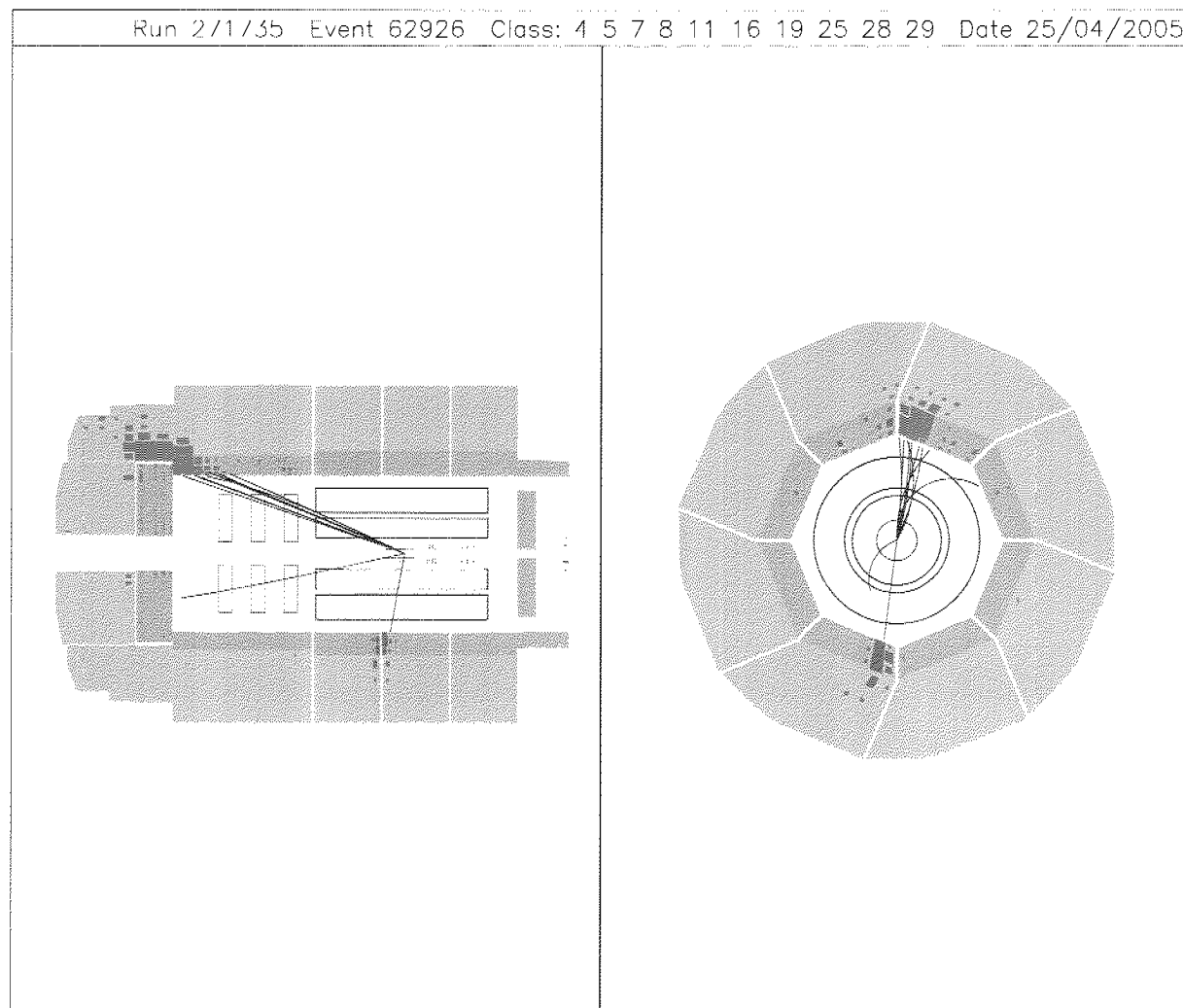


| | |
|--------------------|-------------|
| Dataset | 99/00 |
| Topology | $\tau\tau$ |
| Run Number | 266034 |
| Event Number | 10075 |
| Reconstructed Mass | 97 GeV |
| $E - p_z$ | 40 GeV |
| P_T^{Miss} | 3.6 GeV |
| η_{max} | 3.4 |
| θ_e | 107° |

Run 268105 Event 90584 Class: 4 5 7 8 11 19 25 28 29 Date 25/04/2005

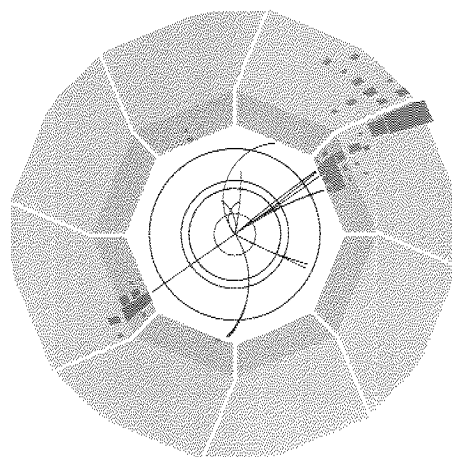
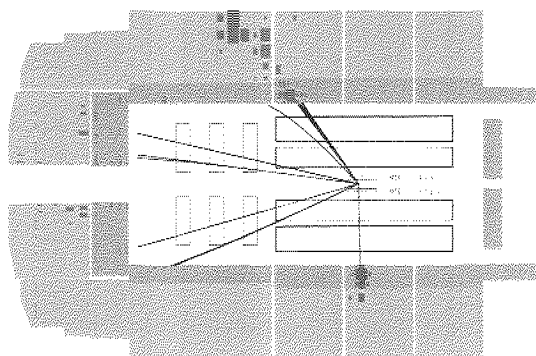


| | |
|--------------------|-------------|
| Dataset | 99/00 |
| Topology | $\tau\tau$ |
| Run Number | 268105 |
| Event Number | 90584 |
| Reconstructed Mass | 91 GeV |
| $E - p_z$ | 39 GeV |
| P_T^{Miss} | 0.8 GeV |
| η_{max} | 3.5 |
| θ_c | 108° |

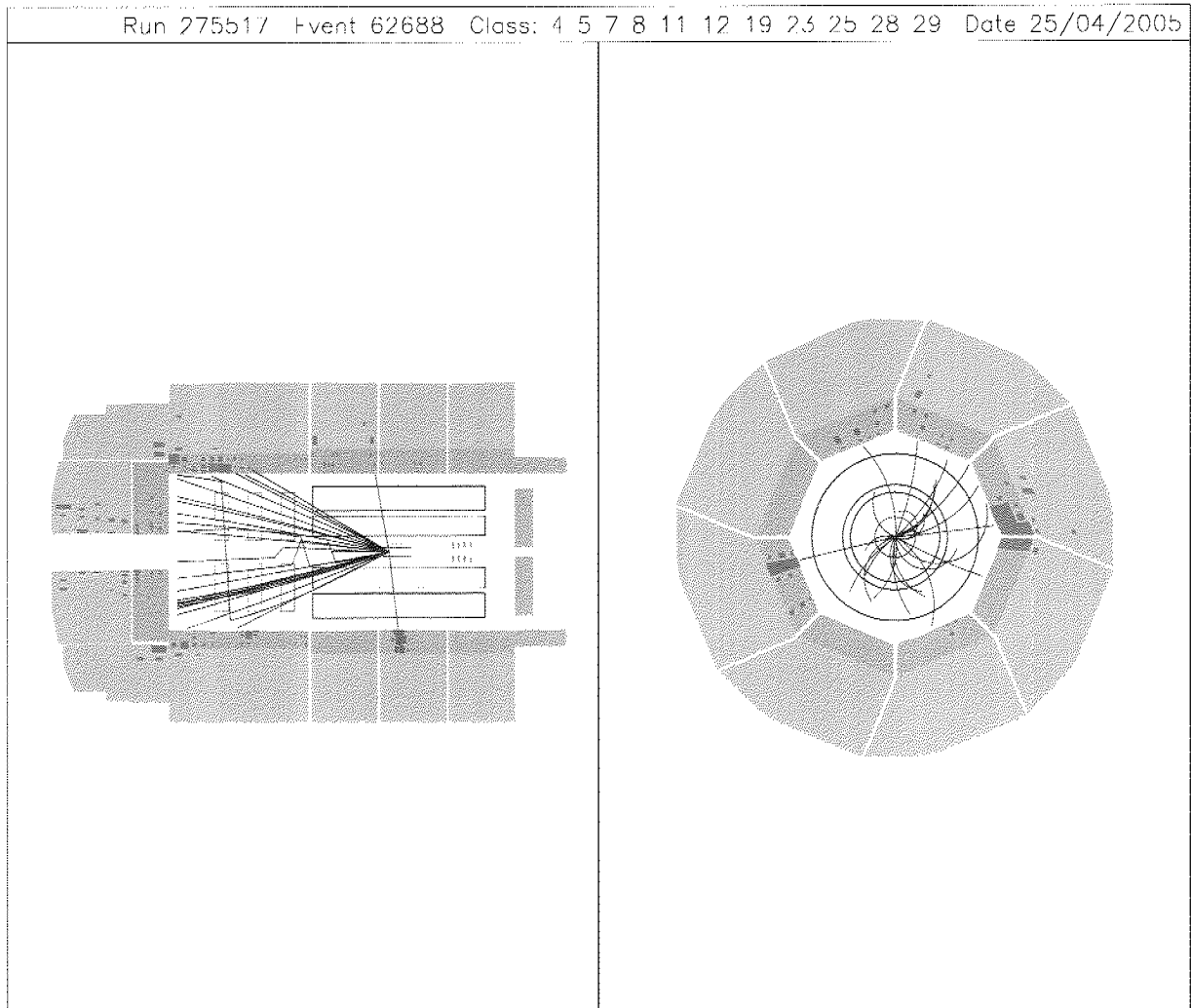


| | |
|--------------------|------------|
| Dataset | 99/00 |
| Topology | $\tau\tau$ |
| Run Number | 271735 |
| Event Number | 62926 |
| Reconstructed Mass | 136 GeV |
| $E - p_z$ | 42 GeV |
| P_T^{Miss} | 6.4 GeV |
| η_{max} | 3.2 |
| θ_e | 80° |

Run 272940 Event 3873 Class: 4 5 7 8 11 19 23 25 28 29 Date 25/04/2005

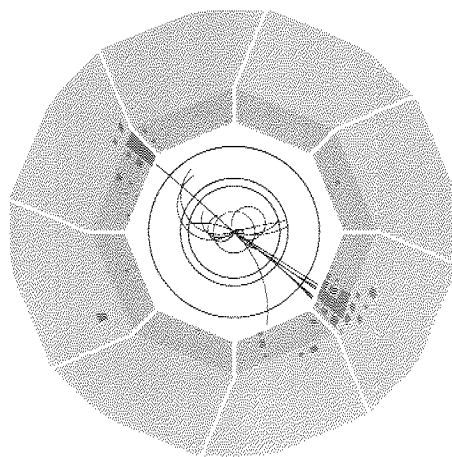
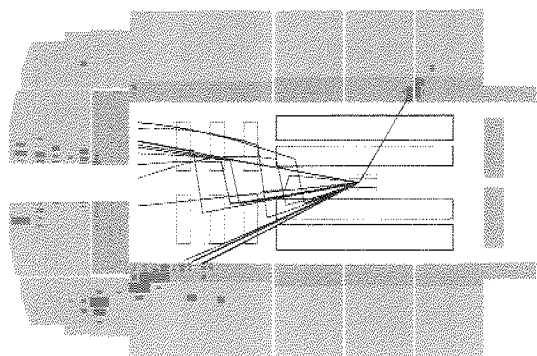


| | |
|--------------------|------------|
| Dataset | 99/00 |
| Topology | $\tau\tau$ |
| Run Number | 272940 |
| Event Number | 3873 |
| Reconstructed Mass | 75 GeV |
| $E - p_z$ | 44 GeV |
| P_T^{Miss} | 6.2 GeV |
| η_{max} | 3.3 |
| θ_c | 91° |

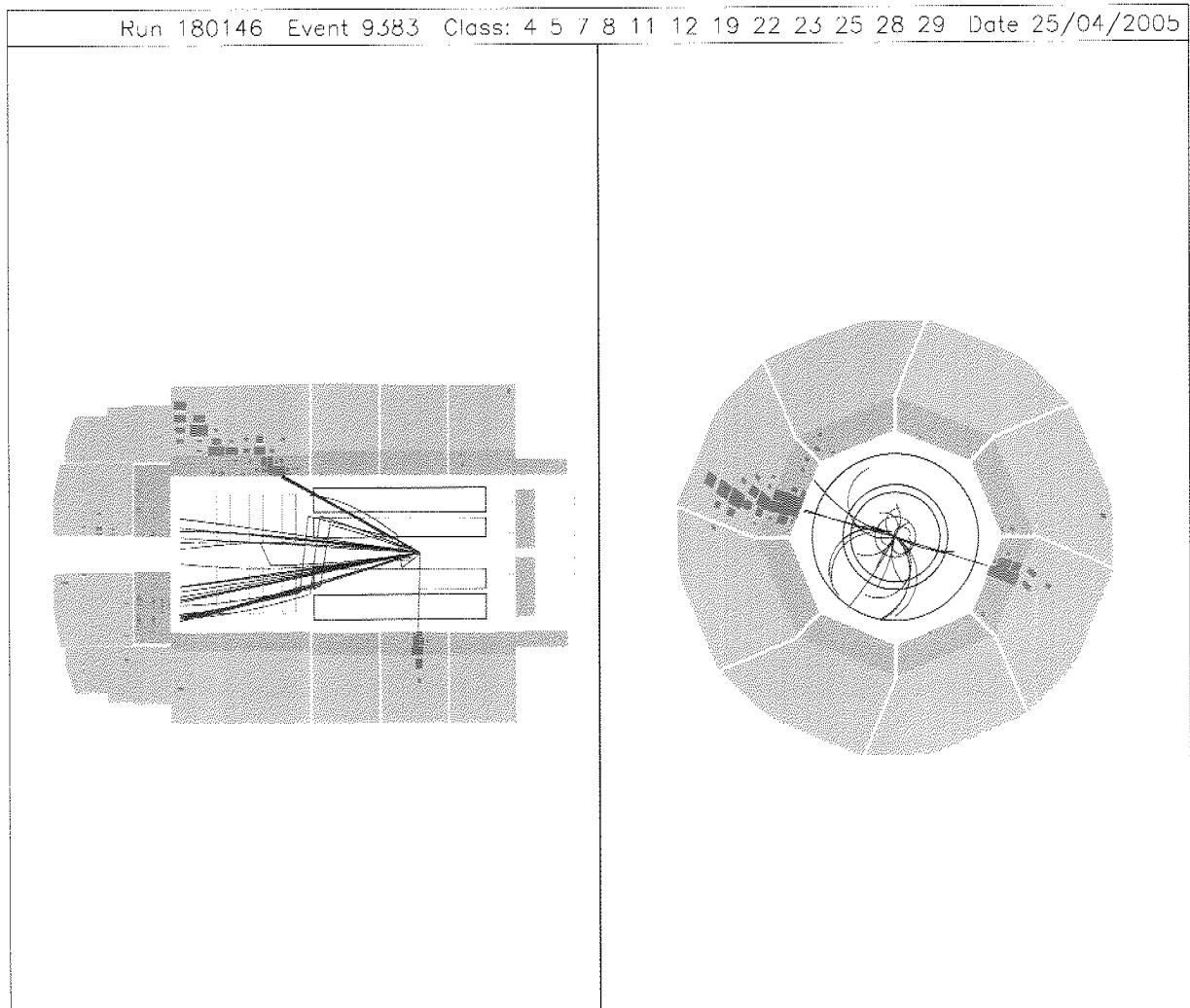


| | |
|--------------------|------------|
| Dataset | 99/00 |
| Topology | $\tau\tau$ |
| Run Number | 275517 |
| Event Number | 62688 |
| Reconstructed Mass | 87 GeV |
| $E - p_z$ | 40 GeV |
| P_T^{Miss} | 3.0 GeV |
| η_{max} | 3.5 |
| θ_c | 96° |

Run 164642 Event 137205 Class: 4 7 8 9 11 19 25 28 29 Date 25/04/2005

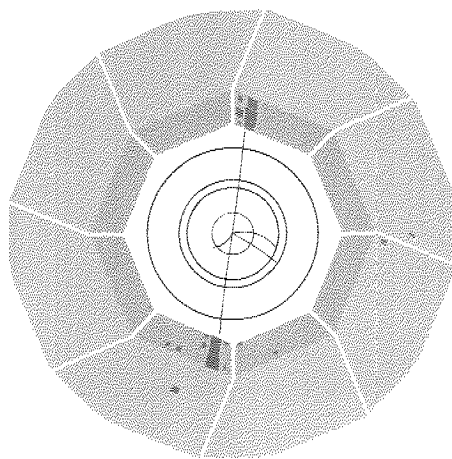
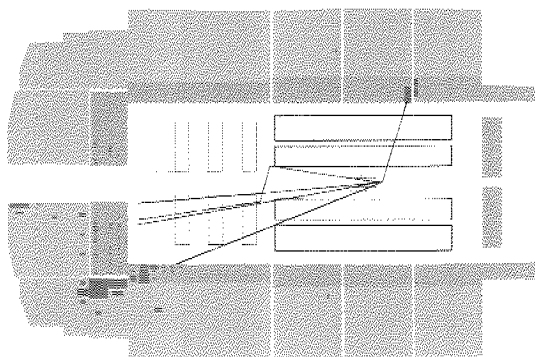


| | |
|--------------------|------------|
| Dataset | 96/97 |
| Topology | $\tau\tau$ |
| Run Number | 164642 |
| Event Number | 137205 |
| Reconstructed Mass | 85 GeV |
| $E - p_z$ | 41 GeV |
| P_T^{Miss} | 6.1 GeV |
| η_{max} | 3.3 |
| θ_e | 120° |

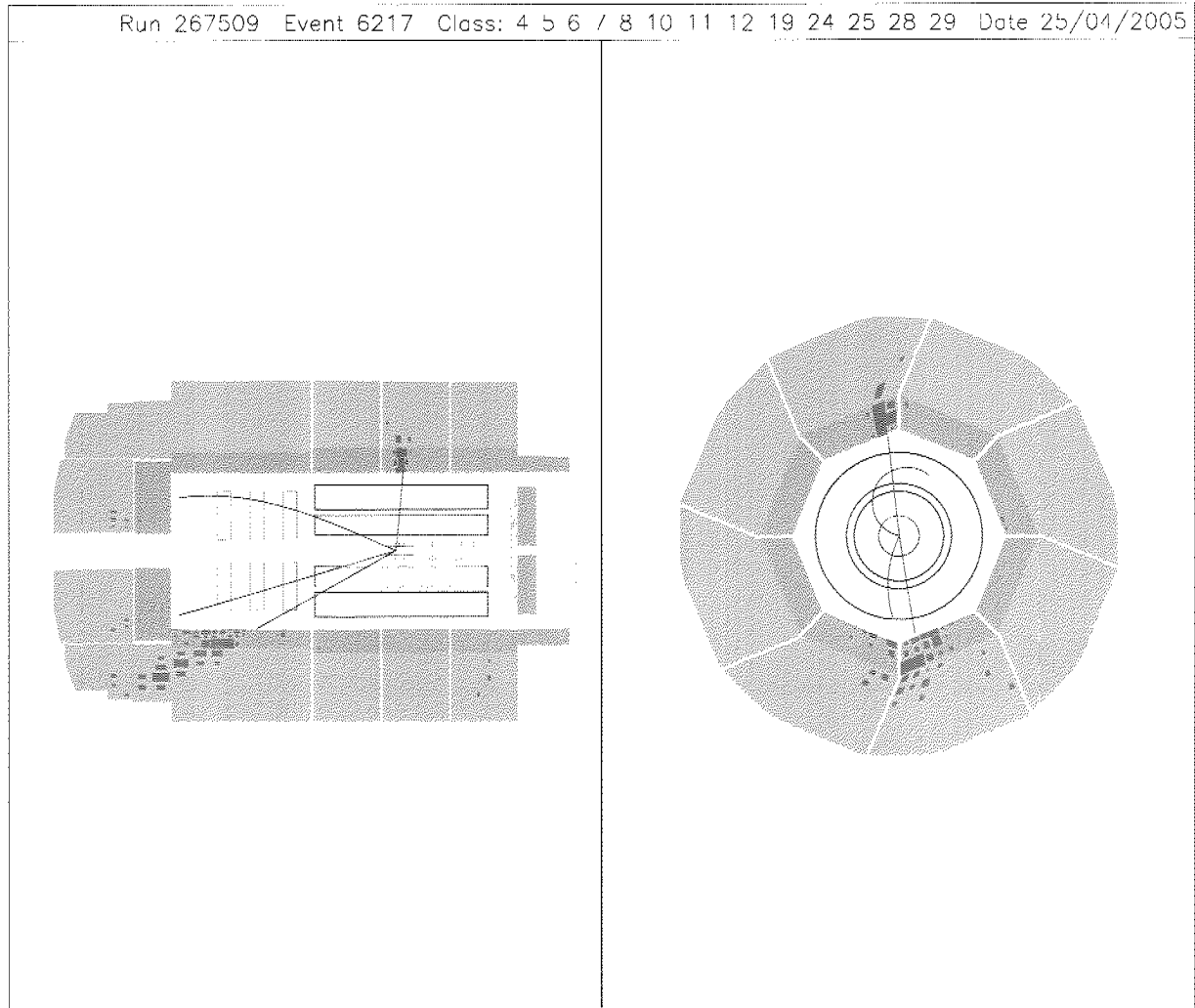


| | |
|--------------------|------------|
| Dataset | 96/97 |
| Topology | $\tau\tau$ |
| Run Number | 180146 |
| Event Number | 9383 |
| Reconstructed Mass | 103 GeV |
| $E - p_z$ | 44 GeV |
| P_T^{Miss} | 8.1 GeV |
| η_{max} | 3.3 |
| θ_e | 88° |

Run 199905 Event 33204 Class: 4 7 8 9 11 16 19 22 23 28 29 Date 25/04/2005



| | |
|--------------------|------------|
| Dataset | 96/97 |
| Topology | $\tau\tau$ |
| Run Number | 199905 |
| Event Number | 33204 |
| Reconstructed Mass | 106 GeV |
| $E - p_z$ | 18 GeV |
| P_T^{Miss} | 2.0 GeV |
| η_{max} | 3.5 |
| θ_e | 107° |



| | |
|--------------------|------------|
| Dataset | 99/00 |
| Topology | $e\tau$ |
| Run Number | 267509 |
| Event Number | 6217 |
| Reconstructed Mass | 92 GeV |
| $E - p_z$ | 46 GeV |
| P_T^{Miss} | 16 GeV |
| η_{max} | 2.8 |
| θ_e | 95° |

Danksagung

An dieser Stelle möchte ich den zahlreichen Personen danken, ohne deren vielfältige Hilfe die vorliegende Arbeit nicht möglich gewesen wäre. Zunächst geht mein Dank an meinen Doktorvater, Prof. Ralph Eichler, der mir diese Arbeit überhaupt erst ermöglicht hat. Seiner pragmatischen Einstellung verdanke ich die Einsicht, dass ein wesentlicher Teil einer solchen Arbeit darin besteht, innert nützlicher Frist zu einem Abschluss zu kommen, selbst wenn dabei einzelne Teilaspekte nicht bis zu Ende optimiert werden können.

Ganz speziell danke ich auch meinem Betreuer, André Schöning, ohne den diese Arbeit nicht gelungen wäre. Seine Fähigkeit bei (fast) allen möglichen und unmöglichen Problemen den richtigen Lösungsansatz zu finden und seine unzähligen Verbesserungsvorschläge waren für mich extrem wertvoll.

Des Weiteren möchte ich den anderen Postdocs unserer Gruppe danken: Benno List hat mir mit seinem ungeheuren Fachwissen immer wieder Fragen zur Physik, Analyse und Programmieretechnik beantwortet. Mein Bürokollege, Christoph Grab, hat mir oft gute und kritische Fragen zu meiner Analyse gestellt und mir einige technische Details zur Datenanalyse und Statistik erklärt. Guillaume Leibenguth hat mich dazu bewogen, rechtzeitig mit dem Zusammenschreiben anzufangen und hat meine ersten Kapitel korrekturgelesen.

In den "Rare and EXotics (REX)" meetings in Hamburg, habe ich immer wieder gute Anhaltspunkte zur weiteren Verbesserung, resp. Problembhebung bekommen. Speziell bedanken möchte ich mich hier bei: Emmanuelle Perez fuer den MC Generator, Jenny List für die intensive Hilfe bei der Verwendung von Tom Junk's Limit-Berechnungsprogramm, Bob Olivier, Emmanuel Sauvan und Cristi Diaconu für die vielen Informationen über die anderen Higgs Analysen und Christian Veelken für viele Tipps und Auskünfte über das h100 Softwarepaket.

Für weitere gute Korrekturvorschläge und die Begutachtung dieser Arbeit danke ich Prof. Urs Langenegger.

Meinen Zürcher Doktorandenkollegen Salvatore Mangano, David Meer, Markus Bischofberger und Marc Del Degan danke ich für das ausserordentlich gute Arbeitsklima. Auch ausserhalb der Arbeit verbrachten wir eine gute Zeit. Meinen Hamburger Doktorandenkollegen Ronnie Weber, Nik Berger und Tobias Zimmermann verdanke ich, dass meine Aufenthalte in Hamburg für mich nicht zu reinen "Arbeitsaufenthalten" verkamen.

Schliesslich danke ich ganz besonders meinen Eltern, meinem Bruder und meinen Freunden, die mich in dieser Zeit immer unterstützt haben, insbesondere dann, wenn die Probleme bei der Arbeit mal wieder unüberwindbar zu sein schienen.

Seite Leer /
Blank leaf

Curriculum Vitae

Persönliche Daten

| | |
|--------------|--------------------------|
| Name | Simon Daniel Baumgartner |
| Geburtsdatum | 30. Oktober 1975 |
| Geburtsort | Bern (Schweiz) |
| Nationalität | CH |

Schulische / Berufliche Laufbahn

| | |
|-------------|---|
| 1982 – 1986 | Primarschule Münsingen / BE |
| 1986 – 1990 | Sekundarschule Münsingen / BE |
| 1990 – 1995 | Gymnasium Bern-Neufeld Typus C, Matura 1995 |
| 1995 – 1997 | Grundstudium Physik an der EPFL in Lausanne |
| 1997 – 2000 | Fachstudium Physik an der ETH Zürich |
| 2000 | Diplom in Physik an der ETHZ im Herbst 2000 Diplomarbeit in der PSRD (Prototype Synchrotron Radiation Detector) Gruppe von Professor G. Viertel |
| 2000 – 2001 | Auf 6 Monate befristete Anstellung in der PSRD Gruppe bis zur Fertigstellung und Abgabe des Detektors am Goddard Space Flight Center der NASA |
| 2001 – 2005 | Doktorarbeit an der ETH Zürich und am DESY in Hamburg |